Optical Properties of annealed hydrogenated amorphous silicon nitride (a-SiNx:H) thin films for photovoltaic application

Sulaiman Jacobs

A thesis submitted in fulfilment of the requirements for the degree of Magister Scientiae in the Department of Physics, University of the Western Cape.

Supervisor: Dr T. F. G. Muller (University of the Western Cape)

Co-supervisors: Prof C. J. Arendse & Dr G. F. Malgas

(University of the Western Cape)

November 2013

To My Late granny, Hajji Mymona Jacobs, She would have been so proud of me.

UNIVERSITY of the
WESTERN CAPE

Acknowledgments

In the name of Allâh, most Gracious, most Compassionate, all the praises and thanks be to Allâh, the Lord of the Worlds, without Him none of this would have been possible.

To Dr. Theo Muller, it has been a pleasure being your very first student, and I thank you for your guidance and the many discussions we had, for the friendship and support you gave me and helping me along on this bumpy journey, guiding me, teaching me and allowing me the freedom to explore my own research avenues.

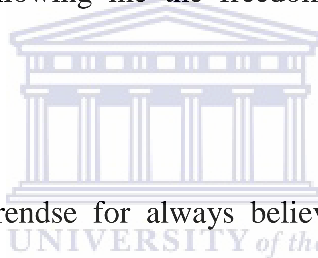

To Prof. Christopher Arendse for always believing in me, for giving me the opportunities to continually improve myself and for the encouragement to always do my best.

I would like to use this opportunity to thank two people who have indirectly and directly guided me into this stream of science, To Dr. Zainunisha Arieff who firstly guided me into the Science Faculty at U.W.C., and always took an interest in me and my progress. To Mr. Ian Schroeder, for the many hours of computational physics, and for always taking a keen interest in my progress, up till now, influencing and guiding me on my new career path. For looking out for me and always wanting the best for me.

I would like to thank the folks at iThemba labs for assisting me with the experiments, especially Dr. Lebogang Chester Kotsedi who took the time to demonstrate the operating procedures of the annealing oven, and for the friendly conversations and the interest he took in my project. To Dr. Nkosi for performing the AFM measurements, and to Mr. Phillip Sechogela for staying late nights at iThemba labs to perform my ERD analysis.

To Dr. Gerald Malgas who was at the CSIR while I was performing experiments, thank you for teaching me and looking out for me while I was there. Thank you to everyone in the Chemistry Department at UWC, for your assistance in measuring FTIR, and for lab supplies when our labs did not have.

To Ms Angela Adams for always looking out for me while I was a postgraduate student in the Physics Department, and teasing me about my lunch

To my family who sacrificed, supported and encouraged me to always follow my dreams and never give up. Thank you to my parents on whose backs I rode while I was a student. Thank you to my sister who supported me financially and always encouraged me, telling me "it will all be worth it in the end".

To my friends at university, Razia, Abdul and Nazley, thank you for your help and support, I'm going to miss you guys.

UNIVERSITY of the
WESTERN CAPE

Last but not least to my fiancé, Zubeidah Khan. Thank you for your love, support and understanding, for encouraging me to complete this MSc, and for never doubting my ability, even when I did. ***I love you much***.

To the National Research Foundation (NRF) for the generous funding over the duration of the study, and to the University of the Western Cape where I have received my education and training to pursue my research.

UNIVERSITY of the
WESTERN CAPE

Declaration

I declare that

‘‘Optical Properties of annealed hydrogenated amorphous silicon nitride (a-SiNx:H) thin films for photovoltaic application”

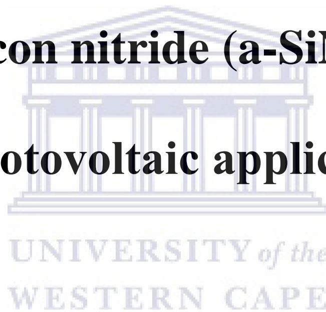

is my own work, that it has not been submitted for any degree or examination in any other university, and that all the sources I have used or quoted have been indicated and acknowledged by means of complete references.

Sulaiman Jacobs **November 2013**

Signature: _______________

Keywords

Optical Properties of annealed hydrogenated amorphous silicon nitride (a-SiNx:H) thin films for photovoltaic application

Sulaiman Jacobs

UNIVERSITY of the
WESTERN CAPE

Hot-wire chemical vapour deposition (HWCVD)

Hydrogenated amorphous silicon Nitride (a-SiN_x:H)

Hydrogen dilution

Annealing

Optical properties

Dielectric functions

Band gap

Refractive index

Surface roughness

Composition

Abstract

Optical Properties of annealed hydrogenated amorphous silicon nitride (a-SiNx:H) thin films for photovoltaic application

Sulaiman Jacobs

MSc. Thesis, Physics Department, University of the Western Cape.

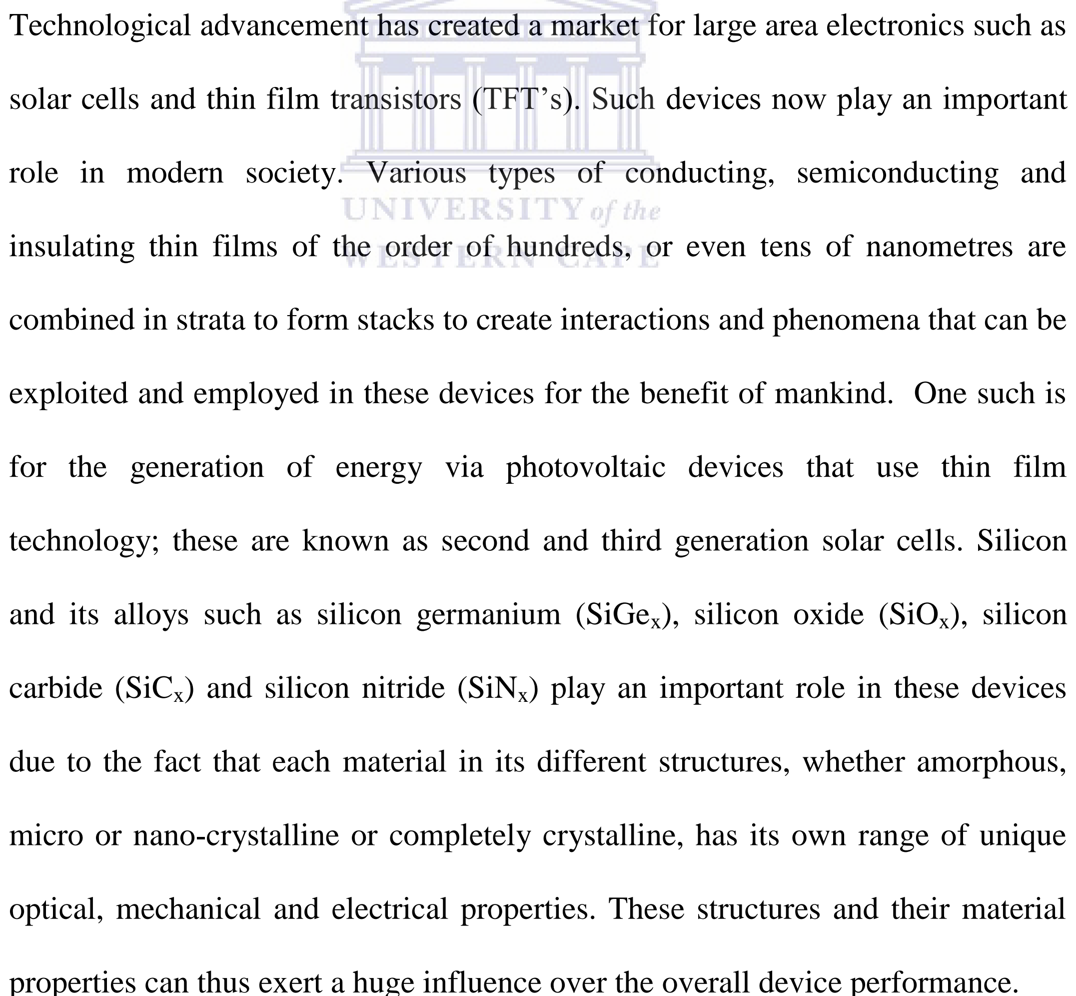
UNIVERSITY of the
WESTERN CAPE

Technological advancement has created a market for large area electronics such as solar cells and thin film transistors (TFT's). Such devices now play an important role in modern society. Various types of conducting, semiconducting and insulating thin films of the order of hundreds, or even tens of nanometres are combined in strata to form stacks to create interactions and phenomena that can be exploited and employed in these devices for the benefit of mankind. One such is for the generation of energy via photovoltaic devices that use thin film technology; these are known as second and third generation solar cells. Silicon and its alloys such as silicon germanium ($SiGe_x$), silicon oxide (SiO_x), silicon carbide (SiC_x) and silicon nitride (SiN_x) play an important role in these devices due to the fact that each material in its different structures, whether amorphous, micro or nano-crystalline or completely crystalline, has its own range of unique optical, mechanical and electrical properties. These structures and their material properties can thus exert a huge influence over the overall device performance.

Chemical vapour deposition (CVD) techniques are most widely used in industry to obtain thin films of silicon and silicon alloys. Source gases are decomposed by the external provision of energy thereby allowing for the growth of a thin solid film on a substrate. In this study a variant of CVD, namely Hot Wire Chemical Vapour Deposition (HWCVD) will be used to deposit thin films of silicon nitride by the decomposition of silane (SiH_4), hydrogen (H_2) and ammonia (NH_3) on a hot tantalum filament (~1600 °C). Hydrogenated amorphous silicon nitride (a-SiN_x:H) has great potential for application in optoelectronic devices. In commercial solar cell production its potential for use as anti-reflection coatings are due to its intermediate refractive index combined with low light absorption. An additional benefit is the passivation of interface and crystal defects due to the bonded hydrogen. This can lead to better photon conversion efficiency. Its optical properties including optical band gap, Urbach tail, and wavelength-dependent optical constants such as absorption coefficient and refractive index are crucial for the design and application in the relevant optoelectronic device. The final firing step in the production of micro-crystalline silicon solar cells, allows hydrogen to effuse into the solar cell from the a-SiN_x:H, and drives bulk passivation of the grain boundaries. We therefore propose the exploration of annealing effects on the thin film structure. The study undertakes a comparison of optical and bonding structure of the as deposited thin film compared to that of the annealed thin film which would have undergone changes due to high temperature annealing under vacuum. However, it is difficult to simultaneously obtain all of these important

UNIVERSITY of the
WESTERN CAPE

optical parameters for a-SiN_x:H thin films. Ultraviolet visible (UV-vis) spectroscopy will be the method of choice to investigate the optical properties.

Infrared (IR) spectroscopy is a source of useful information on the microstructure of the material. In particular, the local atomic bonding configurations involving Si, N, and H atoms in a-SiN_x:H films can be obtained by Fourier Transform Infrared Spectroscopy (FTIR). Therefore, this study will attempt to establish a relationship between film microstructure of a-SiNx:H thin films and their macroscopic optical properties.

UNIVERSITY of the
WESTERN CAPE

List of Abbreviations

Materials

a-SiN_x	: Amorphous Silicon Nitride (non-stoichiometric)
a-Si_3N_4	: Amorphous Silicon Nitride (stoichiometric)

Deposition Methods

HWCVD	: Hot-wire chemical vapour deposition
LPCVD	: Low-pressure chemical vapour deposition
PECVD	: Plasma-enhanced chemical vapour deposition
GD	: Glow Discharge Chemical Vapour Deposition
RF	: Radio Frequency Chemical Vapour Deposition
VHFCVD	: Very High Frequency Chemical Vapour Deposition

UNIVERSITY of the
WESTERN CAPE

Deposition Parameters

T_{wire}	: Filament temperature
T_{sub}	: Substrate temperature
P	: Chamber pressure
P_{gas}	: Gas Pressure

Analysis Techniques

ERDA	: Elastic Recoil Detection Analysis
FTIR	: Fourier Transform Infrared spectroscopy
RAMAN	: Raman Scattering
HRSEM	: High Resolution Scanning Electron Microscopy
XRD	: X-Ray Diffraction
AFM	: Atomic Force Microscopy

List of Symbols

Optical Measurements

ν or ω	: Photon frequency
h ν or $\hbar\omega$	: Photon energy
c	: Speed of light in a vacuum
ε_0	: Vacuum permittivity
Ω	: Size of the volume element containing one electron
$P(\omega)$	: Momentum matrix element for absorption
$\sigma(\omega)$	: Photo-conductivity
$\alpha(\nu)$	: Absorption coefficient
$n(\nu)$	: Real part of the complex refractive index
n_0	: Refractive index at zero energy
$k(\nu)$	: Imaginary part of the complex refractive index
$f(E)$	: Fermi-Dirac distribution
$N(E)$	: Density of states distribution in the valence band
$N(E+ \hbar\omega)$	: Density of states distribution in the conduction band
E_v	: Mobility edge of the valence band
E_c	: Mobility edge of the conduction band
E_g	: Optical band gap
$E_{g(Tauc)}$	: Tauc band gap

UNIVERSITY of the
WESTERN CAPE

Fourier Transform Infrared Spectroscopy

ω	: Wavenumber
$\alpha(\omega)$	: Absorption coefficient
$T(\omega)$	: Transmission
T_0	: Baseline transmission when $\alpha(\omega) = 0$
d	: Film thickness
α_{BCC}	: BCC corrected absorption coefficient
α_{TRUE}	: True absorption coefficient

UNIVERSITY of the
WESTERN CAPE

ELASTIC RECOIL DETECTION

K	: Kinematic factor
$\frac{d\sigma}{d\Omega}$	: Differential scattering cross section
$\frac{dE}{dx}$	: Rate of energy loss or stopping power
$\sigma(\omega)$	: Scattering cross section
Ω	: Finite solid angle spanned by the detector
Y	: Yield or number of detected particles
Q	: Total number of incident particles in the projectile beam
N_s	: Number of target atoms per cm^2
$[H]_{ERDA}$	: Hydrogen concentration determined by ERDA

X-Ray Diffraction

[uvw]	: Indices of the direction of a line
a, b, c	: Lengths of crystallographic axes of unit cell
α, β, γ	: Angles between crystallographic axes of unit cell
h, k, l	: Miller indices
d_{hkl}	: Spacing of the (hkl) plane
d	: Interplanar spacing
λ	: Wavelength of incident radiation
a	: Lattice parameter of unit cell
θ	: Bragg angle

Raman Spectroscopy

Γ	: FWHM of absorption peak
$\Delta\vartheta_b$	: Root-mean-square bond angle variation

Physical Constants

Constant	Symbol	Value
Boltzmann's Constant	k	1.381×10^{-23} JK^{-1}
Planck's Constant	h or $\hbar$=h/2π	6.626×10^{-34} Js or 1.055×10^{-34} Js
Speed of Light in a Vacuum	c	3×10^{8} m.s^{-1}
Permittivity of Free Space	ε_0	8.854×10^{-12} C^2/(Nm^2)

UNIVERSITY of the
WESTERN CAPE

Contents

Acknowledgments ii
Declaration v
Keywords vi
Abstract vii
List of Abbreviations x
List of Symbols xii
Physical Constants xv
Contents xvi
Chapter 1: Introduction 1
1.1 Fossil Fuels and Renewable energy 1
1.2 Photovoltaics and Semiconductors 2
1.2.1 p-n Junctions 5
1.2.2 The Diode Equation 6
1.2.3 Amorphous Silicon (a-Si) 8
1.2.4 Thin film solar cells 10
1.2.5 p-i-n Junctions 11
1.2.6 Anti-Reflective Coating (ARC's) 13
1.2.7 Silicon Nitride 15
1.3 Deposition of a-SiN_x 18
1.4 Post deposition annealing of a-SiN_x 19
1.5 Aims and Outlines 20
References 22
Chapter 2: Experimental Methods 24
2.1 Chemical Vapour Deposition 24
2.1.1 Hot Wire Chemical Vapour Deposition 31
2.1.2 Deposition of SiN_x 32
2.2 Thin Film Deposition 34
2.2.1 Sample Preparation 34
2.2.2 Deposition Parameters 34
2.2.3 Annealing 36
2.3 Analytical Techniques 39
2.3.1 X-Ray Diffraction (XRD) 39

UNIVERSITY of the
WESTERN CAPE

2.3.2 Raman Spectroscopy 47
2.3.3 Fourier Transform Infrared (FTIR) Spectroscopy 55
2.3.4 Elastic Recoil Detection Analysis (ERDA) 62
2.3.5 Atomic Force Microscopy (AFM) 66
2.3.6 High Resolution Scanning Electron Microscopy (HRSEM) 71
2.3.7 UV-Vis Spectroscopy 79
References 94
Chapter 3: Results and Discussion 98
3.1 Introduction 98
3.2 Characterisation of a-SiN_x:H 102
3.2.1 Structural Characteristics 102
3.2.2 Compositional Properties 107
3.2.3 Surface Characteristics 118
3.2.4 Optical Characteristics 129
Conclusion 150
References 154
Summary 158

UNIVERSITY of the
WESTERN CAPE

Chapter 1: Introduction

1.1 Fossil Fuels and Renewable energy

The majority of the world's energy needs are met through the use of non-renewable fossil fuels. The demand for energy is increasing with the growth in population, while the amount of fossil fuels available is on a sharp decline. Another problem faced with the use of fossil fuels is the copious amounts of pollution released, impacting on the environment and worsening the greenhouse effect. The necessity for clean and renewable energy is greater now than it ever was and should be delivered cheaply and efficiently to every corner of the earth. A number of renewable energy sources are available, for instance, wind power, nuclear energy, and geothermal power to name a few, that may off-set the dwindling stocks of fossil fuels. These, however, are costly to set up and may not be as reliable as the trusted fossil fuels, and are often unsafe if used incorrectly.

UNIVERSITY of the
WESTERN CAPE

The sun radiates energy onto the earth at approximately 1kW/m^2, and the larger part of it is unused. One device capable of converting the energy of the sun for sustainable use is a photovoltaic solar cell. The photovoltaic process or effect makes use of devices consisting of semiconducting material to generate electricity from the energy of the sun. The derivation of energy by the photovoltaic process is done cleanly and efficiently and can be delivered to the most rural of places, thereby improving the quality of life.

1.2 Photovoltaics and Semiconductors

Semiconductors are materials which are not completely insulating and, when excited by enough energy causes a current to flow. A single atom contains discrete energy levels, each level holding electrons according to Pauli's exclusion principle. The outer energy level of the atom contains unpaired electrons, which constitutes the valence shell of the atom. The electrons found in the valence shell are typically loosely bound and experiences less force due to the nucleus compared to electrons in the energy levels below it. This is due to the shielding effect by the preceding energy levels that allow the electrons to be excited so easily.

UNIVERSITY of the
WESTERN CAPE

In a pure and ordered bulk material, consisting of many such atoms, the discrete energy levels of each atom merge to form band structures. These band structures that form are not continuous, and are separated by a band gap denoted by E_g [1.1]. Below the band gap is the valence band. At low temperatures the valence band is completely filled with electrons. Above the band gap is the conduction band, which is empty at low temperatures. Band structures are described by the density of states functions (DOS), which is the number of allowed states per energy value and is finite. If the DOS is zero, then no states are available. In a perfectly crystalline material, where the long range order is preserved, no energy states are allowed in the band gap which means the DOS is zero. A simplified schematic of the DOS is shown in figure 1.1 below.

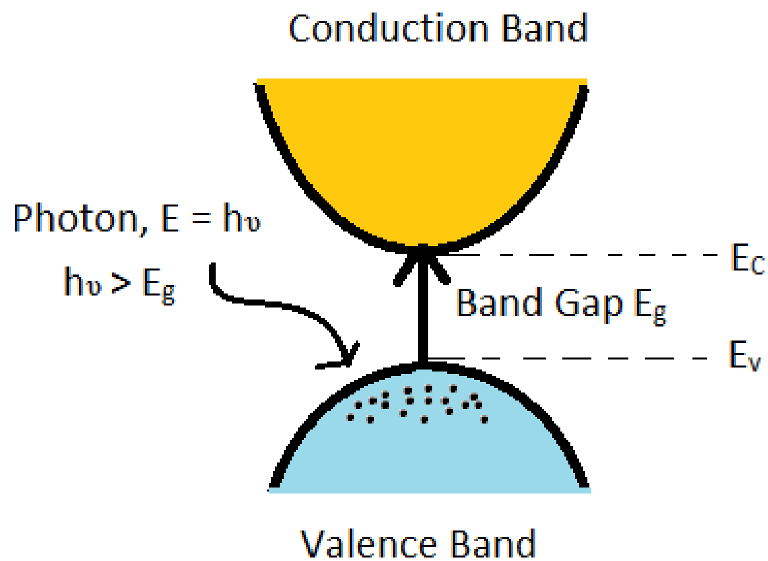

Figure 1.1: Simplified schematic of a direct band gap showing valence and conduction bands [1.2].

UNIVERSITY of the
WESTERN CAPE

Figure 1.1 depicts the instance of a direct band gap, where the valence band and conduction band share the same wave vector **k**. Consider excitation from electromagnetic radiation of energy E = hν, where h is Planck's constant and ν is the frequency of the light. In order to excite an electron out of the valence band and into the conduction band, the incoming photon has to be of energy $h\nu > E_g$ [1.3]. This process is known as optical generation, whereby excitation event increases the concentration of free charge carriers, namely, both electrons and the holes. Holes are thought of as positive charges which travel in the opposite direction to the electron. If $h\nu >> E_g$ the electron will be promoted across the band gap and into the conduction band with "extra" energy. This, however, is short lived, and the electron relaxes down to the lowest possible energy site in the conduction band. This process is known as thermalisation [1.4]. If $h\nu < E_g$ the photon would not have enough energy to excite and release the electron out of its

position in the valence band. In this instance, the photon energy is absorbed by the semiconducting material and put to work in some other process.

Another category of band gap exists in which the valence and conduction bands do not share the same **k** value. The charge carriers in the valence band belonging to an indirect band gap material as shown in figure 1.2 is not only excited by an energy $h\nu > E_g$, but requires an extra "push", usually in the form of momentum to overcome the band gap.

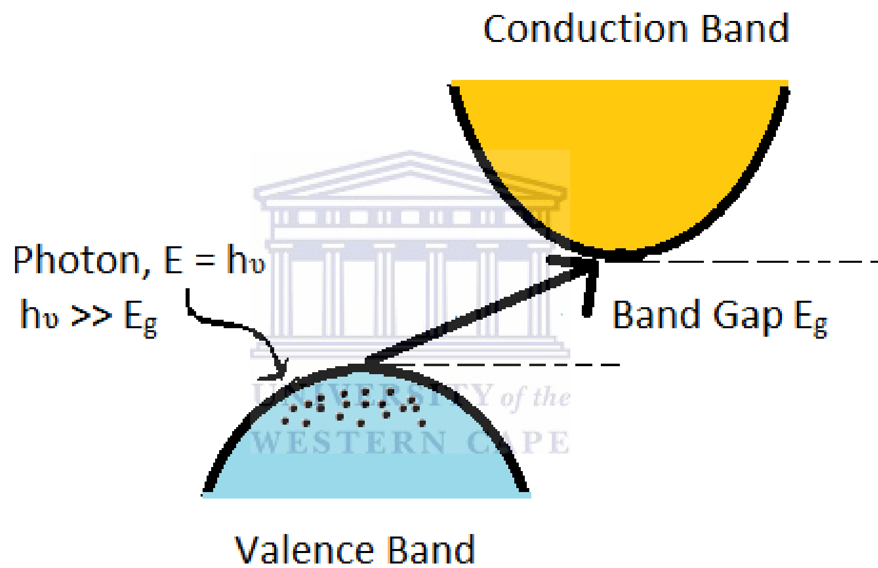

Figure 1.2: Schematic of an indirect band gap [1.2].

In order to generate electron hole pairs, an extra amount of energy is needed for the electron to overcome the energy gap. The surplus of energy may be obtained through a lattice vibration. The lattice vibration along with the impinging photon could promote the electron towards the conduction band, generating the electron hole pair [1.3]. Generating the charge carriers (the electron-hole pair), is the relatively simple part. Keeping them from recombining is more challenging.

For charge separation to be effective, the electrons are sent to one side, and the holes are sent to the other side of the device. This separation is made possible through the use of an electric field. The electric field is generated through the use of a device known as a p-n junction.

1.2.1 p-n Junctions

p-n Junctions are formed by bringing a p-type semiconductor in contact with an n-type semiconductor [1.3]. n- and p-type semiconductors are formed during a doping process, wherein impurities are added to the pure (intrinsic) semiconductor material such as silicon. Donor atoms are added to the intrinsic semiconductor to form the n-type semiconductor. These donor atoms are atoms which have a higher valence value (more free electrons) than that of the intrinsic atom, and therefore increases the concentration of electrons in the material. P-type semiconductors are formed by the addition of acceptor atoms into the intrinsic lattice; these atoms are of a lower valence value compared to the intrinsic atoms. They increase the acceptor site (holes) concentration in the material. Electrons and holes can thus be added to an intrinsic material with the use of dopants consisting of elements either of a lower or higher free electron value.

UNIVERSITY of the
WESTERN CAPE

In an n-type material, the majority carriers are the electrons while the minority carriers are the holes since there is a surplus of electrons compared to holes. In the p-type material the opposite is true. For efficient photo-conversion to take place, the diffusion lengths of the minority carriers have to exceed that of the photon absorption depths. To ensure that the charge separation is kept to a maximum, an electric field is needed, thus forcing the charge carriers to move opposite to each

other. This electric field is created at the junction where the two semiconducting materials meet. In the n-type material, the extra electrons flow across into the p-type material, and conversely in the p-type material there is an excess of holes which flows into the n-type material till a depletion region is formed [1.3]. The majority of the charge carriers are repelled by the internal electric field and moves toward their corresponding terminal. Figure 1.3 below depicts a schematic of a pn-junction.

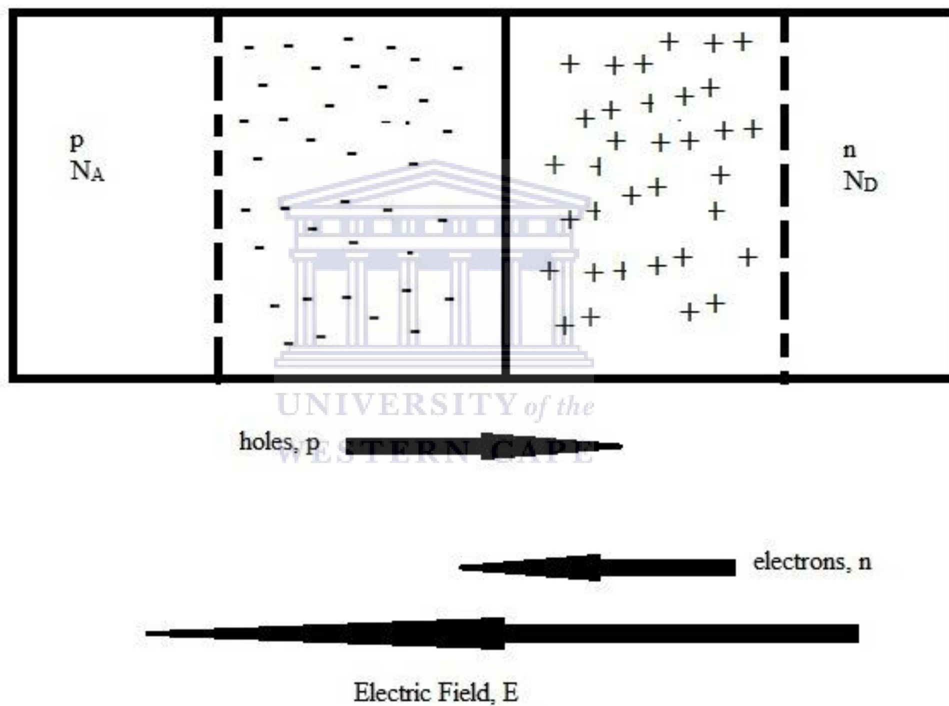

UNIVERSITY of the
WESTERN CAPE

Figure 1.3: Schematic of charge transfer across a pn-junction [1.2].

1.2.2 The Diode Equation

A solar cell as depicted in figure 1.4 below is a semiconducting device which has the potential to convert the radiant energy received from the sun into electrical energy with the help of p-n junction. The device is effectively known as a diode.

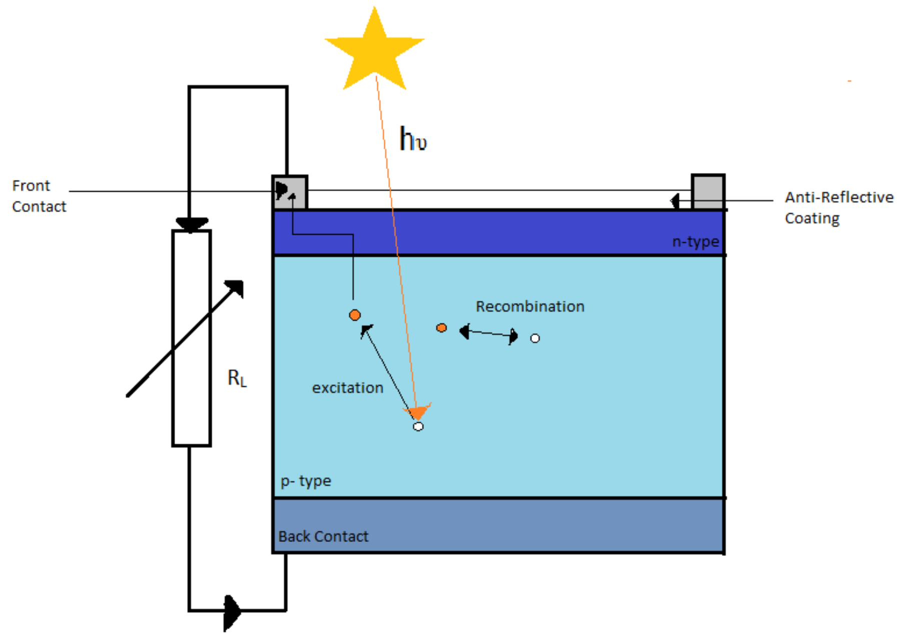

Figure 1.4: Schematic of a solar cell.

UNIVERSITY of the
WESTERN CAPE

Solar cells follow diode characteristics under illumination, causing a current to flow. For an ideal diode, the current can be expressed as [1.2]:

$$I = I_0 \left[\exp\left(\frac{qV}{kT}\right) - 1\right] - I_L \quad (1.1)$$

where q is the elementary charge, k the Boltzmann constant, T the absolute temperature, I_0 the reverse saturation current density, and I_L the illumination current. Figure 1.5 below shows a comparison of the properties of a diode in the dark and when illuminated.

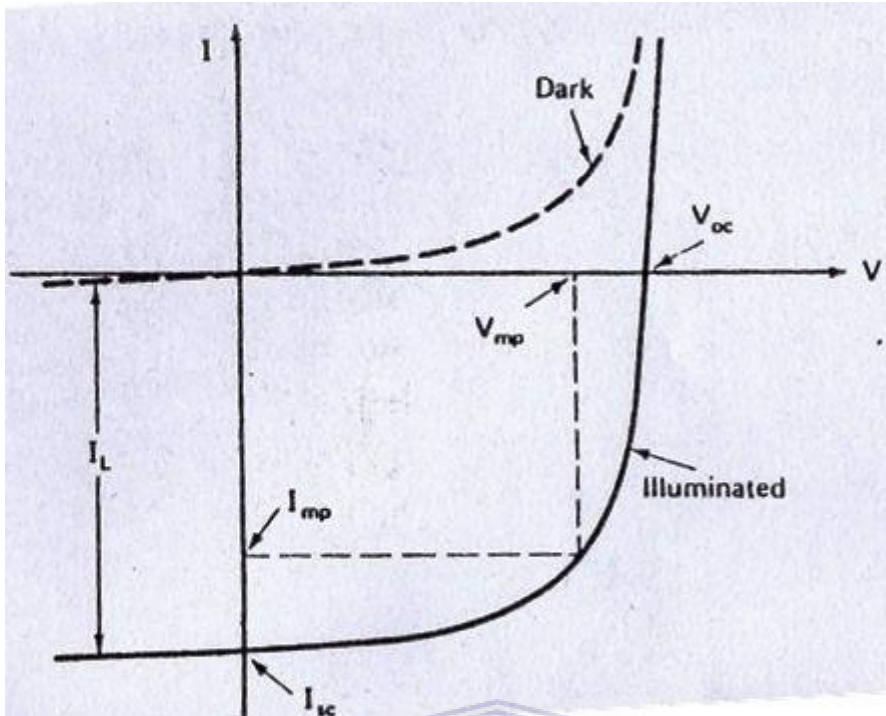

Figure 1.5: Properties of a diode under illumination and in the dark [1.2].

UNIVERSITY of the
WESTERN CAPE

1.2.3 Amorphous Silicon (a-Si)

Silicon is found in two structural forms, namely crystalline and amorphous, and is covalently bonded in both cases. In the former type the silicon atoms making up the crystal are periodically and equidistantly spaced and bonded to each other. On the other hand, the amorphous form has no specific order - the atoms are randomly spaced in a disordered fashion. Dangling bonds form due to uncoordinated silicon atoms and are not bonded ideally, leaving some valence electrons free [1.5]. These differences in structure influence the overall properties of the material. The introduction of hydrogen into the amorphous silicon network can be used as a doping mechanism, saturating and passivating the dangling bonds. A new form of a-Si is formed referred to as *hydrogenated amorphous*

silicon (a-Si:H). Figure 1.6 below contrasts the bonding arrangements between crystalline silicon (c-Si) and a-Si:H.

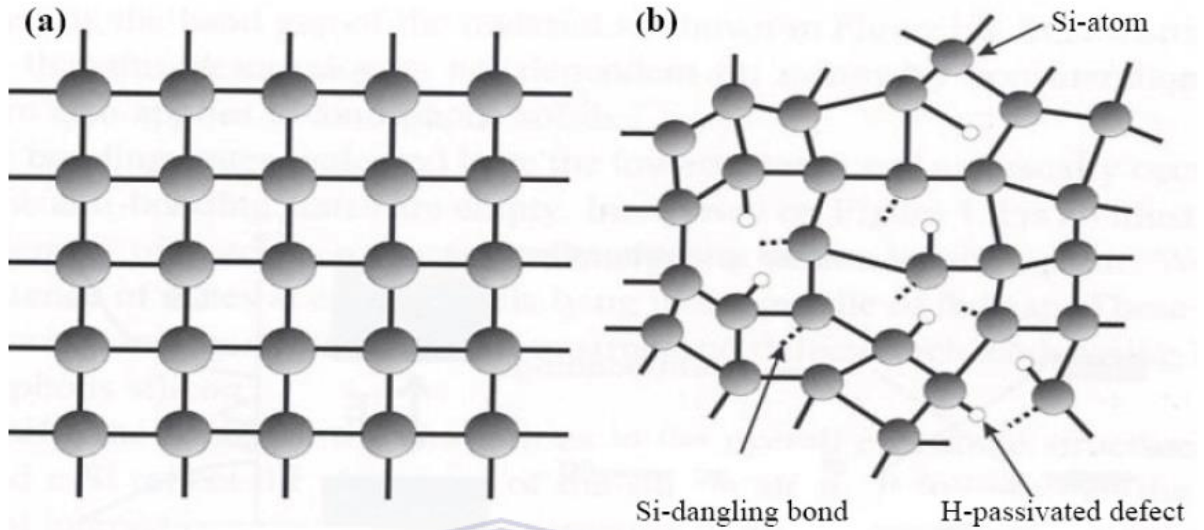

Figure 1.6: Depiction of (a) c-Si and (b) a-Si:H contrasting the bonding arrangements between the ordered crystalline silicon, and the disordered a-Si [1.5].

UNIVERSITY of the
WESTERN CAPE

The amorphous nature of the material influences the electronic and structural characteristics of silicon. The DOS for amorphous silicon is shown in figure 1.7 below, where an interpretation of the defect DOS state in the band gap region is depicted. These defect states acts as electron traps, which aid recombination, thereby diminishing the optoelecronic properties of the device which consists of a series of indirect band gaps.

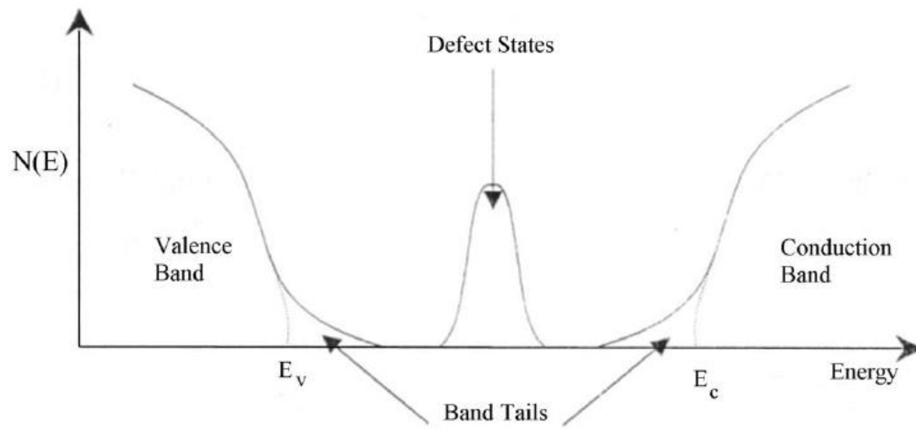

Figure 1.7: DOS diagram of a-Si showing the valence band and conduction band containing band tailing as well as defect states in the band gap [1.5].

The theory described above holds well for bulk single phase material solar cells, which are expensive to produce. Recently, much focus and attention has been placed on thin film solar cells. The drive for this stems from the need to use cheaper and flexible substrates, and to drive down the manufacturing costs of solar cells.

UNIVERSITY of the
WESTERN CAPE

1.2.4 Thin film solar cells

Thin films refer to coatings which are less than a micron (μm) thick and range up to hundreds of nanometers (nm). When developing a thin film solar cell, the material that is considered has to have specific properties. The manufacturing process must be cheap and reliable, and repeatability is important. The device itself should be non-toxic, and stable under extreme conditions [1.3]. The reduction in thickness means that the cell should be photo absorbent leading to a reduced diffusion length for the minority charge carriers. These materials can be

deposited at low temperatures by physical or chemical vapour deposition (CVD) techniques.

Polycrystalline and amorphous silicon contain natural defects as a consequence of the deposition [1.3]. These defects act as natural dopants in the thin film system, altering the electronic properties of the thin film much like the insertion of an impurity into the lattice of an intrinsic single crystal system. Photon generation of charge carriers can be used to describe the conversion process in a thin film solar cell as previously described. However, in an amorphous material such as a-Si the conduction and valence band do not always share the same wave vector as in direct band gap materials such as c-Si, and to excite an electron across the indirect band gap the photon energy is not enough. The electron requires an “extra push” which is received from momentum. Charge separation is achieved by a modified p-n junction known as a *p-i-n* junction.

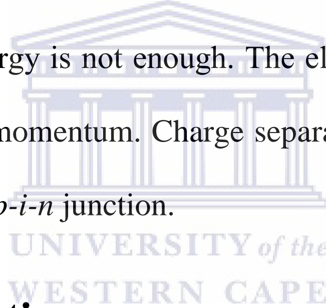

UNIVERSITY of the
WESTERN CAPE

1.2.5 p-i-n Junctions

Doping the intrinsic amorphous silicon with hydrogen shortens the diffusion lengths of the charge carriers through passivation of the dangling bonds. Absorption of photons is increased by using intrinsic amorphous material, as the selection rule imposed to the photon absorption in c-Si is no longer valid, and the entire system becomes relaxed [1.5]. In conjunction with the doped amorphous material, the resulting structure is known as a *p-i-n* junction as depicted in figure 1.8 [1.3]. The junction structure generates an electric field, as in the *p-n* junction, which drives charge separation. The electric field extends over a larger area of the device as compared to in a p-n junction, and, in theory, should exceed the total

thickness of the intrinsic region [1.3]. These junctions are not perfect and do exhibit shortcomings. Although the charge carriers have an extended lifetime within the intrinsic layer, the conductivity is not as effective as that of the doped regions. As the concentration of holes and electrons increase and converge to similar values, the probability of a recombination event increases. Impurities that exist in the amorphous intrinsic layer may negatively affect the electrical properties of the overall junction.

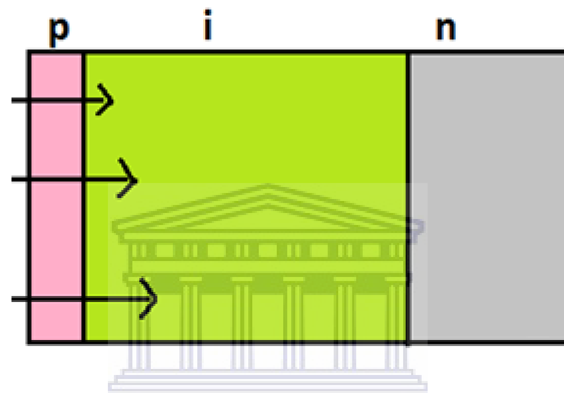

Figure 1.8: Simple schematic of p-i-n junction for thin film solar cells showing the direction in which the photon travels [1.3].

UNIVERSITY of the
WESTERN CAPE

For efficient charge separation a path of least resistance is needed by the flowing charge, thus decreasing the probability of a recombination event. Recombination occurs when the electron loses energy and meets back up with a hole, which decreases the overall conversion efficiency of the cell.

The device efficiency, η, can be expressed as the ratio of the power output to the power input. To increase the conversion efficiency of the solar cell, as well as improving the ability of the device to capture incoming photons, an anti-reflective coating is needed on top of the solar cell [1.3]. The anti-reflective coating (ARC) has to transmit light of "useful" frequency through to the bulk layer of the solar

cell with minimal absorption and reflection of the light. For this to transpire, the ARC should possess superior optical properties.

1.2.6 Anti-Reflective Coating (ARC's)

The reflection of light off smooth surfaces is significant. For a textured surface, the light photons are given a greater opportunity to penetrate the material due to secondary interaction with the material, and, therefore, the loss of light is greatly reduced. Texturing of surfaces is one way of minimising reflection losses; another method is through the use of specialised coatings.

The anti-reflection coating (ARC) mechanism is well known in industry, and is especially not new to that of the PV industry, where it is used on bulk and thin film solar cells. The function of an ARC is to minimize the loss of light to a reflection interaction. The reflection off a surface of light at normal incidence can be expressed as follows [1.2]:

UNIVERSITY of the
WESTERN CAPE

$$R = \left(\frac{n_1 - n_0}{n_1 + n_0}\right)^2, \quad (1.1)$$

where n_0 and n_1 are the refractive indices of the ambient medium and material medium respectively. The ambient medium through which the light travels is usually air which has a constant refractive index $n_0 = 1$. For material having a large difference in refractive indices, the reflectance will be high. To minimise the reflectance, the insertion of a single layer ARC with a perfectly tailored refractive index of optimal thickness on top of the solar cell is normally performed. The reflection is calculated according to

$$R = \left(\frac{{n_{ARC}}^2 - (n_0 n_1)}{{n_{ARC}}^2 + (n_0 n_1)}\right)^2, \quad (1.2)$$

where n_{ARC} is the refractive index of the anti-reflective coating, and n_0 and n_1 are as described before. For a minimum or zero reflectance at a specific wavelength the refractive index of the ARC should be calculated as follows [1.6] :

$$n_{ARC} = \sqrt{n_0 n_1}. \tag{1.3}$$

The optimum thickness, d, of the ARC must meet the quarter-wave optical thickness approximation

$$d = \frac{\lambda_0}{4n_{ARC}}, \tag{1.4}$$

where λ_0 is the wavelength where reflectance is a minimum.

A single layer ARC is the minimum requirement for mitigating the loss of light through reflection, and in some cases, multiple layers are employed, and a more complex form of the formulae described above hold true.

A number of materials are suitable for the role of an ARC, with the refractive indices ranging between 1.4 and 2.7 for these materials [1.6]. The deposition of the ARC onto the surface of the solar cell should be cheap and easy, while causing no damage to the active layer beneath it. Two main ARC's used in industry are titanium dioxide (TiO_2) as well as silicon dioxide (SiO_2) [1.7]. The refractive index of SiO_2 is far too low for the use as an ARC and does not improve the electrical characteristics of the solar cell module. TiO_2 is an effective ARC but provides no passivation to the defect states in the a-Si thin film, or to the electrical properties. Over the last couple of decades much focus has turned to silicon nitride (SiN_x) as an ARC.

UNIVERSITY of the
WESTERN CAPE

1.2.7 Silicon Nitride

In recent years silicon nitride (SiN_x) has received huge amounts of attention due to its versatility as a material, with applications in many industries [1.8]. The wide application of the material is due to the tuneable properties of the material, which depends on the specific deposition conditions and parameters. One such use is as an anti-reflective coating for multi crystalline solar cells, to enhance the light capturing and conversion efficiency of the device.

Stoichiometric amorphous silicon nitride (a-$Si_{1-x}N_x$) with x in range 1.33 is a metastable material, which deteriorates at high temperatures and high current densities [1.9].

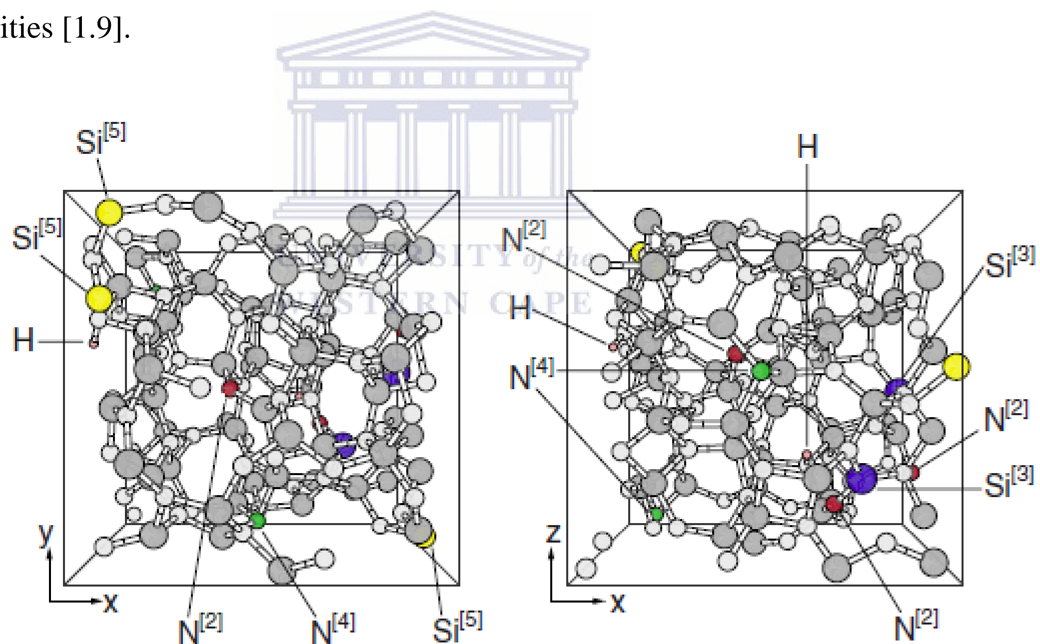

Figure 1.9: Depiction of a-Si_3N_4 at different orientations, the yellow and purple depicts the 5 coordinated Si atoms and the 3 coordinated atoms respectively, while the red and greed colours depict the 2 coordinated and 4 coordinated nitrogen atoms respectively [1.10].

$a\text{-}Si_3N_4$ as depicts in figure 1.9 consists of an edge sharing tetrahedral network such that each nitrogen atom is shared amongst three Si atoms at the corners of a planar triangle, forming a ridged network [1.11].

Similarly to silicon, silicon nitride (SiN_x) can be found in two structural forms: crystalline SiN_x ($c\text{-}SiN_x$) and amorphous SiN_x ($a\text{-}SiN_x$). The complex crystalline phase consists of two sub phases which are temperature dependent. At low temperatures the alpha (α) phase is present, as the material temperature increases the structure changes till the beta (β) phase takes over. The β-phase is characterised by a hexagonal space group. The amorphous structure of SiN_x has a typical bond length of 1.729 Å, which is comparable to that of other amorphous structures [1.11]. The focus of this study is to investigate amorphous silicon nitride structures, and no further focus will be given to the crystalline phases again.

UNIVERSITY of the
WESTERN CAPE

The density of states of $a\text{-}SiN_x$, like in a-Si:H, exhibits band tailing and defect states in the forbidden region. The DOS for $a\text{-}SiN_x$ is much more complex as shown in figure 1.10, as it involves two elements each with variant electronegativity which is chemically bonded to each other. The tail state occurs from the contributions of both elements.

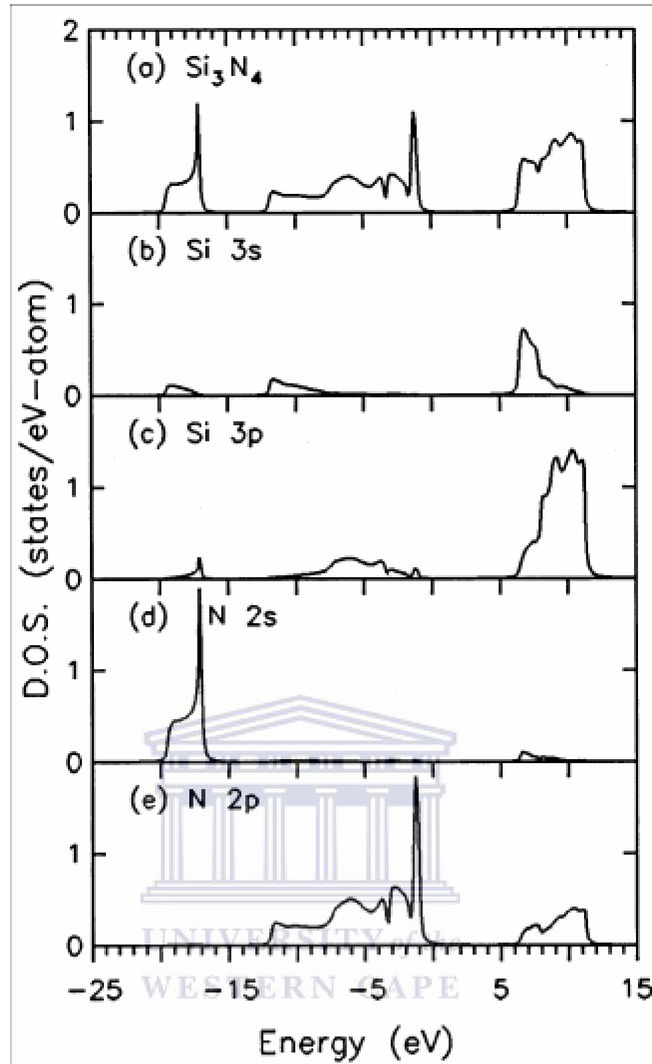

Figure 1.10: DOS of a-SiN$_x$ (a) depicts the average DOS of a-SiNx, (b) and (c) show the contribution of the Si atoms 3s and 3p bonding states respectively, (d) and (e) shows the nitrogen contribution to the DOS for the 2s and 2p states respectively [1.10].

a-SiNx As an Anti-Reflective Coating

Hydrogen incorporation during the deposition of silicon nitride passivates the dangling bonds which occur due to the amorphous nature of the material and the deposition conditions. Similarly to a-Si:H the class of material that results is known as *hydrogenated amorphous silicon nitride* (a-SiN$_x$:H). The hydrogen passivates the dangling bonds as well as relaxes the strained amorphous network

[1.11]. The inclusion of hydrogen in the bulk of the thin film has an influence on the structural and optical properties of the material.

For use as an ARC, a-SiN_x:H acts as a surface and bulk passivator, relieving the stress on the amorphous network of the a-Si:H solar cell, as well as the passivation of the grain boundaries in multi-crystalline (mc)-Si solar cells. The use of SiN_x:H in photovoltaics may influence charge separation, as the hydrogen incorporation provides low surface recombination velocities [1.12], thereby increasing the lifetime of the charge carriers and increasing the overall electrical efficiency of the solar cell.

The deposition conditions greatly influences the properties of a-SiN_x:H. The tuneable properties of SiN_x make it a suitable candidate as an ARC as well as for uses in the microelectronics. The chemical hardness and resistance to moisture absorption are all properties which elevates the status of SiN_x:H in industry.

UNIVERSITY of the
WESTERN CAPE

1.3 Deposition of a-SiN_x

There are many ways by which SiNx can be manufactured. The most popular method in industry is Plasma Enhanced Chemical Vapour Deposition (PECVD) [1.9, 1.13, and 1.14]. Other methods include RF sputtering, ion beam sputtering, electron cyclotron resonance plasma method and Hot Wire Chemical vapour Deposition (HWCVD) [1.15, 1.16, and 1.17]. Although PECVD is the most popular of the techniques used in industry [1.13], HWCVD has gained popularity due to its ease and simplicity of deposition, quality of the deposited thin films and the rate by which it can be manufactured [1.13].

PECVD presents the manufacturer with many drawbacks that HWCVD seems to have overcome [1.13, 1.18, and 1.19], like:

- The use of plasma leaves a dusty residue in the vacuum chamber.
- Plasma forms radicals as well as fast moving ions from the feed gas; these fast moving ions etch away at the surface of the film as it forms.

In HWCVD the plasma generators are replaced by metal filaments, usually made of tungsten (W) or tantalum (Ta). These filaments act as catalysers, stripping the gas to form radicals. The radicals are much softer on the developing thin film and causes little to no damage. The gas utilisation in such a system is high, ensuring good quality thin films with a high mass density, and minimal gas wastage.

1.4 Post deposition annealing of a-SiN_x

UNIVERSITY of the
WESTERN CAPE

Post-deposition annealing is used not only to evoke structural and physical changes to the thin film, but also to determine the stability at high temperatures. Placing the thin film under elevated thermal stress and exposing it to a new atmosphere may cause a rearrangement of the structural bonds, which ultimately has an effect on the physical properties of the material.

The creation of quantum dots (QD) and nanostructures may be the desired effect of annealing the as-deposited thin films at various temperatures and under various atmospheres. By controlling the size of the QD, photo emission as well as refractive indices can be controlled [1.20].

Si-H and N-H bond intensity peaks have been observed to decrease in the FTIR spectra as the annealing temperatures increase, this occurs as the hydrogen effuses out of the films. The rate of effusion of H_2 varies in a Si–rich thin film compared

to that of an N-rich thin film [1.21]. The movement of hydrogen out of the film at low annealing temperatures may cause an increased formation of defect states (dangling bonds and trap states). This comes about if insufficient rearrangements of bonds do not occur [1.22]. Passivation of the bonds and defects occur at higher annealing temperatures as the hydrogen is reincorporated into the bulk matrix [1.23, 1.24].

1.5 Aims and Outlines

The many experiments conducted by other research groups involved other deposition techniques including PECVD, magnetron sputtering and rf glow discharge. A few used high gas flow rates and the dilution of the reactant gas with inert gases such as helium, argon or nitrogen [1.23, 1.25]. The dilution of the reactant gas and deposition conditions is important in determining the properties of the thin films. For that reason the current study employed HWCVD using low flow rates of the reactant gases while simultaneously under dilution of hydrogen gas. Two types of SiN_x thin films are presented in the study, both demonstrating silicon rich structures, while the one type contains a higher nitrogen to silicon ratio. The as-deposited thin films were subsequently annealed isochronally for 30 minutes at low, medium and high temperatures ranging between 150°C and 1000°C to investigate the changes in the structural and optical properties.

The thin films were characterised by X-ray diffraction, Raman spectroscopy, Fourier transform infrared spectroscopy, elastic recoil detection analysis, atomic force microscopy, high resolution scanning electron microscopy, and UV-Vis spectroscopy. The theoretical background to each technique is discussed in

UNIVERSITY of the
WESTERN CAPE

chapter 2. The optical parameters discussed include the dielectric function, refractive index, Tauc band gap, and optical absorption. The optical parameters section in chapter two also includes the theory of the Effective Medium Approximation (EMA) used in solving the optical parameters.

Chapter three discusses the results of the two sets of thin films, comparing the as-deposited and post-deposition annealing films with respect to the structural changes which occurred in the thin films, as the response of the material to the heat treatment. The chapter serves as a comparison between the annealing response of the two types of SiN_x thin films described in the study. Included in chapter three is a section on using the EMA theory to build an optical model to solve the optical parameters described. The optical parameters were examined before and after annealing, which provided some insight into the structural changes which may have occurred as a result of the heat treatment.

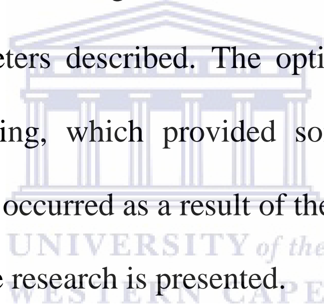
UNIVERSITY of the
WESTERN CAPE

Finally, a summary of the research is presented.

References

[1.1] J. J. Quinn, Kyung-Soo Yi, '*Solid State Physics, Principles and Modern Applications*', Springer-Berlin Heidelberg (2009).

[1.2] M. A. Green, '*Solar Cells- Operating Principles, Technology and System Applications*', Prentice-Hall, Inc, Englewood Cliffs (1982).

[1.3] J. Nelson, '*The Physics of Solar Cells*', Imperial College Press, UK (2003).

[1.4] A. Shah, '*Thin- Film Silicon Solar Cells*', EPFL Press, Switzerland (2010).

[1.5] R. A. Street, '*Hydrogenated Amorphous Silicon*', Cambridge University Press (1991)

[1.6] R. Kishore, S. N. Singh, B. K. Das, *Renewable Energy*, **33** (2007) 131.

[1.7] A. G. Aberle, *Solar Energy Materials & Solar Cells*, **65** (2001) 239.

[1.8] F. Alvarez, A. Valladares, *Revista Mexicana De Física*, **48** (2002) 528.

[1.9] F. Giorgis, C.F. Pirri, E. Tresso, *Thin Solid Films*, **307** (1997) 298.

[1.10] L. Giacomazzi, P. Umari, *Phys Rev B* **80**, (2009) 144201.

[1.11] F. de Brito Mota, J. F. Justo, and A. Fazzio, *J. Appl. Phys.*, **86**, (1999) 1843.

[1.12] A. El amrani, I. Mahiou, R. Tadjine, A. Touati, A. Lefgoum, *Renewable Energy*, **33** (2008) 2289.

[1.13] W. C. Tan, S. Kobayashi, T. Aoki, R.E. Johanson, S.O. Kasp, *J Mater Sci: Matter Electron, **20*** (2009) S 15.

[1.14] Z. S. Houweling, V. Verlaan, R. Bakker, C.H.M. van der Werf, Y. Mai, R.E.I. Schropp, '*Dielectric properties of Hot Wire CVD silicon nitride applied in a-Si TFTs*', (unpublished).

[1.15] M. Molinari, H. Rinnert, M. Vergnat, P. Weisbecker, *Materials Science*

UNIVERSITY of the
WESTERN CAPE

and Engineering, **B101** (2003) 186.

[1.16] H. Nagayoshi, M. Ikeda, K. Okushima, T. Saitoh, K. Kamisako, *Solar Energy and Solar Cells*, **48** (1997) 101.

[1.17] M. Molinari, H. Rinnert, M. Vergnat, *J. Appl. Phys.*, **101** (2007) 123532-4.

[1.18] B. Stannowski, C.H.M. van der Werf, R.E.I. Schropp, *Proc. Of the 3rd Intern. Conf. on Coatings on Glass*, Maastricht, (2000) 387.

[1.19] S.R. Jadkar, J.V. Sali, D.V. Musale, S.T. Kshirsagar, M.G. Takwale, *Solar Energy Materials & Solar Cells,* **71** (2002) 153.

[1.20] L. Jiang, X. Zeng, X. Zhang, *Journal of Non-Crystalline Solids,* **357** (2011) 3187.

[1.21] J.K. Holt, D.G. Goodwin, A.M. Gabor, F. Jiang, M. Stavola, H.A. Atwater, *Thin Solid Films,* **430** (2003) 37.

[1.22] A.K. Panchal, C.S. Solanki, *Thin Solid Films*, **517** (2009) 3488.

[1.23] G. Scardera, T.Puzzer, I. Perez-Wurfl, G.Conibeer, *Journal of Crystal Growth,* **310** (2008) 3680.

[1.24] T.C. Patil, P. Mahajan, S. Chakrabarti, *Superlattices and Microstructures*, **48** (2010) 190.

[1.25] Z. Lu, P. Santos-Filho, G. Stevens, M. J. Williams, G. Lucovsky, *J. Vac. Sci. Technol.* **A. 13** (1995) 607.

UNIVERSITY of the
WESTERN CAPE

Chapter 2: Experimental Methods

Understanding the deposition technique, the theory of gas flow and the interactions of the molecules is important. The conditions in the chamber during the deposition influence the characteristics and properties of the thin films, and ultimately dictate the behaviour which the thin films display during annealing.

2.1 Chemical Vapour Deposition

Chemical vapour deposition (CVD) describes the process by which thin solid films are deposited through a series of chemical reactions at high temperatures, and usually take place in the gaseous phase. The process of CVD was developed by Spear [2.1], and is depicted in figure 2.1.

UNIVERSITY of the
WESTERN CAPE

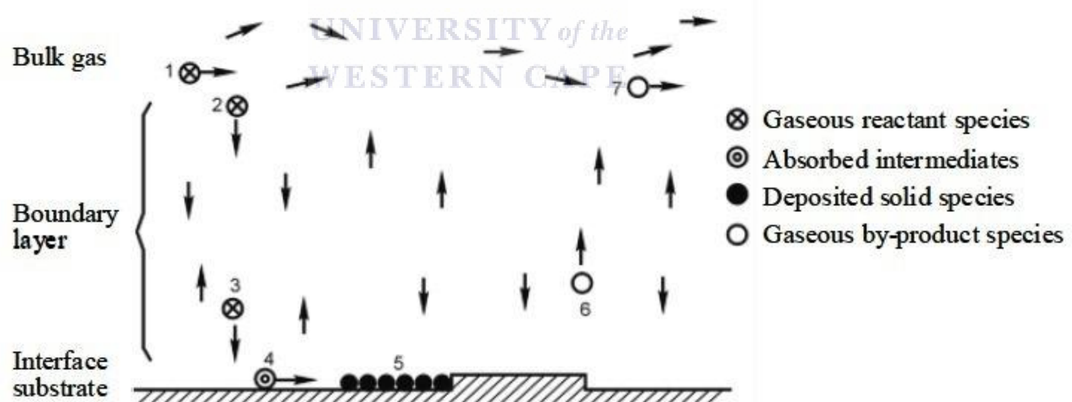

Figure 2.1: CVD process model depicting the gas phase reactions which may occur in the deposition chamber [2.2].

The first step in any CVD process is the forced flow of reactant gas into the evacuated chamber. As the gas flows into the system, diffusion and Stefan flow of the reagent gas through the boundary layer towards the substrate occurs [2.2].

Adsorption of gas species onto the substrate comes about as the gas phase reactions take place. As the reactions continue, desorption of the species from the substrate occurs, with diffusion and Stefan flow of the product gasses through the boundary layer into the bulk gas. The excess gasses are forced out of the reaction chamber and dealt with accordingly.

The CVD process involves the addition of a thin film on top of a substrate, which is intended for a specific purpose. The strength of the bonds formed in the thin film is dependent on the chemical reactions which take place and do not need any external solidification processes. These reactions occur at an atomic level and therefore, the films formed can be of the order of nano-metres to micro-metre thicknesses [2.2], this is dependent on many other deposition conditions, one such condition being the duration of the deposition.

The interactions of the gas molecules which occur during the CVD process can be explained using the gas laws and the kinetic theory of molecules. To understand and describe the movement of the gas, it is assumed that the interactions experienced by the gas molecules obey the ideal gas laws, and follows the assumptions that govern these gas laws [2.2].

The assumptions that the gas laws make are that the molecules are spherical in size, and the gas consists of a huge number of the small spherical particles. The volume of every sphere is much smaller than that actually occupied by the gas, and each molecule is independent of the next, and therefore do not exert a force on one another. The motion of the molecules is random in a rectilinear path, and the spheres can be considered to be rigid solids which experiences completely elastic collisions.

UNIVERSITY of the WESTERN CAPE

Ideal gasses conform to Boyles Laws for every temperature; this relationship was determined and described by Boyle in 1662. According to Boyle the product of the pressure (P) with the volume (V) yields a constant at a constant temperature. This can be expressed as

$$PV = const. \tag{2.1}$$

The volume of an ideal gas is proportional to the absolute of the temperature, and is inversely proportional to the pressure such that

$$PV = nRT, \tag{2.2}$$

where n is the number of moles of gas present in the system and R is the universal gas constant ($R = 8.31\ J.K^{-1}.mol^{-1}$).

UNIVERSITY of the
WESTERN CAPE

The total pressure felt inside the deposition chamber is made up of the sum of the individual gas pressures of the mixture of gasses inside the chamber. These individual pressures are known as the partial pressures of the gas, and the total pressure can be expressed as

$$P_{Tot} = \Sigma\, P_n, \tag{2.3}$$

where P_{Tot} is the total pressure due to the interactions of the gas, and P_n is the partial pressures of each individual gas molecules.

Gas kinetic theory describes the interactions of the particles making up an ideal gas with each other as well as with the deposition chamber.

The pressure experienced inside the chamber is due to the force per unit area exerted by the gas mixture on the inside surface of the chamber, and can be represented by

$$P = {}^{1}/_{3}\,(Nmu_{av}^{2}), \tag{2.4}$$

where P is the pressure measured in any units of pressure (it does not have to be SI units, but can be converted mathematically), N is the molecular number per unit volume, m the mass of the molecules, and u_{av} the mean velocity of the gas molecules [2.2].

The Maxwell-Boltzmann distribution function describes a profile of velocities which a molecule of gas could have at a certain temperature. This is needed since it is known that molecules do not all travel at the same speed. The Maxwell-Boltzmann distribution is expressed as

$$f(u) = 4\pi \left(\frac{m}{2\pi kT}\right)^{3/2} (u^2) \exp\left(-\frac{mu^2}{2kT}\right), \qquad (2.5)$$

where f(u) is the probability of a molecule having a certain velocity, m is the mass of one molecule, k is the Boltzmann constant ($k = 1.32 \times 10^{-23}$ J.K^{-1}), u is the speed of one molecule, and T the temperature measured in Kelvin. The most probable velocity at which any molecule would be moving in the system is expressed by the quantity u_p; this corresponds to the point at which f(u) is a maximum such that [2.2]

$$u_p = \sqrt{\frac{2kT}{m}} = \sqrt{\frac{2RT}{M}}. \qquad (2.6)$$

M is the molar mass of the gas. The mean velocity can be calculated by the mathematical average of the velocity (u_{av}) distribution:

$$u_{av} = \int_0^\infty uf(u)du = \sqrt{\frac{8kT}{\pi m}} = \sqrt{\frac{8RT}{M}}. \qquad (2.7)$$

The root mean square velocity, u_{rms} is the square root of the average squared velocity expressed as

$$u_{rms} = \sqrt{\int_0^\infty u^2 f(u)du} = \sqrt{\frac{3kT}{\pi m}} = \sqrt{\frac{3RT}{M}}. \qquad (2.8)$$

UNIVERSITY of the
WESTERN CAPE

The varying quantities of velocity are used to describe the behaviour a molecule will have at a certain temperature. These quantities are related such that u_{av} = $1.128u_p$, and $u_{rms} = 1.225u_p$.

Gas molecules are said to be able to travel at speeds greater than that of sound at ambient temperatures. However the paths of these fast moving gas particles are not linear, and often resemble zigzag-like patterns as shown in figure 2.2 below. These gas particles partake in random collisions which slow down their movement, allowing them to change the direction. The average distance which a molecule will travel before a collision is known as the mean free path described as:

$$\lambda = \frac{kT}{\sqrt{2}\pi P d^2}, \quad (2.9)$$

where k is the Boltzmann constant, T is the temperature in Kelvin, P is the pressure and d the diameter of the molecules. The mean free path differs from the average distance between molecules, as small molecules with high velocities due to thermal excitation will not collide often, thus resulting in larger mean free paths.

UNIVERSITY of the
WESTERN CAPE

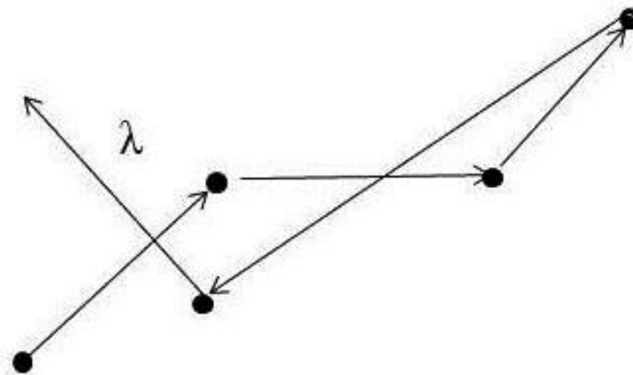

Figure 2.2: Movement and mean free path travelled by gas molecules [2.2].

A system at equilibrium containing gaseous molecules moving over a specific area conforms to the bounds and assumptions of the Knudsen Law.

The law assumes an equal distribution, as well as the random motion of the gaseous molecules within the system. When considering an area (dA) inside the chamber the probability that a molecule will move from the solid angle (dω) is equated to $\frac{d\omega}{4\pi}$. For molecules moving in a velocity range of u + du the number of molecules (dN) moving over dA in a certain unit of time can be expressed as

$$dN = \frac{d\omega}{4\pi} n. f(u). u. \cos(\theta) . dA, \quad (2.10)$$

where n describes the number of molecules per unit volume, f(u) the Maxwell-Boltzmann distribution function, θ the angle of inclusion formed between the normal line of the area, dA, and the solid angle as shown in Figure 2.3 below.

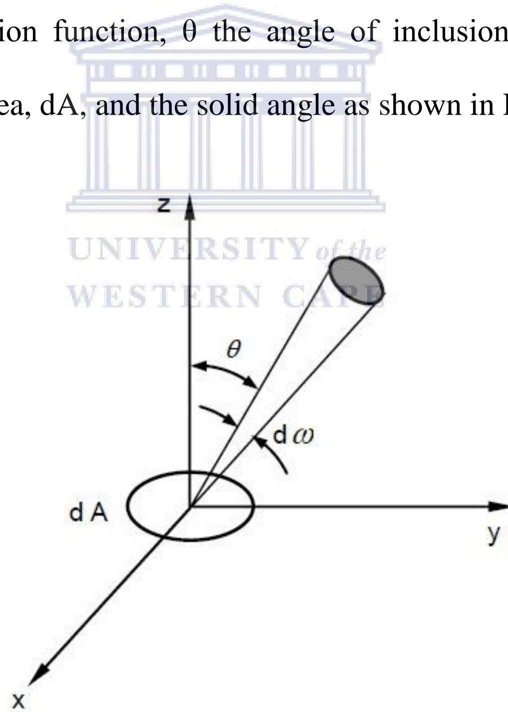

UNIVERSITY of the
WESTERN CAPE

Figure 2.3: Schematic representation of geometry involved in Knudsen's Law [2.2].

Taking the integral of the velocity from zero (0) to infinity (∞), the total number of molecules impinging on dA can be shown as

$$N = \frac{d\omega}{4\pi} n.\cos(\theta).dA \int_0^\infty u.f(u)\,du = \frac{d\omega}{4\pi}. \qquad (2.11)$$

The cosine law shows that the number of molecules impinging on dA is directly proportional to the cosine function taken with respect to the inclusion angle (θ). Knudsen explained the importance of the law by assuming the complete adsorption of molecules onto a solid surface, and where after the molecule is released. The direction in which the molecule travels after it is released from the surface is not dependent on the prior motion before adsorption had taken place. The assumptions of Knudsen have been confirmed through experimental observation.

The time (τ) a molecule spends adsorbed on the surface is an important factor in understanding the CVD mechanism. This can be expressed as [2.2]:

$$\tau = \tau_0 \exp\left(\frac{Q}{RT}\right), \qquad (2.12)$$

where τ_0 is the period of vibration of the molecule, Q the heat of adsorption, and R and T have their usual meanings as explained earlier.

UNIVERSITY of the
WESTERN CAPE

The number of gas molecules per unit time and per unit area can be calculated using the cosine law and is given by

$$n_0 = \frac{1}{4} n.u_{av}. \qquad (2.13)$$

The molecules taking part in a CVD process must be delivered from the bulk gas in order to be incorporated into the lattice of the substrate. This is defined through the use of the Hertz-Knudsen Law which describes the movement of the gas molecules onto the substrate:

$$F = \frac{P}{\sqrt{2\pi MRT}} \text{ [mole.cm}^{-2}\text{.s}^{-1}\text{]}, \qquad (2.14)$$

where P is the pressure of the gas molecules measured in Torr, M is the molar mass in g.mol^{-1}, and T is the absolute temperature in Kelvin. The Hertz-Knudsen Law can also be written as:

$$F = 3.35 \times 10^{22} \frac{P}{\sqrt{MRT}} \text{ [mole.cm}^{-2}\text{.s}^{-1}\text{]}. \quad (2.15)$$

2.1.1 Hot Wire Chemical Vapour Deposition

Hot Wire Chemical Vapour Deposition (HWCVD) can be described by the catalytic decomposition of the feed gases over a hot wire filament in an ultra-high vacuum (UHV) chamber, with radicals forming that settle on the cooler substrate, thus contributing to the growth of the thin film. The deposition of silicon and silicon alloys by HWCVD dates back to 1979, with the deposition of a-Si:H by Weismann *et al*. [2.3]. The results of the experiment were not well received due to the poor quality material being deposited. Matsumura *et al.* [2.4] later improved on this by depositing near-device quality material with properties comparable to thin films deposited by the more favoured and industrialised Plasma Enhanced Chemical Vapour Deposition (PECVD).

Studies have been conducted with the addition of hydrogen to the feed gases to enhance the deposition characteristics of the thin films [2.5]. It has been reported that while depositing a-Si:H, the substrate temperature has little effect on the electronic properties of the resulting thin film, while the moderate dilution of silane feed gas with hydrogen in specific ratios during deposition has a positive effect on the electronic structure of the material, and very little structural effect. Dilution of the feedstock gas above a threshold yields interesting structural

UNIVERSITY of the WESTERN CAPE

effects, which could cause the onset of proto-, nano-, or micro-crystalline material [2.5].

An in-depth description of the MV HW-System used for the deposition of the thin films in this study is given by Arendse [2.6]. A cross section of the HW chamber is shown in figure 2.4.

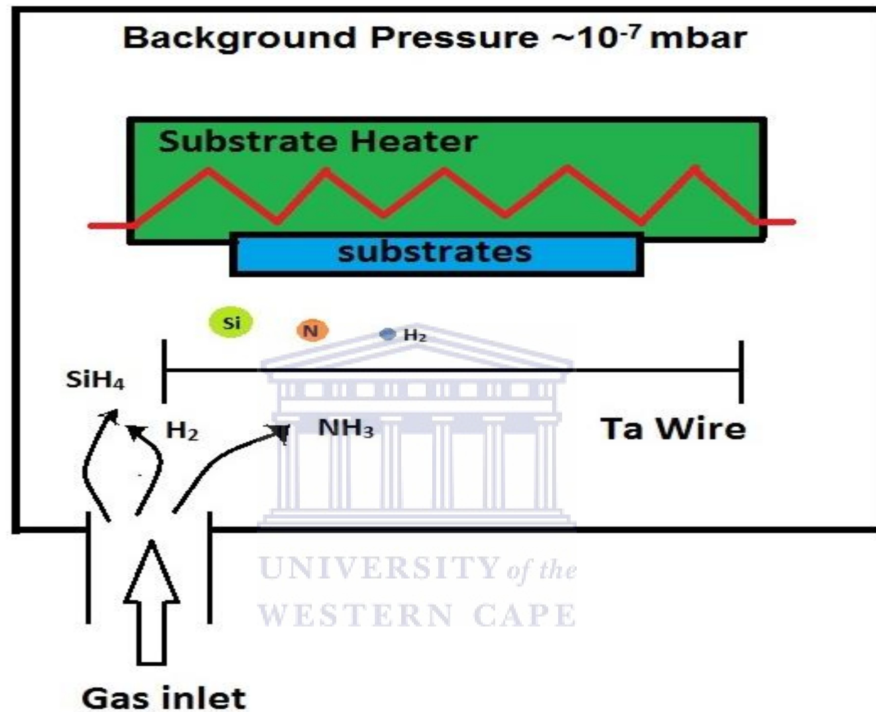

UNIVERSITY of the
WESTERN CAPE

Figure 2.4: A cross sectional schematic view of the deposition chamber, showing the substrate heater, substrate holder, hot Ta filament and precursor gases.

2.1.2 Deposition of SiN_x

PECVD is the favoured technique for the deposition of silicon and silicon alloys in industry as it offers a high growth rate and cost feasibility for large scale productions. However, the thin films deposited by PECVD are of a lower quality compared to those deposited by HWCVD. The difference in film quality is due to the high hydrogen incorporation of the PECVD deposited thin films, as well as the

constant ion bombardment resulting from the breakdown mechanism of the feed gases [2.7].

Parameters such as the base/background pressure in the chamber, the flow rates of the feed gases and the pressure at which these gases are fed into the chamber during the deposition dictate the quality and the characteristics of the thin film [2.7]. The orientation of the substrates in relation to the hot filament, as well as the size and shape of the deposition chamber may result in the unique properties of the deposited thin films.

To achieve a high growth rate in any deposition chamber, a high rate of decomposition of the source gases is required [2.8]. As mentioned above, the rate at which the feed gases are flowed into the chamber affects the properties of the thin film. Verlaan *et al*. [2.9] has shown that the N/Si ratio decreases as the flow of silane increases; the decomposition of the ammonia gas is suppressed as the silane flow rate increases [2.10]. The growth rate of the thin films would increase and the resulting thin films would be Si-rich SiN_x.

The deposition of SiN_x under a constant flow rate, but varying the gas pressure during the deposition, has an effect on the nitrogen content of the subsequent thin films [2.9]. As the gas pressure increases more species of silane and ammonia are brought into contact with the catalysing hot filament, resulting in the elevated presence of atomic hydrogen in the deposition chamber. The occurrence of the atomic hydrogen during the gas phase reactions promotes the incorporation of nitrogen into the thin films, thereby increasing the N/Si ratio.

The addition of hydrogen gas into the deposition chamber during the deposition facilitates the incorporation of nitrogen into the matrix of the thin films, while, at

UNIVERSITY of the
WESTERN CAPE

the same time etching the hot filament to remove any silicides which may have formed, thus restoring the catalysing ability of the hot filament.

2.2 Thin Film Deposition

2.2.1 Sample Preparation

Two types of substrates were prepared during the deposition of the thin film, Corning 7059 glass and p-doped crystalline silicon (c-Si) with a <100> orientation polished on one side. The thin films deposited on the Corning 7059 glass were characterised using X-ray diffraction and Raman spectroscopy, while the thin films deposited on the c-Si substrates were characterised using the following techniques: UV-visible optical spectroscopy in reflection mode, Fourier Transform Infrared Spectroscopy, ion-beam based measurements, High resolution Scanning electron microscopy and Atomic Force Microscopy.

UNIVERSITY of the
WESTERN CAPE

The substrates were cut to size 7 cm x 4 cm and rigorously cleaned before being used for the deposition. The substrates underwent ultra-sonication in acetone, and then in methanol, each for 5 minutes, where-after the c-Si underwent an additional one minute treatment in a 2% hydrofluoric acid (HF) solution to remove the native oxide layer from its surface. The substrates were then dried in a natural ambient of a fume hood and placed under UH vacuum immediately thereafter.

2.2.2 Deposition Parameters

Two sets of depositions were carried out. In each set a tantalum (Ta) wire was chosen as a filament; the wire temperature (T_W) was kept at 1490°C during the deposition while the substrate temperature (T_S) was maintained at 240°C. The

filament temperature was deliberately lowered compared to depositions for hydrogenated amorphous or nanocrystalline silicon, to investigate a new deposition regime for hydrogenated amorphous silicon nitride, compared to other laboratories. The silane (SiH_4) and the hydrogen flow (H_2) rates were kept constant at 5 standard cubic centimetres per minute (SCCM) and 20 SCCM respectively and the overall gas pressure in the deposition chamber was 100 μbar. In the first sample set (MW 303) the deposition parameters described above were used, coupled with addition of 2 SCCM of ammonia gas (NH_3). In the second set (MW 304), the ammonia gas flow rate was changed to 7 SCCM while the other parameters were kept constant. In both sets of experiments, the distance between the wire and the substrate was kept constant (~4 cm), and the total flow rate of gas varied between 27 SCCM and 32 SCCM into the chamber. The deposition conditions are summarised in table 2.1 below.

UNIVERSITY of the
WESTERN CAPE

Table 2.1: A summary of the conditions within the vacuum chamber during the deposition process.

Parameter	Condition
Wire Temperature (T_W) [^{o} C]	1490
Substrate Temperature (T_S) [^{o} C]	240
Deposition Pressure [mbar]	0.1
NH_3 (MW 303/MW 304) [SCCM]	2/7
H_2 Flow [SCCM]	20
SiH_4 Flow [SCCM]	5

Before the deposition commenced a background pressure of ~10^{-7} mbar was attained in the chamber, and the substrates were transferred from the load lock.

The shutter was inserted between the filaments and the substrates, and the substrate heater was set. Once the substrate temperature had reached its set point the wire was turned on and ramped up to 1490°C. The wire was treated for two minutes with 20 SCCM of H_2 gas, and the deposition gas flux was set. The feed gas was opened and allowed to flow into a mixing chamber to allow the pressure to build up. The deposition pressure was controlled through the use of an automatic butterfly valve. At the end of the deposition the wire was once again treated with a steady flow of H_2 gas at 20 SCCM for two minutes. The treatment of the wire with hydrogen prolongs the life span of the wire, as well as etching away at any silicide's which may have formed on the surface of the wire. The wire was switched off and the remaining gas was purged from the gas feeding line. The samples were left to cool under vacuum until it reached room temperature, after which they were removed from the chamber and characterised.

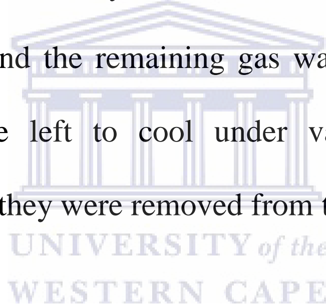
UNIVERSITY of the
WESTERN CAPE

2.2.3 Annealing

Predictions should be formulated for the behaviour of SiN_x:H used in optical and microelectronic devices before and after heat treatment. During heat treatment structural changes occur accompanied by hydrogen effusion. This process can be illustrated with the use of a theoretical model describing the bond evolution which may have occurred due to the addition of heat, and the extra energy placed into the bonding system [2.11]. For SiN_x the transformations of the structural properties of the thin film involves the breaking of $(Si_xN_y)\equiv$Si:H and $(Si_xN_y)\equiv$SiN:H bonds by exposing the thin films to elevated temperatures. During the bond rearrangements of the thin film, defect states may be introduced into the

matrix; these defect states include dangling bonds belonging to either silicon or nitrogen, depending on whether the films are silicon-rich or nitrogen-rich. During thermal annealing the following chemical reactions may take place [2.11]:

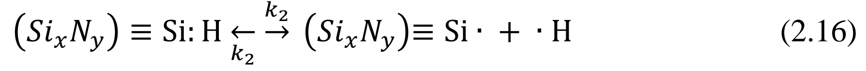

$$(Si_xN_y) \equiv \mathrm{Si{:}H} \underset{k_2}{\overset{k_2}{\leftarrow\rightarrow}} (Si_xN_y) \equiv \mathrm{Si}\cdot + \cdot\mathrm{H} \qquad (2.16)$$

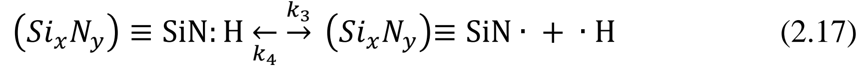

$$(Si_xN_y) \equiv \mathrm{SiN{:}H} \underset{k_4}{\overset{k_3}{\leftarrow\rightarrow}} (Si_xN_y) \equiv \mathrm{SiN}\cdot + \cdot\mathrm{H} \qquad (2.17)$$

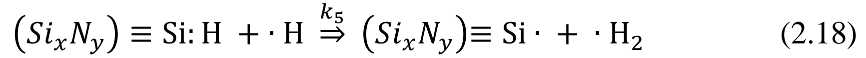

$$(Si_xN_y) \equiv \mathrm{Si{:}H} + \cdot\mathrm{H} \overset{k_5}{\Rightarrow} (Si_xN_y) \equiv \mathrm{Si}\cdot + \cdot\mathrm{H_2} \qquad (2.18)$$

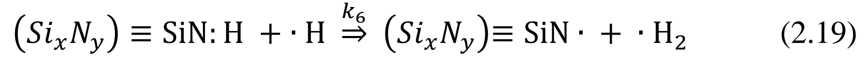

$$(Si_xN_y) \equiv \mathrm{SiN{:}H} + \cdot\mathrm{H} \overset{k_6}{\Rightarrow} (Si_xN_y) \equiv \mathrm{SiN}\cdot + \cdot\mathrm{H_2} \qquad (2.19)$$

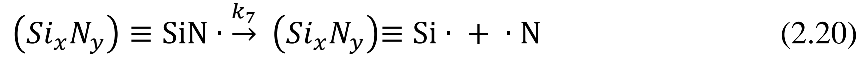

$$(Si_xN_y) \equiv \mathrm{SiN}\cdot \overset{k_7}{\rightarrow} (Si_xN_y) \equiv \mathrm{Si}\cdot + \cdot\mathrm{N} \qquad (2.20)$$

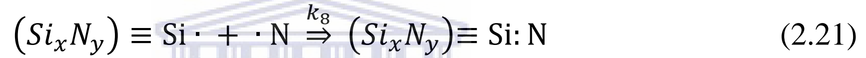

$$(Si_xN_y) \equiv \mathrm{Si}\cdot + \cdot\mathrm{N} \overset{k_8}{\Rightarrow} (Si_xN_y) \equiv \mathrm{Si{:}N} \qquad (2.21)$$

UNIVERSITY of the
WESTERN CAPE

Equations (2.16) and (2.17) describe the breaking and reformation of the (Si_xN_y)≡Si:H and (Si_xN_y)≡SiN:H hydrogen-containing bonds respectively. Equations (2.18) and (2.19) describes the other possible breaking mechanisms which may occur, and it is assumed that the formation of hydrogen molecules occur when any mobile hydrogen atom comes into contact with an immobile bonded hydrogen within a distance $r_h < 1.0$ nm. The breaking of nitrogen bonds with the formation of free hydrogen is depicted through the use of equation (2.20), with equation (2.21) describing the reverse process, whereby SiN_x is formed again. The rate at which hydrogen is lost can be described through the use of equation 2.22 [2.12].

$$\Delta A = C(A_0 - A)\exp(-\frac{E_a}{kT}), \qquad (2.22)$$

where ΔA is the decrease in absorbance of the N-H and or the Si-H modes from a temperature T, A_0 is the Absorbance measured in the as-deposited sample, E_a is

the activation energy barrier for H in a single rate bond reduction, k the Boltzmann constant, T the temperature in Kelvin and C is a constant. The actual rate at which hydrogen is lost may differ from that calculated, and is dependent on the type of bonds formed, the x value, and the method in which the thin film was deposited and the source gases used [2.13].

Annealing experiments were conducted under vacuum (1.33×10^{-6} mbar) at iThemba Labs, Faure in Cape Town. The annealing experiments were performed in an Elite Thermal System with a quartz tube and an isolated element. The heating element was allowed to ramp up to the set point before the element was turned on, and the ramping rate was controlled by a *k*-type thermocouple.

Post deposition structural and optical changes were induced through thermal annealing. The annealing was done isochronally for 30 minutes under vacuum for a range of temperatures. Before the annealing could commence the samples were systematically cut into approximate 1 cm by 1 cm squares using a diamond scribe pen. A grid was constructed consisting of 1 cm^2 blocks; each block had a row and column designation. Each square was characterised fully before and after annealing.

UNIVERSITY of the
WESTERN CAPE

Four samples, two from each sample set, were placed in a quartz annealing boat and loaded into a carousel placed under vacuum. The temperature control was set and only once the present value on the display had reached the set point, was the element switched on. The boat containing two c-Si, and two Corning substrates was pushed to the centre of the oven and exposed to the high temperature. Annealing started at 150°C and increased in 50°C increments up until 500°C. The next temperature set were chosen as 600°C; 700°C, and 1000°C. At 1000°C only

c-Si substrates were used, as the Corning 7059 glass cannot withstand such extreme temperatures. At the end of the isochronal annealing session, the boat containing the annealed samples were pulled into the carousel and allowed to cool under vacuum while the next set of samples were annealed. Once the samples were sufficiently cooled, the system was vented and flushed with nitrogen gas to prevent post-deposition oxidation from occurring.

2.3 Analytical Techniques

2.3.1 X-Ray Diffraction (XRD)

2.3.1.1 Introduction

UNIVERSITY of the
WESTERN CAPE

X-ray diffraction (XRD) is a non-destructive technique conducted under an atmospheric ambient and is used in the analysis of phase identification, crystal structure and crystal orientation of the material. The wavelength of an X-ray photon is comparable to that of the interatomic distances separating the atoms [2.14]; the use of a small probe size of the x-rays compared to the size of the particles under investigation makes x-rays the perfect tool for the investigation of the long range bonding order in the thin film sample under analysis.

2.3.1.2 Theory

Crystal Structure

A crystal may be considered as a series of periodically spaced atoms in a solid which spans the area of space in three dimensions. Not all solids are crystals as

they do not meet the requirement of periodicity, such as glass, and materials in this category are known as amorphous. Figure 2.5 below shows a point lattice, each dot represents an atom in the crystal structure in three dimensions.

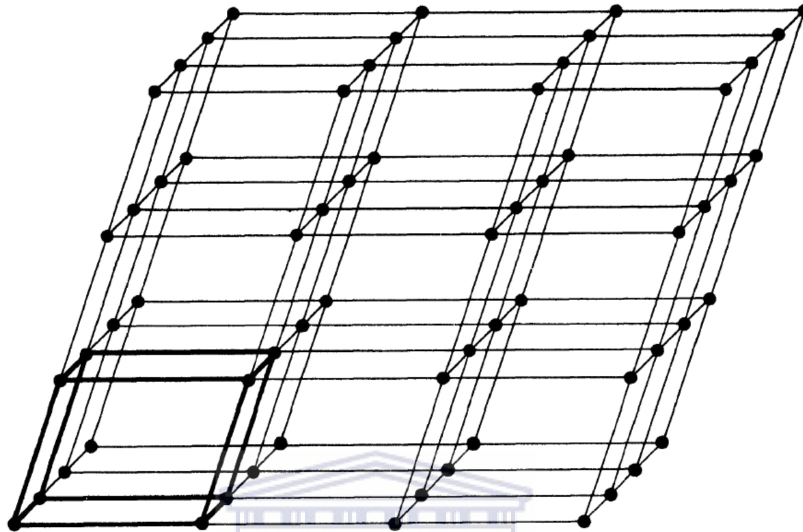

Figure 2.5: Three dimensional point lattice [2.15].

The point lattice, when viewed from one direction, will be the same if viewed from any other direction, and is created by dividing the space up into three sets of planes. The direction of any line drawn on the point lattice is generic, as the origin can be selected at any one point on the lattice. The direction of any line passing through the origin in the point lattice may be described through the use of indices [u v w]. Since the origin may be arbitrarily selected, any line drawn parallel to that of the given line would have the same set of indices. Lines drawn in the opposite direction and having negative indices are represented with a bar on top of the number. A set of directions related by symmetry are known as directions of a form and are depicted by the indices being encased in angular brackets, e.g. <111> is symmetrical to $[111], [\bar{1}11], [1\bar{1}1], [11\bar{1}]$. The indices are always

UNIVERSITY of the
WESTERN CAPE

written in the smallest integer form through the mathematical manipulation of the numbers [2.15].

In a cubic system selecting a single cube in the point lattice forms the unit cell. The unit cell is described by three vectors, namely $\vec{a}, \vec{b}, \vec{c}$, making up the lengths of the cell, as well as three angles between the lengths α, β, γ. The vectors originate from an arbitrary selected origin at any lattice point, and the angles are measured between the vectors. Collectively, the vectors and angles depicted in figure 2.6 below are known as the crystallographic constants.

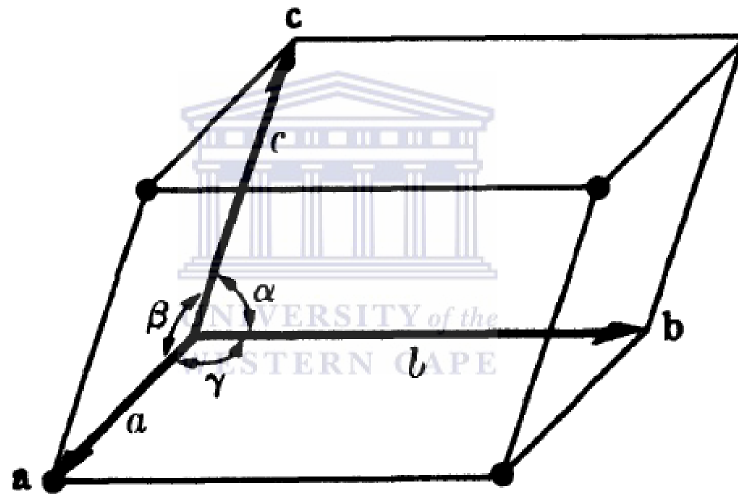

Figure 2.6: Unit cell showing crystallographic constants [2.15].

A primitive cell contains only one lattice point per cell while a non-primitive lattice, such as body-centred, face-centred and base-centred cells, contains more than one point per cell. The number of lattice points per unit cell may be calculated by:

$$N = N_i + \frac{N_f}{2} + \frac{N_c}{8}, \tag{2.23}$$

where N_i is the number of interior points, N_f is the number of points found on the face of the cell, and N_c is the number of points at the corner of the cell.

The lattice points forming a non-primitive cell may be translated through space like those in a primitive cell. The translations and operations of the variation in the crystallographic constants in a point lattice gives rise to space groups in the Bravais lattice, allowing for a maximum of 14 variations in the Bravais lattice whose characteristics are given in Table 2.2 below.

Table 2.2: Bravais lattice orientations [2.15].

System	Axial lengths and angles	Bravais lattice	Lattice symbol
Cubic	Three equal axes at right angles $a = b = c, \ \alpha = \beta = \gamma = 90^\circ$	Simple Body-centered Face-centered	P I F
Tetragonal	Three axes at right angles, two equal $a = b \neq c, \ \alpha = \beta = \gamma = 90^\circ$	Simple Body-centered	P I
Orthorhombic	Three unequal axes at right angles $a \neq b \neq c, \ \alpha = \beta = \gamma = 90^\circ$	Simple Body-centered Base-centered Face-centered	P I C F
Rhombohedral*	Three equal axes, equally inclined $a = b = c, \ \alpha = \beta = \gamma \neq 90^\circ$	Simple	R
Hexagonal	Two equal coplanar axes at 120°, third axis at right angles $a = b \neq c, \ \alpha = \beta = 90^\circ, \ \gamma = 120^\circ$	Simple	P
Monoclinic	Three unequal axes, one pair not at right angles $a \neq b \neq c, \ \alpha = \gamma = 90^\circ \neq \beta$	Simple Base-centered	P C
Triclinic	Three unequal axes, unequally inclined and none at right angles $a \neq b \neq c, \ \alpha \neq \beta \neq \gamma \neq 90^\circ$	Simple	P

* Also called trigonal.

UNIVERSITY of the WESTERN CAPE

Miller Indices and Diffraction

The lattice planes of a crystal structure displaying a high degree of order are all parallel to each other in a unit cell. A set of integer values, *hkl*, may be used to index the lattice planes such that $\frac{a}{h}, \frac{a}{k}, \frac{a}{l}$ are the points at which the planes intersect

the unit cell. The integer values are known as Miller indices and are represented by round brackets, for example (110) and (111). Figure 2.7 below depicts an example of lattice planes.

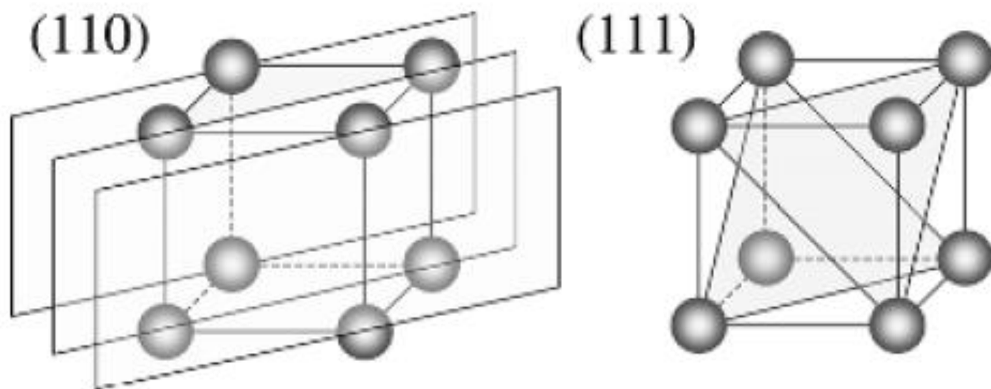

Figure 2.7: Lattice planes showing (110) and (111) planes for a simple cubic arrangement [2.14].

UNIVERSITY of the
WESTERN CAPE

The distances separating two adjacent planes, known as the interplanar spacing d_{hkl}, is specific to a particular set of Miller indices. For a simple cubic arrangement of atoms, the interplanar spacing is dependent on the crystallographic constant and the specific Miller indices:

$$d_{hkl} = \frac{a}{\sqrt{h^2+k^2+l^2}}. \tag{2.24}$$

In general for the diffraction pattern to be a maximum,

$$2d_{hkl} sin\theta_B = \lambda. \tag{2.25}$$

Equation 2.25 known as the Bragg [2.16] equation has to be obeyed, where λ is the wavelength of the impinging radiation, d_{hkl} the interplanar spacing, and θ_B the Bragg angle, the point at which the intensity is the greatest.

The Bragg equation is derived by considering any arbitrarily arranged crystallographic lattice plane as shown in figure 2.8 where the planes in the crystal are separated by an inter-planar distance d_{hkl}. A beam of X-rays is impinged upon

the planes at an angle θ. A path difference is experienced by the impinged radiation as it is reflected by the atoms. This difference is dependent on the arrangement of atoms making up the crystal which the radiation interacts with; the path difference can be represented as Δ_1 and Δ_2. The sum of the parts is equal 2dsin θ, for any angle θ. Constructive interference will take place for the reflected beam if, and only if, the path difference equals a multiple of the wavelength

$$2dsin\theta_B = n\lambda, \qquad (2.26)$$

where n is the order of reflection. Since Bragg's law can be derived for any crystal structure, the only requirements for the calculation of Bragg's law would be the Miller indices and the crystallographic constraints of the crystal structure.

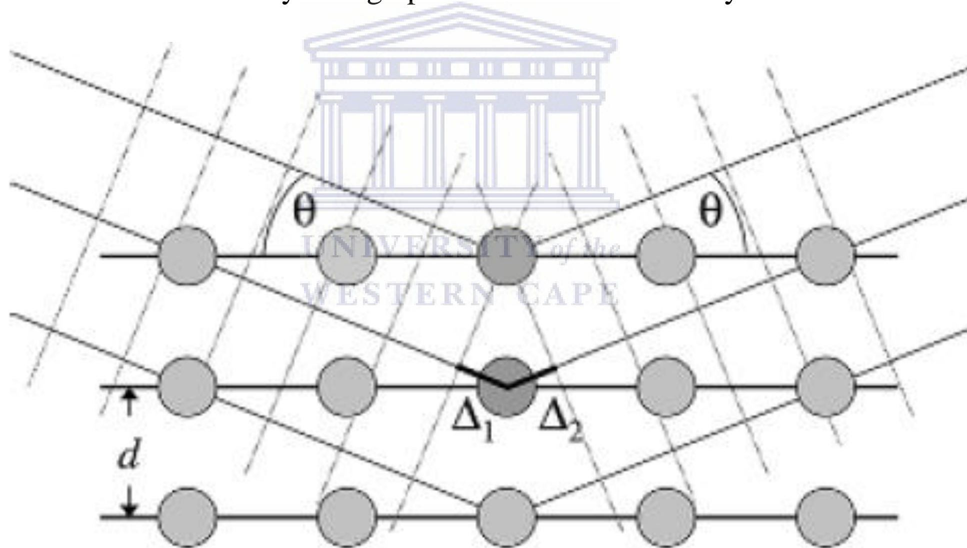

UNIVERSITY of the
WESTERN CAPE

Figure 2.8: Diffraction scattering in a crystal plane with d_{hkl} spacing [2.14].

2.3.1.3 Experimental

X-ray diffraction was performed on samples deposited on Corning 7059 glass using an X' Pert PRO Panalytical X-ray powder diffractometer situated at the Council for Scientific and Industrial Research (CSIR) in Pretoria, operating at 45 kV and 40 mA in reflection geometry. Measurements were performed at 2θ-

values ranging from 5 to 90° with a step size of 0.026°, using a Copper $K_{\alpha 1}$ radiation with a wavelength of 1.5406 Å as the X-ray source. The instrument was fitted with an automated sample changer connected to a Windows XP controlled computer for easy data acquisition. XRD was also conducted on two samples deposited on c-Si substrates with a <100> orientation using a BRUKER axs D8 ADVANCE diffractometer located at iThemba Labs in Faure, Cape Town. The diffractometer was operated using 45kV and 40 mA in reflection geometry. The 2θ scan was conducted in the range 7 to 67° with a step size of 0.04° with Copper $K_{\alpha 1}$ as the X-ray source. A schematic of a general X-Ray system is shown in Fig 2.9 below.

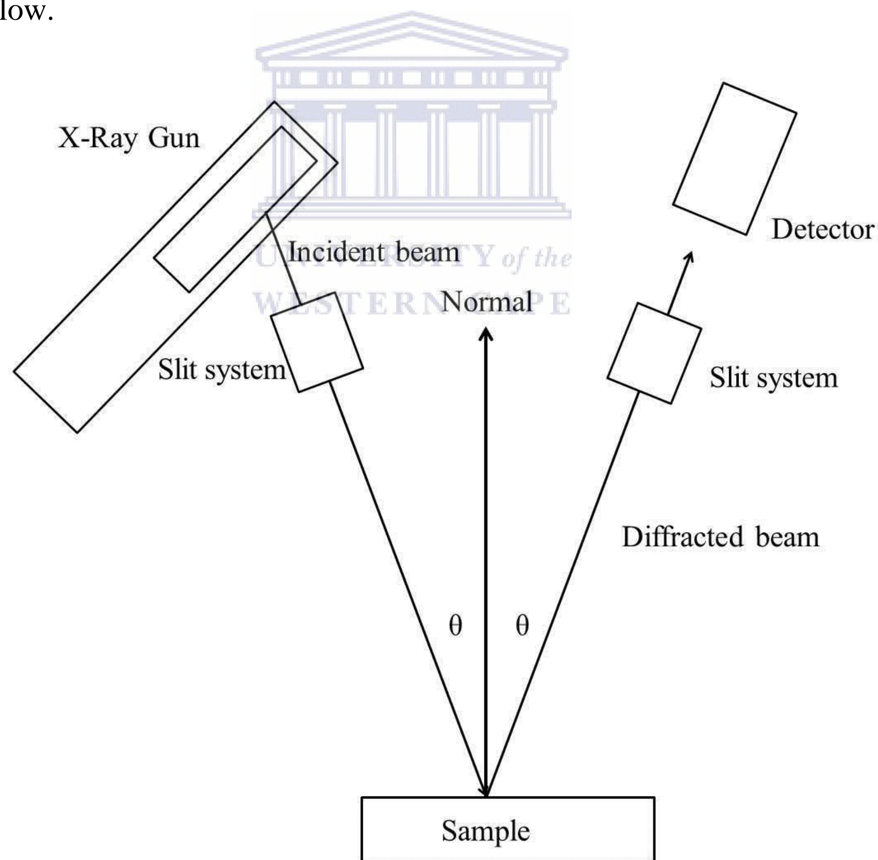

Figure 2.9: Schematic diagram depicting X-Ray diffraction.

2.3.1.4 XRD of Silicon Nitride

Silicon nitride thin films of both sets MW 303 and MW 304 were deposited on Corning 7059 glass using the conditions highlighted in Table 2.1 , and were characterised using XRD to determine the long range bonding order. Figure 2.10 shown below is a representative XRD diffraction pattern for the as-deposited sets belonging to both MW 303 and MW 304. The diffraction pattern shows the amorphous nature of the as-deposited silicon nitride thin films. Each set of was deposited under varying conditions by HWCVD, and characterised to be amorphous, this is seen by the absence of any crystalline features.

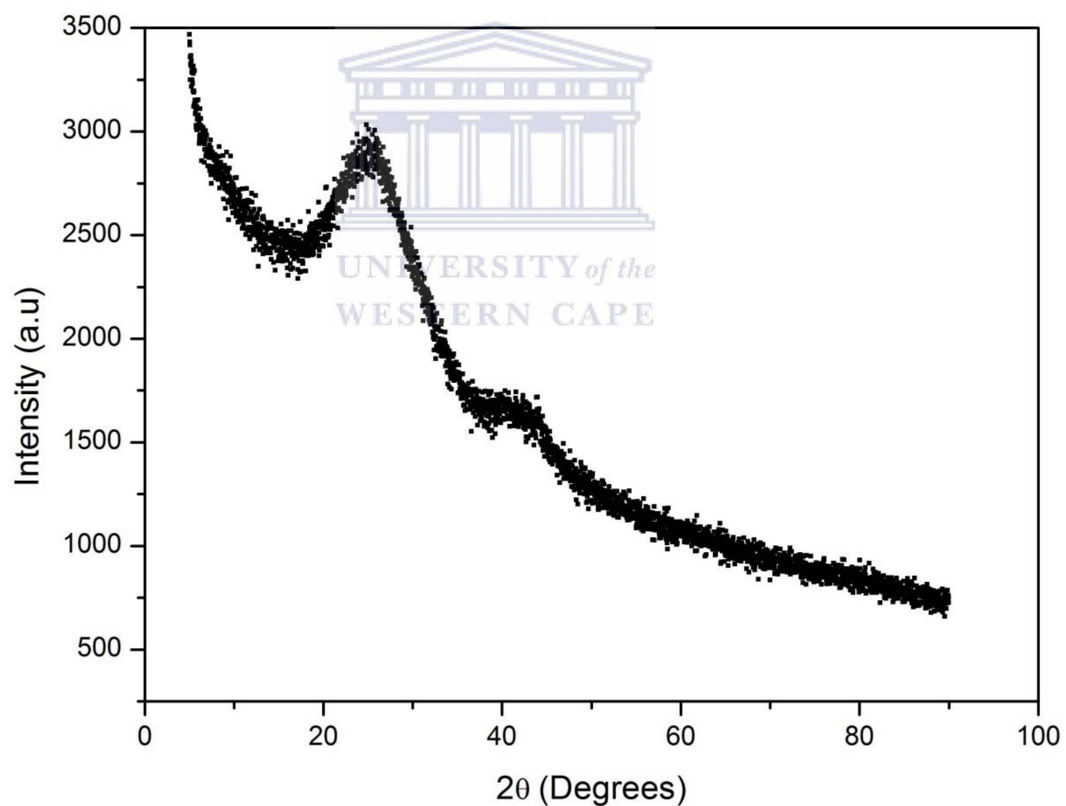

UNIVERSITY of the
WESTERN CAPE

Figure 2.10: Representative XRD diffraction pattern of the amorphous nature of the as-deposited silicon nitride thin films for both sets, MW 303 and MW 304.

2.3.2 Raman Spectroscopy

2.3.2.1 Introduction

Raman spectroscopy is a vibrational technique used to quantify the chemical and structural form of the material under analysis. The main underlying process at work is known as Raman scattering, which involves the inelastic scattering of light due to an interaction with the vibrating molecules in the material. As the light scatters off the molecules, small changes in the short range bonding order of the atoms in the material can be detected. The theory describing the scattering process is given by W. E Smith *et al.* [2.17] the following section presents a summary thereof, highlighting the important points.

2.3.2.2 Theory

UNIVERSITY of the
WESTERN CAPE

Electromagnetic radiation impinged on the surface of a thin film is either transmitted through the thin film, absorbed, or scattered off the surface of the thin film. Raman Spectroscopy utilises the radiation which is inelastically scattered off the surface of the thin film, ignoring all other processes which may have occurred [2.17].

In spectroscopy measurements the radiation used is often described by the wavenumber (ω) of the radiation, rather than the wavelength (λ) of the incident radiation. These quantities are related through the following operations [2.17]:

$$\lambda = \frac{c}{\nu} \quad (2.27)$$

and

$$\omega = \frac{\nu}{c} \quad (2.28)$$

where ν is the frequency of the propagating light, and c the speed of light.

The equations above show the relationships between the wavelength and the wavenumber - they are inversely related to each other. In Infrared (IR) spectroscopy a range of wavenumbers are used to characterise the sample, in comparison to Raman spectroscopy where a monochromatic and single energy photons are impinged onto the surface of the sample. The single energy beam is scattered from the molecules as it interacts with the sample. A Raman signal does not need to match any energy gaps or differences between the ground state and excited state to be detected. Instead, in Raman spectroscopy, the detected photon is one vibrational unit of energy different from the incident beam.

The impinging beam of radiation interacts with the molecule creating a distortion (polarisation) of the surrounding electron cloud, forming virtual states. The virtual states are unstable and short-lived, and as the electrons relax, a photon is re-radiated. Photons scattered by electrons are done so elastically by Rayleigh scattering, and involve interactions with the electron cloud. Nuclear motion is another form of scattering which may occur when radiation is impinged on the surface of the thin film. During nuclear motion, an energy transfer between the photon and the nucleus takes place, where after the photon is inelastically scattered. This scattering process describes Raman scattering where the scattered photon is dissimilar to the incident photon by one vibrational unit of energy.

UNIVERSITY of the
WESTERN CAPE

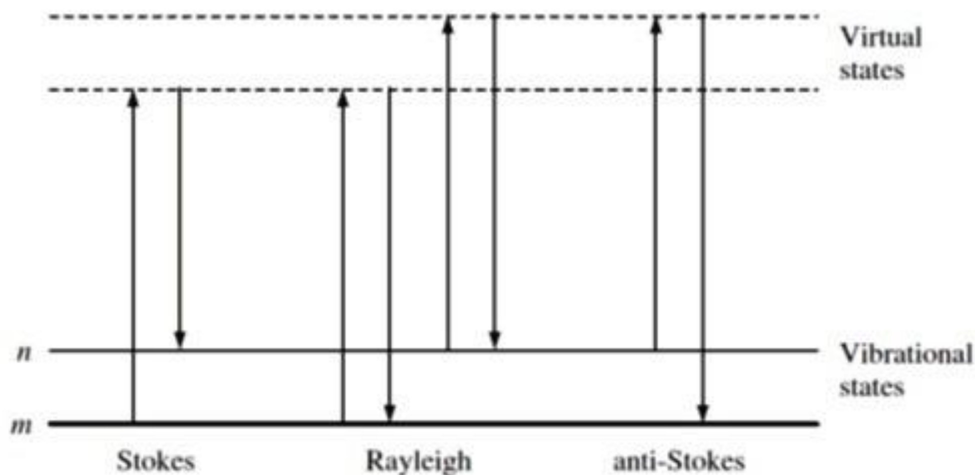

Figure 2.11: The basic process for one vibration, Rayleigh and Raman scattering, m indicates the ground state, and n indicates an excited state [2.17].

UNIVERSITY of the
WESTERN CAPE

The energy of the virtual states formed during electronic interactions is dependent on the energy of the laser used to polarise the electrons, as an interaction of the photons with matter takes place. The most prevalent process to take place is the Rayleigh scattering as it is easier to excite electrons than induce nuclear motion. Molecules are usually located in their lowest energy level (m), but this is not usually the case, as molecules could contain thermal energy. Thus the molecule could be found in a higher energy level (n). Since molecules could have two different energy levels, this leads to two types of Raman scattering as seen in figure 2.11:

- Stokes scattering occurs when a molecule in the ground state (m) absorbs some of the energy of the impinging photon and is subsequently promoted to a higher vibrational state (n). During a Stokes scattering event a transfer of energy between the photon and the molecule takes place, leaving the molecule in an excited state.

- Anti-Stokes scattering occurs when an excited molecule at a higher energy is scattered by the photon to a lower ground state energy (m). In the Anti-Stokes scattering, the molecule transfers energy to the photon as it drops down to the ground state.

Intense Raman scattering signals arise from vibrating molecules, which consequently leads to the polarisation of the electrons surrounding the vibrating molecule. The largest scattering events are obtained from a symmetrically vibrating molecule.

Vibrations of Molecules

The ball and spring model is the simplest model that can be used to describe the bond between atoms. The atoms as depicted in figure 2.12 on either side of the spring would adhere to Hooke's law as the atoms begin to oscillate on the spring after gaining some energy.

UNIVERSITY of the
WESTERN CAPE

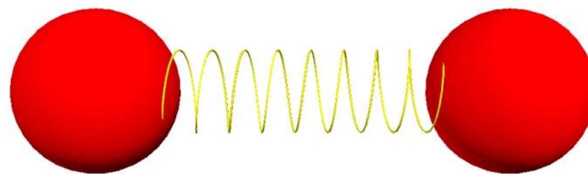

Figure 2.12: Ball and spring representation of bonded atoms.

Hooke's law

The frequency of vibration for the two masses on the ends of the spring can be related to Hooke's law [2.17]:

$$\nu = \frac{1}{2\pi c}\sqrt{\frac{K}{\mu}}, \tag{2.29}$$

where K is the spring constant which describes the bond strength, c is the speed of light, and μ is the reduced mass defined as:

$$\mu = \frac{M_A M_B}{M_A + M_B}, \tag{2.30}$$

where M_A and M_B are the masses of atoms A and B respectively.

The use of Hooke's law to understand the energies of vibration shows that the lighter atoms will vibrate at higher energies compared to heavier atoms, and that the spring constant describes the stiffness and strength of the bond. The vibration of two atoms weakly bonded together would have a slow and stretched out vibrational frequency compared to those strongly bonded atoms whose vibrational frequency would be higher.

The movement of a vibrating molecule can be described through the use of degrees of freedom. Three degrees of freedom are used to describe the translational motion of the molecule, and another three degrees of freedom is used to describe the rotational motion. In a linear molecule only two types of rotations are possible. In a system containing N number of atoms, the number of possible vibrational degrees of freedom and the number of vibrations would then amount to 3N – 6 for all molecules except linear molecules, and 3N – 5 possible degrees of freedom for linear molecules.

UNIVERSITY of the
WESTERN CAPE

A linear diatomic molecule such as O-O experiences a simple stretch motion when excited. The movement induces a change in polarization of the electron cloud surrounding the molecule as the molecule begins to vibrate symmetrically about the centre. The polarization of the electron cloud by the impinging light brings about nuclear motion, giving rise to a Raman signal being detected. The movements of a triatomic molecule are not as simple. These molecules may

undergo three modes of vibrations, symmetrical and asymmetrical stretching as well as a deformation or bending vibrations, as shown in figure 2.13.

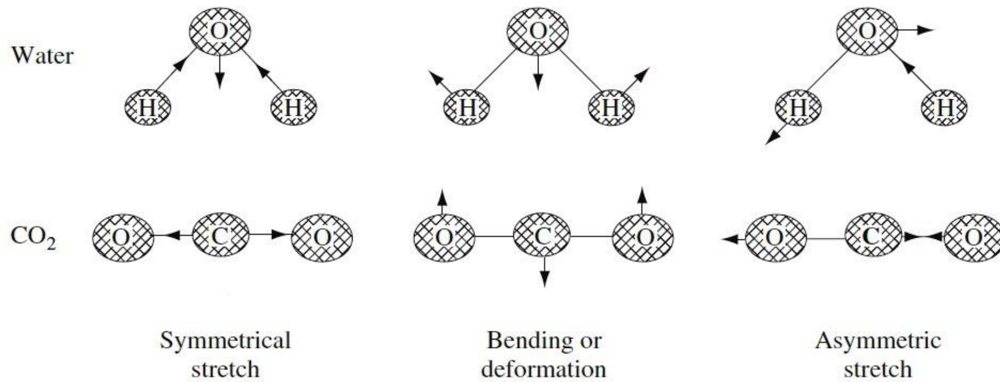

Figure 2.13: Linear and non-linear triatomic molecule showing the three bending motions [2.17].

UNIVERSITY of the
WESTERN CAPE

The degree to which a material may be polarised depends on a physical quantity, known as the polarisability (α) of the material, and its product with the electric field (E) of the impinging light gives the expression for the dipole (μ) which gives

$$\mu = \alpha E. \tag{2.31}$$

The polarisability of the electron cloud can be broken down into component form such as α_{XX}. The first X refers to the direction of the polarisability of the molecule, and the second X is the polarisation of the impinging photon. The dipole can be expanded out of matrix form as:

$$\mu_x = \alpha_{XX}E_X + \alpha_{XY}E_Y + \alpha_{XZ}E_Z. \tag{2.32}$$

Similar expressions exist for μ_Y as well as μ_Z.

The intensity of a beam scattered during the Raman scattering process can be expressed as:

$$I = KP\alpha^2\omega^4, \tag{2.33}$$

where K is a constant, P is the power of the laser, α the degree of polarisability of the molecule, and ω the frequency of the impinging light source. From the above equation it can be seen that two parameters are controllable by the user that may affect the intensity of the Raman scattering.

2.3.2.3 Experimental setup

The Raman scattering experiments were conducted on SiN_x samples deposited on the Corning 7059 glass substrates at the University of Groningen, Groningen, The Netherlands, using a Jobin Yvon Triplemate 64000 micro-Raman system equipped with a N_2-cooled CCD detector coupled to an Olympus BX40 microscope. An Argon (Ar) laser operated in the green wavelength (λ = 514.3 nm) region of the electromagnetic spectrum measured over a wide range of Raman shifts between 20-3000 cm^{-1}, utilising a step size of 0.5 cm^{-1}.

UNIVERSITY of the
WESTERN CAPE

Mode Identification

The amorphous silicon matrix to which nitrogen is incorporated presents two prominent peaks at the low wavenumber region of the Raman shift. The transverse acoustic (TA) and the transverse optical (TO) modes are located around 160 cm^{-1} and a broad peak around 480 cm^{-1} respectively. The broadened TO peak consists of the longitudinal acoustic (LA) mode as well as the longitudinal optical (LO) mode for the silicon matrix incorporated into it [2.18]. The width of the peaks increases with an increase in nitrogen content as the ring structure undergoes modification [2.18].

Si-H wagging and stretching modes are detected between 640-680 cm^{-1} and 2000-2200 cm^{-1} respectively [2.18]. The stretching modes may be located at higher

wavenumbers as the nitrogen content increases, placing increasing stress on the matrix of the thin films [2.18].

In a silicon-rich sample the 2TO scattering peak of the silicon matrix is located between 800-1000 cm^{-1} [2.18], while the SiN_x peak will be incorporated into the 2TO peak and will be found at around 850 cm^{-1} [2.18].

Figure 2.14 shows a deconvoluted Raman spectrum of a silicon-rich SiN_x sample. Features belonging to the amorphous silicon matrix situated at 160 cm^{-1} and 480 cm^{-1} shows the TA and TO peak containing the LA and LO peaks embedded within it.

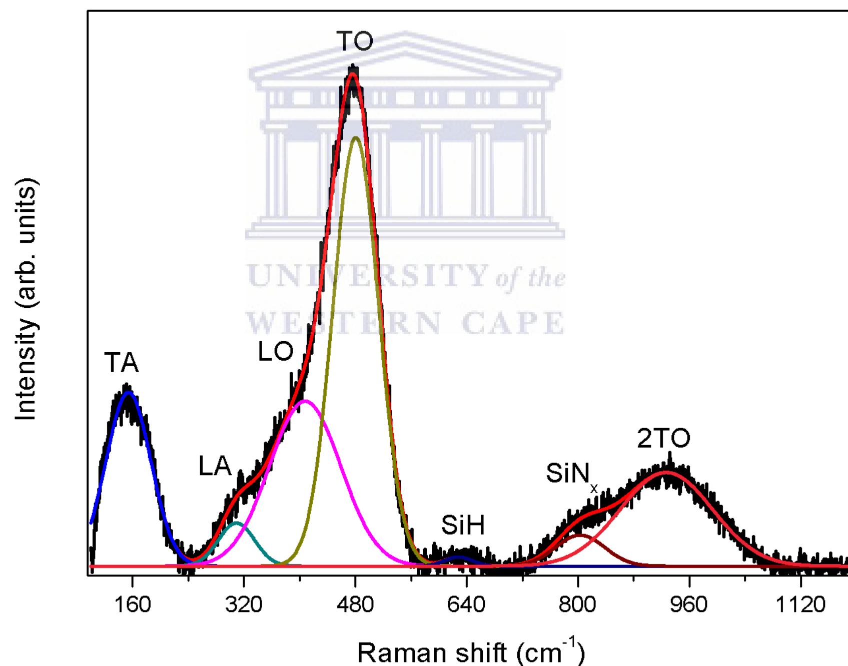

Figure 2.14: Typical Raman spectrum showing all possible peaks [2.19]

2.3.3 Fourier Transform Infrared (FTIR) Spectroscopy

2.3.3.1 Introduction

Infrared (IR) spectroscopy is a non-destructive analytical technique used in the identification of bonding groups in materials. A change in the vibrational status of molecular bonds occurs after a sample has been exposed to IR radiation. This change indicates that some of the radiation has been absorbed, while the remainder has been transmitted. The vibrational frequency of the bonding group dictates the region of absorption in the IR spectra, whereas the amount of absorption detected is dependent on the energy transfer. For IR radiation to be absorbed a change in dipole moment must be experienced by the molecule [2.20].

Two types of IR spectroscopy exist: (i) Dispersive infrared spectroscopy, and (ii) Fourier Transform infrared (FTIR) spectroscopy. The latter will be discussed, as FTIR spectroscopy compared to dispersive IR spectroscopy allows for a faster scan rate, and offers better signal-to-noise ratio [2.20].

UNIVERSITY of the
WESTERN CAPE

2.3.3.2 Theory

FTIR spectroscopy makes use of a Michelson interferometer as a beam splitter. IR radiation is divided in two by the interferometer, and a path difference is created between the two halves of the beam. The two parts are recombined, and the intensity of the recombined beam is monitored as a function of path difference. A schematic of the beam setup is shown below in figure 2.14.

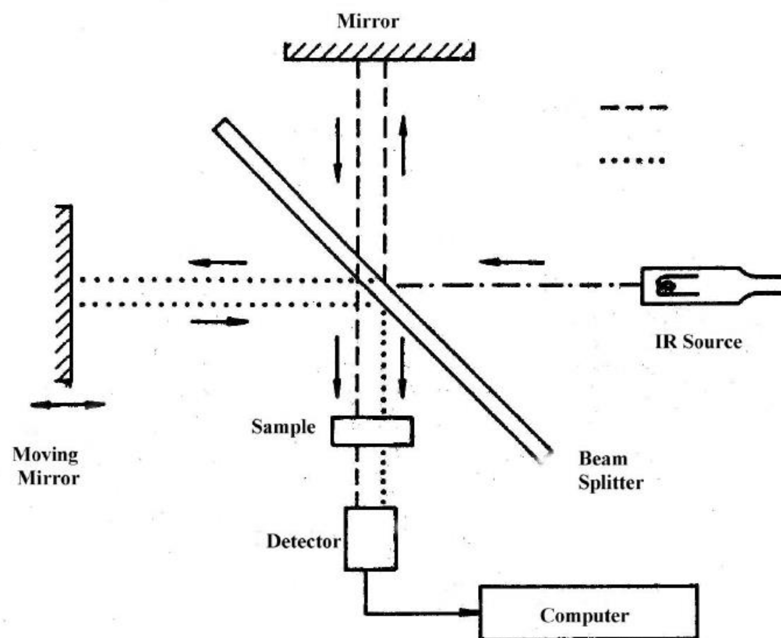

Figure 2.15: Michelson interferometeric process used in a FTIR spectrometer [2.20].

UNIVERSITY of the
WESTERN CAPE

The diagram depicts IR radiation split in two by a semi-transparent mirror acting as the interferometer, allowing 50% of the light to be transmitted while the other 50% is reflected off a stationary mirror. The portion of light that is transmitted is projected onto a movable mirror that is moving at constant speed. The light is reflected off the two mirrors back towards the beam splitter where recombination of the radiation occurs [2.20]. A path difference is created by the moving mirror in relation to the stationary mirror, and interference takes place as the light recombines. The recombined radiation contains information of the entire frequency range emanating from the IR source. The signal is decoded through the use of a computer algorithm executing Fourier transform mathematical operations on the data received. A spectral depiction of the absorbance modes of the sample under analysis is then displayed.

IR Radiation

In FTIR analysis, the preferred unit of measurement is the wavenumber (ω) measured in cm^{-1}, rather than wavelength (λ); the two quantities are related by the following operation

$$\omega = \frac{1}{\lambda}. \quad (2.34)$$

For a single beam, the intensity, B(ω), of the IR radiation given off at the source is related to the amplitude, I(x), as a function of the position, x, of the movable mirror of the interferogram as measured by the detector, by the following mathematical representation [2.21]:

$$I(x) = B(\omega)cos(2\pi\omega x). \quad (2.35)$$

In a polychromic source, as is the case in FTIR systems, the interferogram and the spectrum are related by $I(x) = \int_{-\infty}^{+\infty} B(\omega)\, cos\, 2\pi\omega x\, .\, dv$, showing the variation in the power density as a difference in path-length for the interference pattern [2.21].

Conversely the IR spectra can be related to the interferogram by showing the variation in path-length for the spectrum [2.21]:

$$B(\omega) = \int_{-\infty}^{+\infty} I(x) \cos 2\pi\omega x\, .\, dx. \quad (2.36)$$

The above two equations are used in the algorithm during the decoding of the IR spectrum, known as the Fourier transform pair. These equations relate the interferogram to an IR spectrum by the mathematics contained in a Fourier transform [2.21].

UNIVERSITY of the
WESTERN CAPE

FTIR spectra for thin films are often measured in transmission mode. The transmission data can then be related to the absorption coefficient (α (ω)) by [2.22]:

$$\alpha(\omega) = -\frac{ln[T(\omega)]}{d}, \tag{2.37}$$

where d is the thin film thickness, and ln[T(ω)] is the natural logarithm of the transmission data.

FTIR spectroscopy measurements were conducted at the Chemistry Department at the University of the Western Cape. A Perkin Elmer Spectrum 100 Spectrometer was used to measure in transmission mode on samples deposited on c-Si wafers in an energy range 400-4000 cm^{-1}, and a resolution limit of 4 cm^{-1} for 20 scans. A background reading of a bare c-Si wafer had to be taken to eliminate the absorption effects of the wafer.

UNIVERSITY of the
WESTERN CAPE

Incoherent and multiple reflections occur in both the thin film and the substrate as light is projected onto the surface. These effects were accounted for with a procedure developed by Brodsky *et al.* [2.22]. A correction to the overestimate calculated for the absorption coefficient can be rectified by relating α_{BCC} to the as-measured Transmission, T(ω) [2.22]:

$$T(\omega) = \frac{4T_0^2 e^{-\alpha_{BCC}d}}{(1+T_0)^2-(1-T_0)^2 e^{-2\alpha d}}, \tag{2.38}$$

where d is the thickness of the thin film in cm, and $T_0 = 0.54$ for c-Si, which is the baseline transmission when α(ω) = 0.

The effects of coherent light interaction and differences in refractive indices are then taken into account by following the Maley approach [2.23]:

$$\alpha_{TRUE} = \frac{\alpha_{BCC}}{1.72-12\omega d} \; ; \; \omega d \leq 0.06 \tag{2.39}$$

and

$$\alpha_{TRUE} = \alpha_{BCC}; \; \omega d \geq 0.06. \tag{2.40}$$

a-SiN:H vibrational modes

For hydrogenated amorphous silicon nitride three groups of bonding configurations can be observed over the energy range 400-3500 cm^{-1} [2.24, 2.25]. The chamber design and deposition conditions under which the a-SiN_x:H thin films are deposited strongly dictates the bonding arrangements and bond densities that are measured. The bonding configurations are as follows:

i. SiH_n bonds located between 630-650 cm^{-1} and 2000-2300 cm^{-1} for the bending or wagging modes as well as stretching modes respectively,

ii. NH_n modes located at 1150 cm^{-1} and 1540 cm^{-1} for the bending modes of NH and NH_2 respectively, and at 3340 cm^{-1} and 3450 cm^{-1} for the stretching modes of the same bonds,

iii. SiN stretching bonds have vibrational modes at a frequency of 750-1050 cm^{-1}. The most visible of these occur at 490 cm^{-1} and at 850 cm^{-1} due to the symmetric and asymmetric stretching modes of NSi_3. The stretching mode of SiN_n and H-Si-N_3 modes can be observed at 790 cm^{-1}, and 1020 cm^{-1} respectively.

The SiNH and SiH_n mode centred about 2000-2220 cm^{-1} can statistically be decomposed into as many as six Gaussian peaks, each with their own bonding configuration and contribution as shown in table 2.3 below [2.26].

UNIVERSITY of the
WESTERN CAPE

Table 2.1: Bonding Configurations and corresponding wavenumbers.

Wavenumber (cm-1)	2005	2065	2100	2140	2175	2220
Bonding arrangement	H-Si-Si_3	H_2-Si-Si_2	H-Si-NSi_2	H-Si-N_2Si and H_2-Si-NSi	H_2-Si-N_2	H-Si-N_3

Figure 2.15 below depicts the vibrations experienced by SiN_x bonds when excited by IR radiation.

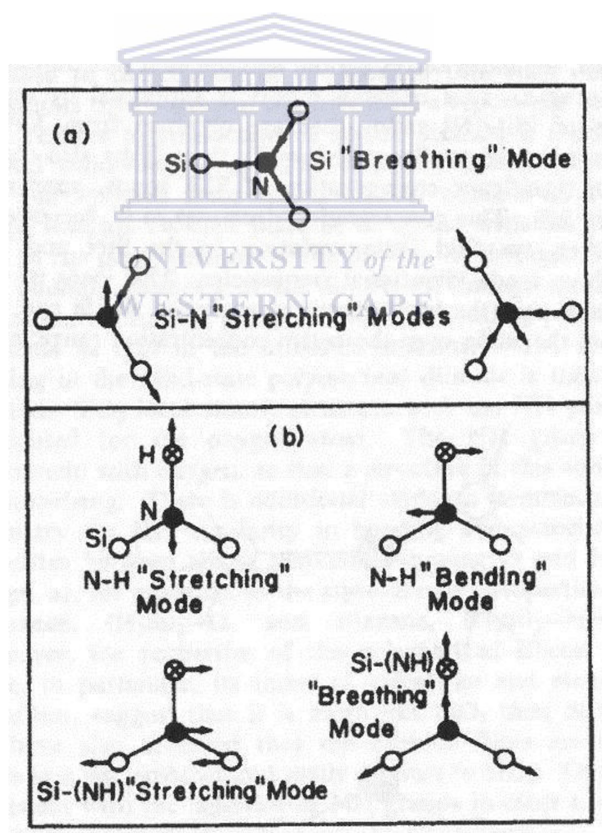

Figure 2.16: IR active vibrations involving Si, N, and H (a) Si breathing along with Si-N stretching modes, (b) N-H bending and stretching vibrations, and Si-(NH) breathing and stretching modes [2.27].

Figure 2.17 depicts a typical baseline flattened spectra of a-SiN_x:H for an as-deposited sample belonging to MW 303, one of the two sets of samples. The spectra has to be flattened in order to apply the corrections procedure,

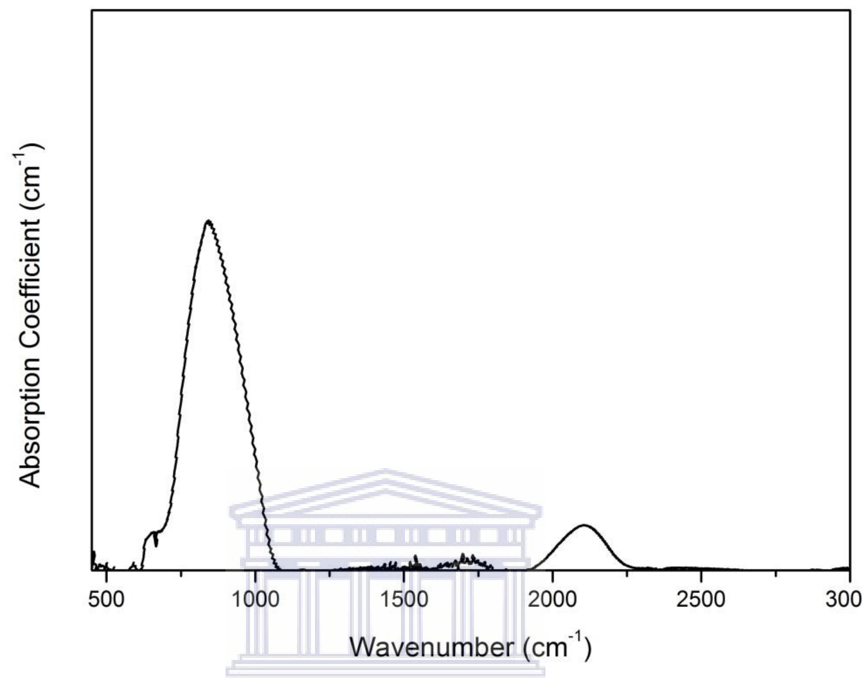

Figure 2.17: Typical flattened FTIR spectrum of SiN_x.

UNIVERSITY of the
WESTERN CAPE

Due to overlapping of absorption bands within the structure, a decomposition process has to be conducted as shown below. The deconvolution of the underlying modes allows one to quantify the amount of the specific bonding configuration present in the sample. Figure 2.18 shown below depicts the hydrogen containing mode of SiN_x:H, allowing us to quantify the bonded hydrogen in the thin film.

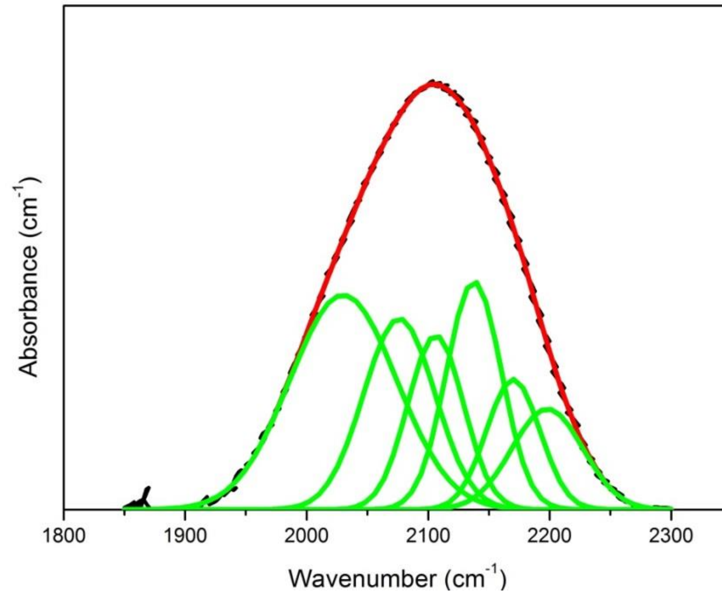

Figure 2.18: Decomposition of peaks centered between 2000-2250 cm^{-1} showing the six possible bonding configurations which may occure at the specific wavenumber.

UNIVERSITY of the
WESTERN CAPE

2.3.4 Elastic Recoil Detection Analysis (ERDA)

2.3.4.1 Introduction

Elastic recoil detection analysis (ERDA) is an analytical technique used for light elemental analysis and depth profiling that makes use of a high energy (MeV) ion beam ($^4He^+$). In ERDA, the recoiled atoms of the thin film target under analysis are detected when bombarded with the high energy heavy ions as they are scattered in a forward direction. ERDA works on the same operating principles of Rutherford Backscatter Spectroscopy (RBS), except in the case of RBS it is the backscattered atoms of the ion beam that are detected. ERDA is chosen over RBS due to the fact that RBS has a poorer sensitivity to light elements suspended in solid matrix [2.28]. This makes ERDA a useful technique for the determination of a concentration gradient of light elements in a sample. ERDA was first introduced

in the mid 1970's by J. L'Ecuyer *et al.* [2.28], when they determined the deuterium concentration and depth distribution in a heavy matrix. It has since become the foremost technique in the determination of depth profiles of light elements.

2.3.4.2 Theory

Ion based techniques make use of high energy bombardment of a thin film sample. During this bombardment, the light atoms making up the thin film are ejected from the target and are scattered in the forward direction [2.29], as depicted schematically in figure 2.19 below. It shows the projectile particle of mass M_1 with energy E_0 colliding with a stationary and less massive target particle M_2 given energy E_2.

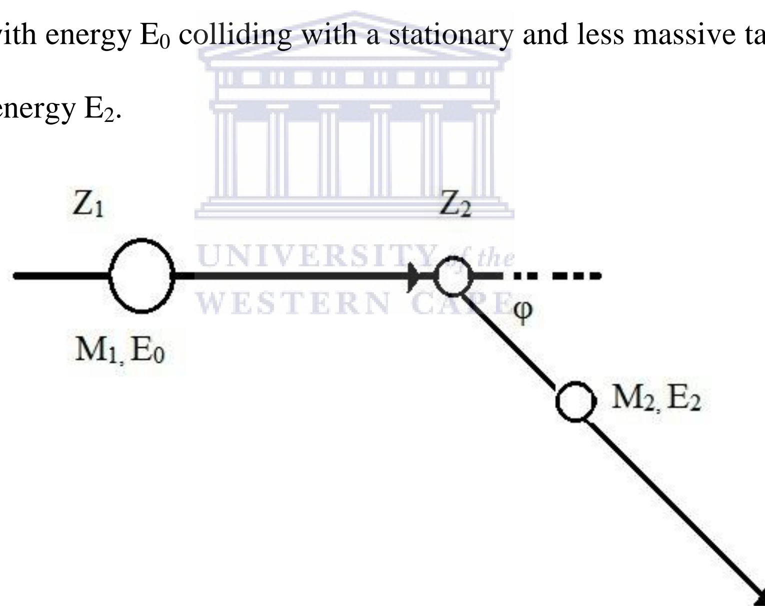

Figure 2.19: Schematic of ERDA process.

Energy is elastically transferred from the projectile to the target, ejecting the target particle and allowing it to scatter in a forward direction. The nuclear interaction of the two atoms can be described using Coulomb repulsion and attraction forces, while the energy transfer can be calculated by considering the

conservation of energy and momentum and by the determination of the kinematic factor for recoiling [2.29]:

$$K_r = \frac{4M_1M_2}{(M_1 + M_2)^2} cos^2\varphi, \tag{2.41}$$

where M_1 and M_2 are the masses of the projectile and the target atoms respectively, and φ is the recoil angle. The projectile particle does not give up all the energy when scattered at an angle ϑ, and the remaining fraction K_s is defined as [2.29]:

$$K_s = \left(\frac{(M^2{}_2 - M^2{}_1 \sin^2\vartheta)^{\frac{1}{2}} + M_1 \cos\vartheta}{M_1 + M_2}\right)^2. \tag{2.42}$$

By comparing equations (2.41) and (2.42) it can be noted that K_s and K_r depend on the ratio of M_2/M_1 as well as the scattering and recoil angles respectively [2.29].

The constituents of the thin film target can be identified through elastic collisions. The number of atoms per unit area on the target, N_s, is related to Q_D, the total number of particles detected, by [2.30]:

$$Q_D = \sigma(\varphi).\Omega.N_s.Q. \tag{2.43}$$

Q is the total number of projectile particles impinged onto the target; this is calculated by the time integration of the current of the impinging ion beam, Ω is the solid angle with the detector, and σ(φ) is defined as the differential cross section and has units of area, which can further be expressed as [2.30]:

$$\sigma(\varphi) = \frac{1}{\Omega}\int_{\Omega} \frac{d\sigma}{d\Omega}.d\Omega. \tag{2.44}$$

The probability of the ion beam ejecting a recoil atom from the target is defined by the Rutherford differential cross section and is expressed as [2.29]:

$$\frac{d\sigma}{d\Omega} = \left(\frac{Z_1Z_2e^2}{2E_0}\right)^2 \frac{(1+\frac{M_1}{M_2})^2}{cos^3\varphi}, \tag{2.45}$$

where Z_1 and Z_2 are the atomic numbers of the projectile particle and the target particle respectively. For hydrogen depth profiling determined by the forward recoiling of atoms from the target a Mylar ($C_{10}H_8O_4$) absorber is required. The role of the Mylar is to stop the scattered ion beam particles from reaching the detector, while the hydrogen atoms ejected from the target may pass through [2.30].

2.3.4.3 Experimental Setup

ERDA was conducted using the Van de Graaff accelerator situated at iThemba labs, Faure. A $^4He^+$ ion beam with energy of 3 MeV and an average current of 20 nA was employed to determine the hydrogen content of the thin films deposited on the c-Si substrate. An incident angle of 15° was formed between the beam and the samples, with the samples at 75° with respect to the beam. A 23 µm Mylar absorber was placed in front of the surface barrier detector placed at a 30° angle. The system was calibrated for hydrogen detection using a 125 µm polyimide Kapton ($C_{22}H_{10}N_2O_5$) as the reference material. A configuration of the setup is shown in figure 2.19 below. The spectra obtained were analysed using SIMNRA Software [2.31] and the hydrogen depth profiles and concentrations calculated from the fitting results.

UNIVERSITY of the
WESTERN CAPE

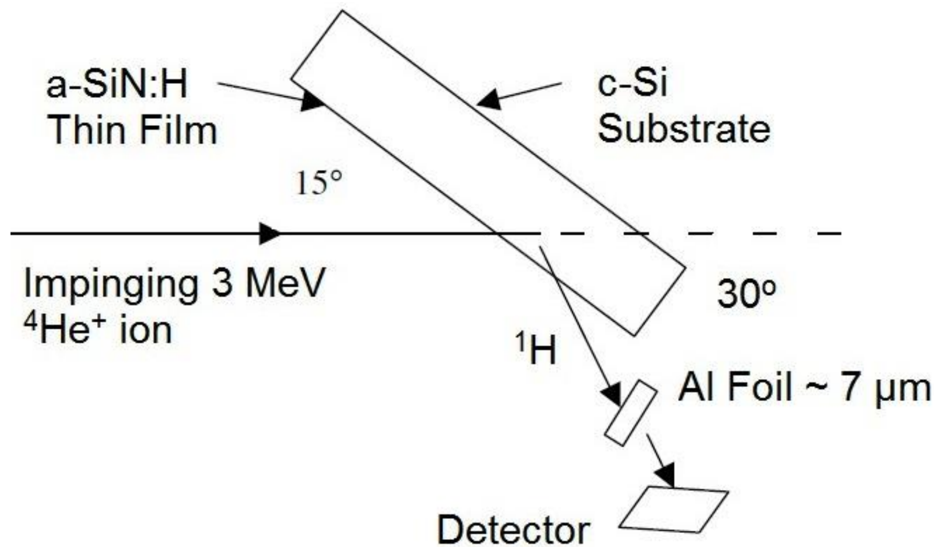

Figure 2.20: Schematic setup of ERDA showing the angle of incidence and recoil angle.

UNIVERSITY of the
WESTERN CAPE

2.3.5 Atomic Force Microscopy (AFM)

2.3.5.1 Introduction

Atomic Force Microscopy (AFM) is a surface characterisation technique, used in the determination of topological and morphological structures which may exist on the surface of the sample. AFM is able to measure on an atomic scale, by employing a sharp tip suspended on a cantilever [2.32]. AFM functions in a similar manner to that of the earlier discovered surface technique of Scanning Tunnelling Microscopy (STM). AFM was developed in 1986 by Gerd Binning *et al*. [2.32] in an effort to characterise non-conducting samples with atomic resolution in a similar method to STM [2.33].

2.3.5.2 Theory

The AFM tip interacts with the non-conducting surface of the sample through inter-atomic interactions [2.30]. The strength of the attraction and repulsion forces

are related to the distance between the tip of the probe and the surface. The dominant interaction under which the AFM operates is that of the long-range van der Waals forces, which are not only exponentially dependent on the distance but also on the shape of the probe [2.30], as shown in the force curve below.

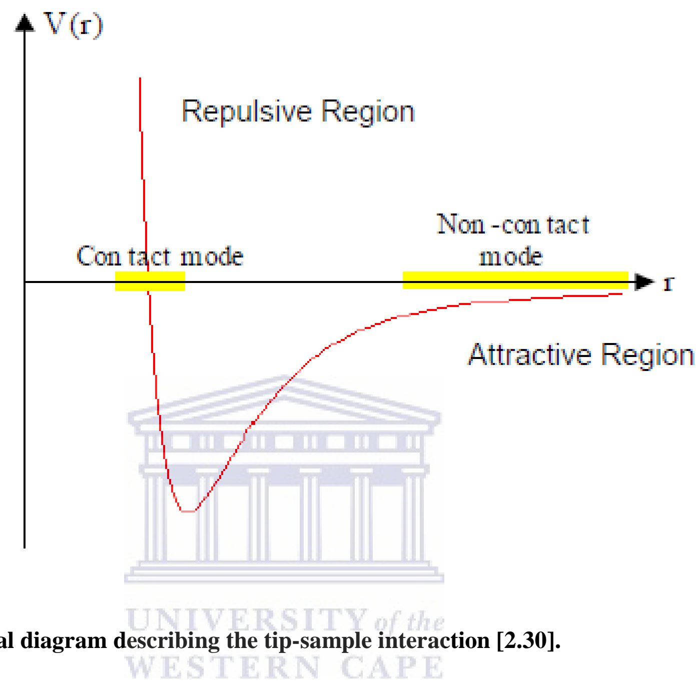

UNIVERSITY of the
WESTERN CAPE

Figure 2.21: Potential diagram describing the tip-sample interaction [2.30].

In surface probe microscopy the scanning probe is suspended on the end of a sensitive scanner capable of sub-nanometre movement. The cantilever is made of piezoelectric ceramic material which bends in response to a change in force due to surface changes on the sample. The cantilever obeys Hooke's Law for small displacements; this is precisely monitored and the rate of bending is determined by an optical detector. A schematic of the AFM cantilever setup is shown in figure 2.21 below [2.30].

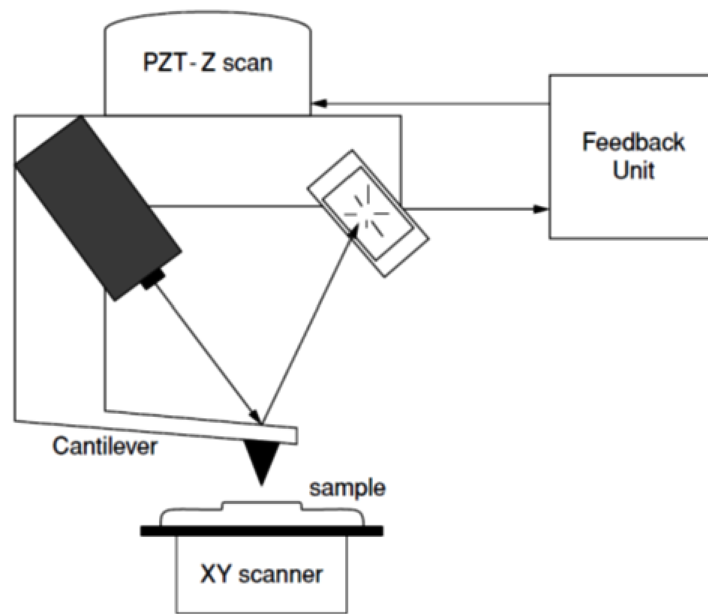

Figure 2.22: AFM Schematic setup [2.30].

UNIVERSITY of the
WESTERN CAPE

Two modes of operation exist for AFM measurement: *constant-height* and *constant-force* modes. In *constant-force* mode, accurate topographical images are acquired. The piezoelectric device senses a change in surface characteristics and responds accordingly to maintain a pre-set value for the force. This is done by either moving the sample or the tip. During *constant-height* or *deflection* measurements, the cantilever is set to a constant height, and a change in the value is detected during surface scans. This mode is often used when imaging atomically flat samples at high resolutions [2.30].

There are three methods of scanning the sample with AFM: *tapping, contact,* and *non-contact modes*, with *tapping mode* being the most commonly used of the three. The tip is dragged across the surface, and the tip and sample experiences a mutually repulsive force. When *non-contact mode* is employed, the tip is made to oscillate at a fixed distance above the surface of the sample, and the sample and tip is no longer in the repulsive region. A vacuum setup is needed for operation in

non-contact mode, as a precipitation from the ambient air forms on the sample giving rise to false images [2.30]. In *tapping mode* the tip is set at an intermediate distance above the sample, and is made to oscillate at a constant frequency as the cantilever scans across the sample. Minimal damage is done to the tip as no contact is made between the probe and the sample. The resulting image that is displayed is a result of the change in force due to a change in surface topology.

The resolution of an AFM image is related to the size and shape of the probe used to scan over the sample. For good resolution the probe has to be of a comparable size to the surface features on the sample under analysis, this minimize the tips interaction with surrounding features [2.34]. Blunt tips will not accurately scan over the surface, and objects may appear larger.

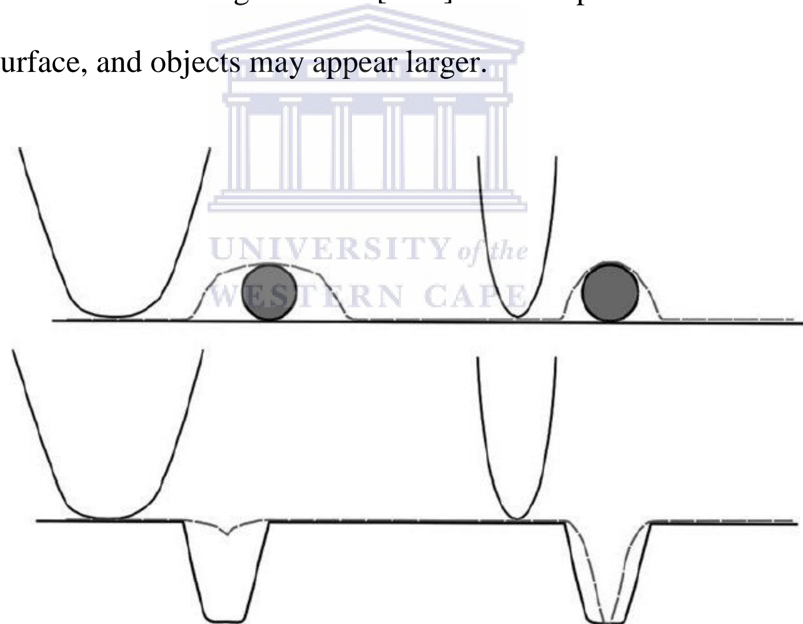

Figure 2.23: Image resolution and tip size [2.34].

Roughness variations of the surface of the sample depict a variation in surface features along the length of the sample. The most common roughness values which are quoted are the arithmetic roughness, R_a, and the root mean square roughness, R_q or R_{rms} [2.34]. Elevated values in both cases indicates an increase in roughness. A summary of the roughness parameters are shown in table 2.4 below,

UNIVERSITY of the
WESTERN CAPE

as well as the mathematical formulae for calculating the respective roughness values.

Table 2.4: Roughness parameters and Mathematical representation [2.34, 2.35]

Parameter name	Abbreviation	Mathematical Representation
Average Roughness	R_a	$R_a = \frac{1}{n}\sum_{i=1}^{n}\lvert y_i\rvert$
Root-Mean-Squared Roughness	R_q or R_{rms}	$R_q = \sqrt{\frac{1}{n}\sum_{i=1}^{n} {y_i}^2}$
Maximum Height of the Image	R_t	$R_t = \left\lvert \min_{1\le i\le n} y_i \right\rvert + \left\lvert \max_{1\le i\le n} y_i \right\rvert$
Skewness	R_{sk}	$R_{sk} = \frac{1}{n{R_q}^3}\sum_{i=1}^{n} {y_i}^3$
Kurtosis (The measure of the distribution of spikes above and below the mean line.)	R_{ku}	$R_{ku} = \frac{1}{n{R_q}^4}\sum_{i=1}^{n} {y_i}^4$

UNIVERSITY of the
WESTERN CAPE

2.3.5.3 Experimental Setup

AFM experiments were conducted at the Materials Research Department (MRD) at iThemba Labs, Faure, on a Nanoman V machine equipped with a VT-103-3K-2 acoustic hood. The AFM was operated using tapping mode with a scan angle of 45° and a scan rate of 0.896 Hz, scanning an area of 3 µm by 3 µm with a resolution of between 10nm and 100nm. The setup allowed for the accurate topological representation of the surface of the thin films. A photograph of the

AFM setup with the hood up can be seen below. The hood was dropped during measurements, while the AFM rested on a vibration free table, mitigating all external movements to allow for a more accurate and clearer scan.

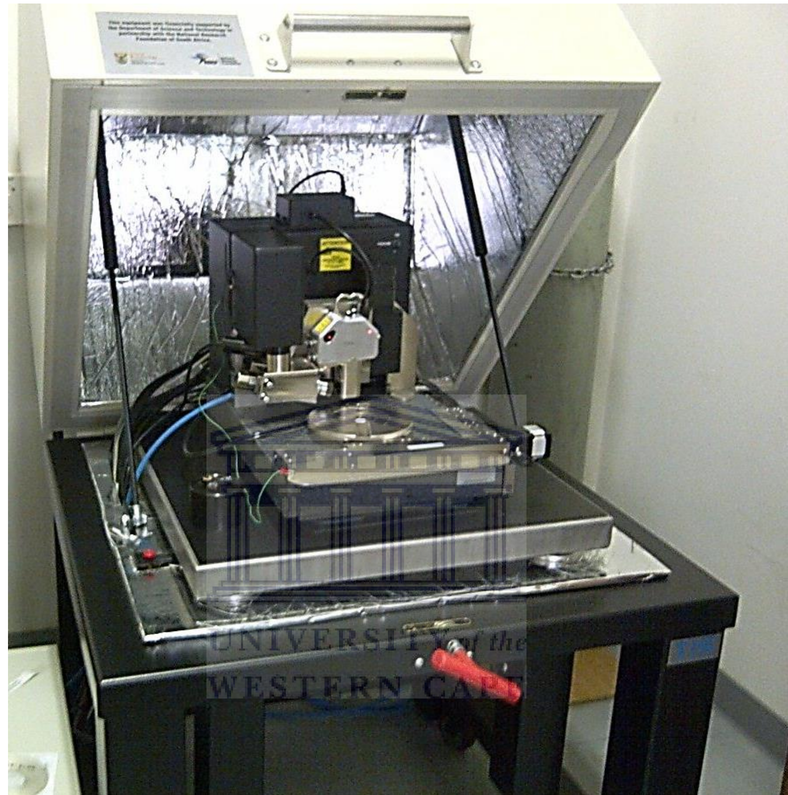
UNIVERSITY of the
WESTERN CAPE

Figure 2.24: AFM setup on a vibration free table.

2.3.6 High Resolution Scanning Electron Microscopy (HRSEM)

2.3.6.1 Introduction

High resolution scanning electron microscopy (HRSEM) was used for surface analysis of the sample, and is an excellent complementary technique to AFM. In

HRSEM electrons (primary electrons) are accelerated towards the specimen and are scanned across the surface of the sample [2.36]. As the primary electrons interact with the surface, secondary processes occur from which internal and topographical structures are determined.

2.3.6.2 Theory

The resolution of any microscopy device is limited by the wavelength of the illumination source [2.36]. Abbe's Equation shows that the resolution (d) of a device is proportional to the ratio of a constant multiplied by the wavelength of the illumination source, and divided by the sine of the aperture angle [2.36]:

$$d = \frac{0.612\lambda}{n sin\alpha}, \qquad (2.46)$$

where d is the resolution of the device, which should be a minimum; λ is the wavelength of the illumination source (electrons in the case of HRSEM), and α is the angle formed between the primary beam and the aperture.

UNIVERSITY of the
WESTERN CAPE

High resolution (HR) images are produced through the use of a focussed electron beam striking the surface of the sample. The electrons are liberated from an electron gun and accelerated towards an anode, acquiring energy as it moves along the vacuum column. The single energy electrons are focused by a series of electromagnetic lenses before striking the surface of the sample, forming an image of the topographical or internal structure under investigation [2.36].

The electron gun is located at the top of the vacuum column, and is comprised of the filament which is the source of the electrons, and is negatively charged, a Wehnelt cylinder (gridcap) and an anode plate. The type of filament used in a SEM is dependent on the purpose and resolution delivered by the microscope.

Thermionic electrons are formed when a tungsten or lanthanum hexaboride (LaB_6) filament are heated. Electrons with a wide spread of energies are boiled off during thermionic emission; this spread of energy is not ideal and is crudely focussed through the creation of an electrostatic bias formed on the slightly more negative gridcap. The electrons are accelerated towards the anode due to a difference in potential known as the accelerating voltage, where the electrons gain energy equal to the accelerating voltage. The number of electrons released by the filament increases as the filament is heated. This number reaches saturation, where after the amount of electrons given off does not increase for a further energy input. The life span of the filament is dependent on several factors which include, but are not only limited to, how well the vacuum system is maintained as well as the heating of the filament wire and the cleanliness of the gun [2.36].

UNIVERSITY of the
WESTERN CAPE

Major depreciation of the wire occurs with gross over-heating above saturation as ion bombardment and evaporation of the metal filament occurs over time.

The crudely focussed electron beam is further focussed by a series of electromagnetic lenses. These lenses consist of iron poles with wire coiled around them, producing a magnetic field. The strength of the magnetic field is dependent on the current flowing through the wire. The condenser lens is the first in the series of lenses, and is responsible for the convergence of the electron beam to a point. Changing the current in the convergence lens moves the focal point up and down the column, and a setting should be chosen such that the focal point lies above the condenser aperture. The intensity of the beam striking the sample can be controlled through a combination of condenser lens current and accelerating voltage.

Below the aperture, the electron beam diverges and a final lens brings the beam back into focus above the sample, and demagnification occurs. The beam spot size on the sample determines the resolution limits. A combination of aperture size and demagnification determines the spot size. A schematic of a SEM set-up is shown in figure 2.25 below.

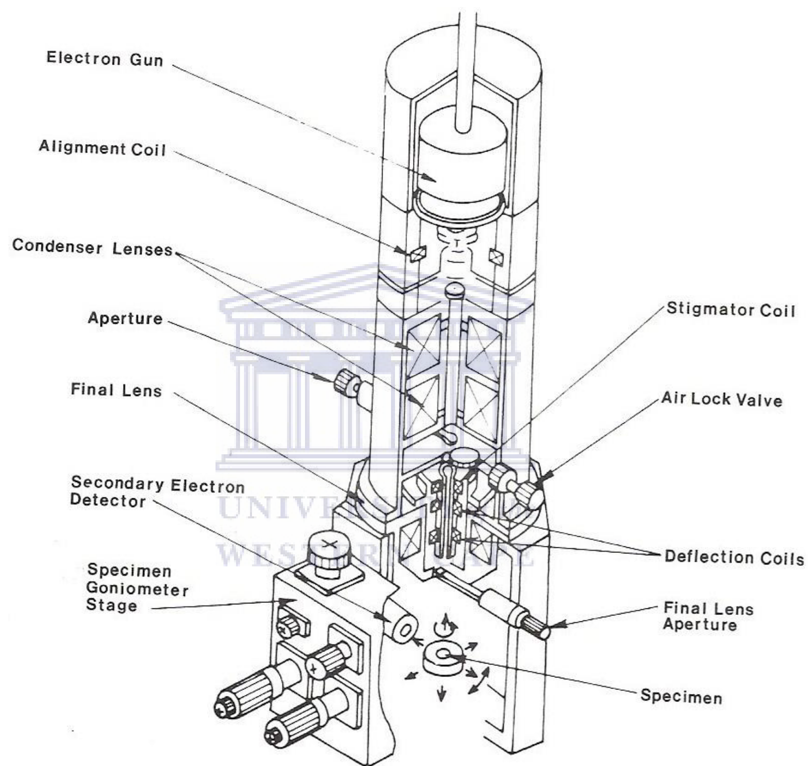

Figure 2.25: Schematic of SEM [2.36].

The interaction of the primary beam with the surface of the specimen leads to the production of many signals as can be seen in figure 2.26.

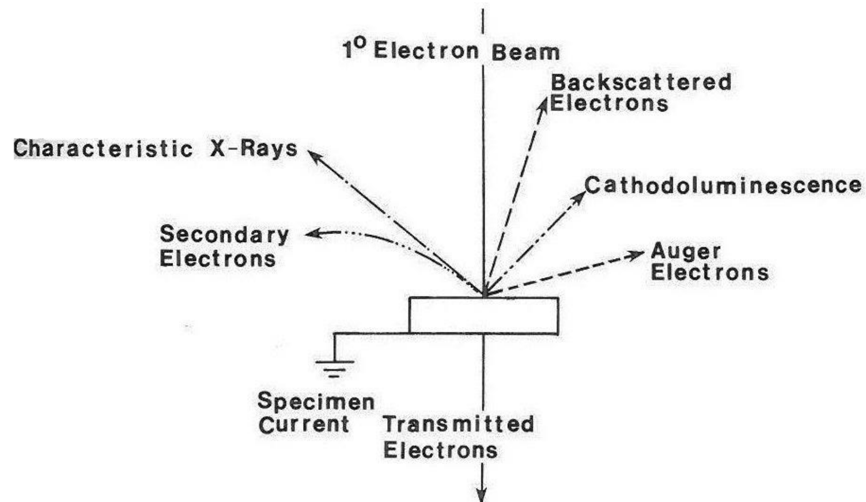

Figure 2.26: Interaction of the primary beam with the specimen [2.36].

These signals can be used for the determination of composition, surface analysis, and internal structure. The information gathered from the specimen is dependent on the interaction which takes place and the signal that it produces. Upon striking the surface, the interaction of the primary beam may either be elastic or inelastic collision, the beam may be transmitted through the specimen, or partake in a recombination event. The interaction that occurs between the sample surface and the primary beam dictates the signal which is registered. A summary of interaction and the uses thereof is given in the table below [2.36].

UNIVERSITY of the
WESTERN CAPE

Table 2.5: A summary of beam interaction and signal events [2.36].

Event	Between	Signal	Resolution	Use
Elastic	Beam electrons/ Specimen nuclei or electrons	Backscattered electrons	> 1 µm 1,000 nm	Atomic number and topographical contrast
Inelastic Scattering	Beam or Backscatter electrons/ specimen electrons	Secondary electrons	10 nm or better	Surface structure
		Continuum X-rays		Not a useful signal
Recombination	Free electrons generated/ positive holes	Cathodeluminescence	<80 nm	Impurity concentration
		Characteristic X-rays	Measured in eV's, an integral of peak width of a given line	Elemental composition
		Auger electrons	Measured in eV's, an integral of peak width of a given line	Surface composition
Transmission	Electrons through the specimen	Transmitted electrons	5 nm or better	Internal ultrastructure
Energy Transfer	Specimen/ ground	Specimen current	Poorer than 2° electron image	Atomic number contrast

UNIVERSITY of the WESTERN CAPE

Tungsten and lanthanum hexaboride tips are not the only types used in scanning electron microscopy. Field emission guns (FEG's) consist of metal crystals which are orientated accordingly. In FEG's electrons are draw from the fine tip by an electric field rather than through a thermionic process as in the standard gun setup [2.36]. It is possible to obtain an intensity of up to 1000 times brighter with a FEG setup compared to that of a standard thermionic gun for a similar electron spot size [2.37]. The tip used in a FEG are designed from tungsten, making use of the metallic properties that the metal possesses, such as high melting point, low vapour pressure and mechanical strength. The finely pointed tip produces a final spot size of around 50 Å, which increases the resolving power of the microscope as well as producing a far more acclamatory signal-to-noise ratio [2.36].

UNIVERSITY of the
WESTERN CAPE

Table 2.6: Comparison of SEM tips [2.36].

	Tungsten Filament	**Lanthanum Hexaboride**	**Field Emission**
Type of Emission	Thermionic	Thermionic	Field
Operating Vacuum (torr)	10^{-4} - 10^{-5}	10^{-6} - 10^{-7}	10^{-9} - 10^{-10}
Brightness ($A/cm^2 \cdot ster$)	10^{-4} - 10^{-5}	$10^5 – 10^6$	$10^7 – 10^9$
Source Size (Å)	1×10^6	2×10^5	$< 1 \times 10^2$
Energy Spread (eV)	1 - 5	0.5 - 3	0.2 – 0.3
Probe Current Stability (% per minute)	0.1 – 1.0	0.2 – 2.0	2 - 10
Operating Life (Hours)	> 20	> 100	> 300

UNIVERSITY of the
WESTERN CAPE

2.3.6.3 Experimental Setup

HRSEM was performed at the Electron Microscope Unit (EMU), of the University of the Western Cape, using an Auriga Zeiss instrument with Gemini technology, employing a FEG Tip operated at an accelerating voltage of 3 kV. The working distance and magnification was altered according to the contrast and depth of field required.

2.3.7 UV-Vis Spectroscopy

2.3.7.1 Introduction

SiN_x:H thin films are used as an anti-reflective coating on top of a-Si:H solar cells [2.38]. For this reason it is incumbent to determine and understand the response of the material to an electromagnetic (EM) stimulus, and from the response the optical constants, such as the refractive index (n) and the extinction coefficient (k), and the optical band gap (E_g) may be determined.

In this section the interaction of light by transmission as well as reflection through and off the sample will be discussed with the appropriate theory to describe the interaction of radiation through matter.

2.3.7.2 Theory of the Interaction of Light with Matter

UNIVERSITY of the
WESTERN CAPE

Some solids are transparent, while others are opaque. Some types of solids will absorb the impinging radiation while other types of solids strongly reflect the radiation. The response of the material to the radiation is frequency dependant. The entire electromagnetic spectrum can be described by the application of Maxwell's Equations which are represented as below, and is summarised from reference [2.39]:

$$\begin{aligned} \nabla \times \boldsymbol{H} &= \frac{\epsilon}{c}\frac{\partial \boldsymbol{E}}{\partial t} + \frac{4\pi\sigma}{c}\boldsymbol{E}, \\ \nabla \cdot \boldsymbol{E} &= 0, \\ \nabla \times \boldsymbol{E} &= -\frac{\mu}{c}\frac{\partial \boldsymbol{H}}{\partial t}, \\ \nabla \cdot \boldsymbol{H} &= 0, \end{aligned} \qquad (2.47)$$

The equations were written by assuming no magnetic effect, i.e. $\mu = 1$, and **H** is the magnetic field, **E** is the electric field, ε is the product of ε_0 the permittivity of free space and ε_r the relative permittivity. The quantity μ is the magnetic permittivity, while c is the speed of light in a vacuum. The propagation of light through a medium compared to that through a vacuum is related by the dielectric constant ε and the conductivity σ for the specific medium. The dielectric constant describes the magnitude of displacement currents due to the time variation of the electric field. The real current created by the interactions of the electric field is described by the conductivity. The magnetic field may be eliminated from these equations such that:

$$\nabla^2 \times \boldsymbol{E} = \frac{\epsilon}{c^2}\frac{\partial^2 E}{\partial t^2} + \frac{4\pi\sigma}{c^2}\frac{\partial E}{\partial t}. \quad (2.48)$$

UNIVERSITY of the
WESTERN CAPE

This represents a wave propagated with dissipation, by choosing a frequency (ν) and writing

$$\boldsymbol{E} = \boldsymbol{E_0} \exp\{i(\mathbf{K} \cdot r - \nu t)\}. \quad (2.49)$$

Then the wave equation requires that

$$-\mathbf{K^2} = -\epsilon\frac{\nu^2}{c^2} - \frac{4\pi\nu\sigma i}{c^2}, \text{ with} \quad (2.50)$$

$$K = \frac{\nu}{c}\left(\epsilon + \frac{4\pi\sigma i}{\nu}\right)^{\frac{1}{2}}, \quad (2.51)$$

where K is the complex propagation constant. For light travelling in free space K can be written as

$$K = \frac{\nu}{c}. \quad (2.52)$$

The velocity of light travelling through a medium is modified, and the phase velocity is divided by a complex refractive index

$$N = \left(\epsilon + \frac{4\pi\sigma i}{\nu}\right)^{\frac{1}{2}}. \quad (2.53)$$

The macroscopic optical properties can be described in terms of N for light of frequency ν, propagating as a plane wave in the z-direction

$$N = n + ik. \tag{2.54}$$

Equation (2.54) above describes both the imaginary (k) and real parts (n) of N, and the propagation constant can be written as

$$K = \frac{n\nu}{c} + \frac{ik\nu}{c}, \tag{2.55}$$

such that the wave equation can be re-written in the form

$$\boldsymbol{E} = \boldsymbol{E_0} \, exp\left\{i\nu\left(\frac{nz}{c} - t\right)\right\} exp(-\frac{k\nu z}{c}). \tag{2.56}$$

The velocity of the light in a medium is reduced to c/n, and the wave is damped by a factor exp (-2πk/n) as it progresses through the medium.

The *damping* effect experienced by the impinging wave is ascribed to the absorption of EM energy by the medium. To calculate the energy loss, Maxwell's Equations are used to determine the current density (J) of the damped wave; the right hand side of the first equation can be written as

UNIVERSITY of the
WESTERN CAPE

$$\boldsymbol{J} = \left(-\frac{i\varepsilon\nu}{c} + \frac{4\pi\sigma}{c}\right)\boldsymbol{E} = -\frac{i\nu}{c}\mathbf{N}^2\boldsymbol{E}. \tag{2.57}$$

The rate at which Joule heat is produced can be described by the real part such that

$$\boldsymbol{J} \cdot \boldsymbol{E} = -\frac{i\nu}{c}\boldsymbol{N}^2\boldsymbol{E}. \tag{2.58}$$

The fraction of energy absorbed while passing through the medium is described by the *absorption coefficient* and can be given by

$$\eta = \frac{Re(\boldsymbol{J} \cdot \boldsymbol{E})}{|\boldsymbol{E}^2|} = \frac{2nk\nu}{c}. \tag{2.59}$$

For the remainder of the thesis the absorption coefficient will be represented with the use of the symbol α. Considering only the case of normal incidence, it has a

solution to Maxwell's Equations of the damped wave travelling through a medium, with a solution that matches a reflected wave outside the medium, for z > 0

$$E_x = E_0 \exp\left\{i\nu\left(\frac{Nz}{c-t}\right)\right\}, \tag{2.60}$$

while for z < 0, outside of the medium in free space the electric field can be written as

$$E_x = E_1 \exp\left\{i\nu\left(\frac{z}{c-t}\right)\right\} + E_2 \exp\left\{-i\nu\left(\frac{z}{c+t}\right)\right\}, \tag{2.61}$$

where E_1 and E_2 are wave amplitudes corresponding to waves travelling to the right and left respectively. The summation of these two amplitudes at the boundary is given by

$$E_0 = E_1 + E_2. \tag{2.62}$$

Magnetic fields are associated with the impinging waves; these waves have magnetic vectors in the y-direction. The application of Maxwell's equations to calculate H_y gives rise to

$$\mathrm{N}E_0 = E_2 - E_1, \tag{2.63}$$

when matched to the wave on the outside of the medium. The ratio of the complex amplitudes of the reflected and incident waves is given by:

$$\frac{E_2}{E_1} = \frac{1-\mathrm{N}}{1+\mathrm{N}}. \tag{2.64}$$

This corresponds to a real reflection coefficient:

$$R = \left|\frac{1-\mathrm{N}}{1+\mathrm{N}}\right|^2 = \frac{(\mathrm{n}-1)^2+\mathrm{k}^2}{(\mathrm{n}+1)^2+\mathrm{k}^2} \tag{2.65}$$

in terms of the real and imaginary parts of the complex refractive index N.

The values of the optical constants, n and k, for the medium in which the light is propagating through can be fixed from independent measurements of the

UNIVERSITY of the
WESTERN CAPE

reflection and absorption coefficients. The experiment being conducted may be more complicated, such that the reflection or transmission of the light may not be perpendicular to the surface at the boundary of the thin film. The results of such experiments may still be described through the use of the same two coefficients, regardless of the complexities.

The values of n and k are related by the dispersion relation, and cannot be thought of as two separate and independent quantities. The quantity N^2 is an example of a generalised susceptibility (x) which can be linked as follows [2.39]:

$$D = xE, \tag{2.66}$$

where D and E is described as the “displacement” and “force” respectively. When a linear relation as the one shown by Equation 2.66 above is expressed as a function of frequency or time, certain requirements of causality needs to be fulfilled. No displacement may take place until after an application of force. The conditions require both the real and imaginary parts of a complex function such as [2.39]:

UNIVERSITY of the
WESTERN CAPE

$$x(\nu) = x_1(\nu) + ix_2(\nu), \tag{2.67}$$

which should satisfy the Kramer-Kronig relations

$$x_1(\nu) = \frac{2}{\pi}\int_0^{\infty}\frac{\nu' x_2(\nu')\,d\nu'}{\nu'^2 - \nu^2} + Const \tag{2.68}$$

and

$$x_2(\nu) = -\frac{2\nu}{\pi}\int_0^{\infty}\frac{x_1(\nu')\,d\nu'}{\nu'^2 - \nu^2}. \tag{2.69}$$

In the case of the optical properties of a material, the real and imaginary parts of N^2 are given as

$$N^2 = (n^2 - k^2) + 2nki \tag{2.70}$$

such that the following arise [3.39]

$$n^2(\nu) - k^2(\nu) = \frac{2}{\pi}\int_0^\infty \frac{\nu' 2n(\nu')k(\nu')\, d\nu'}{\nu'^2 - \nu^2} + Const \quad (2.71)$$

and
$$2n(\nu)k(\nu) = -\frac{2\omega}{\pi}\int_0^\infty \frac{\{n^2(\nu) - k^2(\nu)\}d\nu'}{\nu'^2 - \nu^2}. \quad (2.72)$$

In each integral, the principal part is taken. If the absorption coefficient is known as a function of frequency for all frequencies, it would be possible to evaluate both n and k separately as functions of frequency.

Optical modelling and the extraction of functions

The optical parameters of a material are important to study for any material used in optoelectronic devices. The optical parameters are determined indirectly by the response of the material to an electromagnetic stimulus, which informs us about the underlying properties contained within the bonding network making up the material. Computational methods for the extraction of the optical parameters from UV-visible spectroscopy measured either in transmission or reflection mode has been developed since the late 1960's [2.40].

UNIVERSITY of the
WESTERN CAPE

In reflection UV-visible spectroscopy the light impinges perpendicularly onto the thin film sample, which consists of a thin layer of thickness (d) deposited onto a reflective substrate which has a finite thickness larger than that of d. A schematic of the reflection process is shown below in figure 2.27.

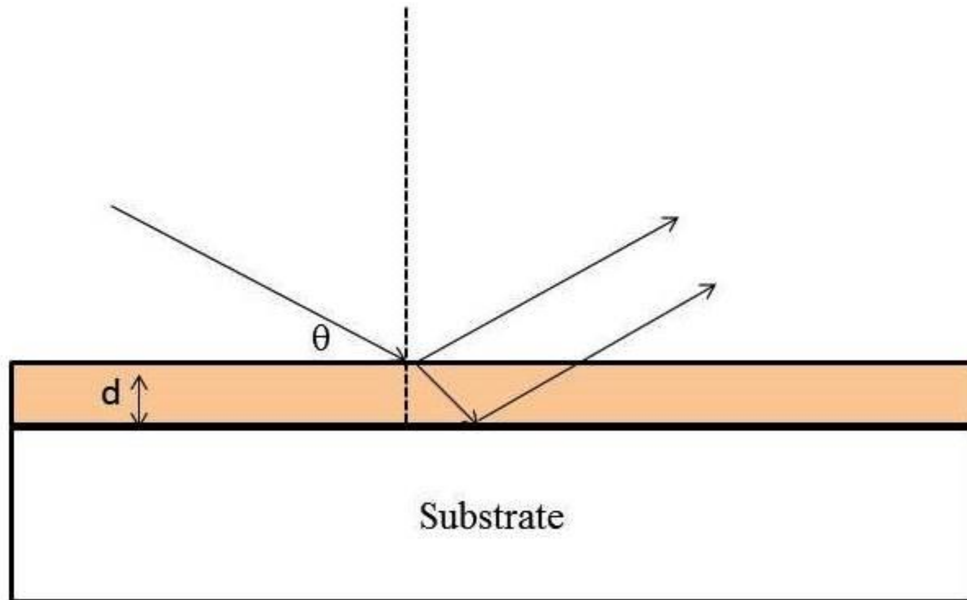

Figure 2.27: Schematic representation of the reflection of light, where θ is the angle of incidence, θ = 90° in our measurements.

UNIVERSITY of the
WESTERN CAPE

The medium through which the light travels before striking the surface is ambient air with a refractive index of 1. Due to the interactions of the light with the thin layer a reflection spectrum (R (λ)) is produced with interference fringes either due to thickness heterogeneities or from the substrate thin film interaction effects as shown in figure 2.28.

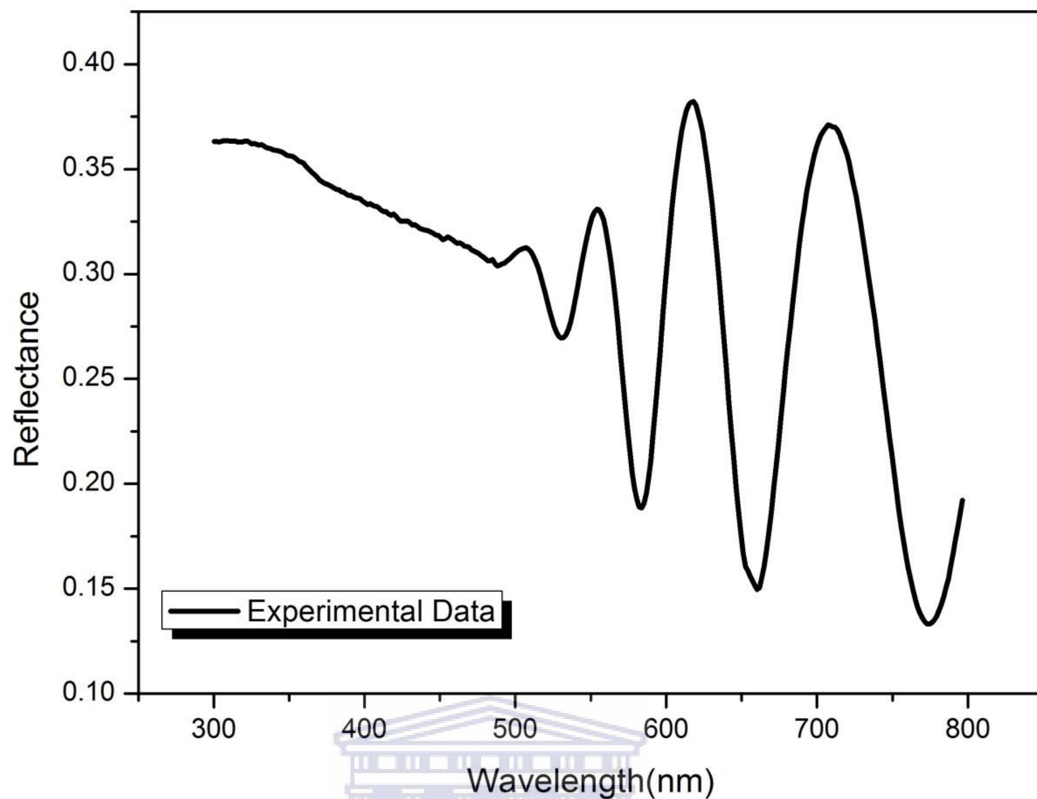

Figure 2.28: Typical Reflectance spectrum showing experimental data.

UNIVERSITY of the
WESTERN CAPE

As the light enters the new medium it is bent, changing the speed of the light as it enters the new medium. This change in speed is dependent on the optical properties of the material described by the complex refractive index of the layer, **n** = n – **i**k; the real and imaginary parts are known as the refractive index and the extinction coefficient respectively. The extinction coefficient is related to the absorption coefficient (α) (previously represented as η) by $\mathbf{I} = \mathbf{I}_0 e^{(-\alpha x)}$ and $\alpha = 4\pi(k/\lambda)$. The absorption coefficient is defined in terms of the intensity of the light at a depth, x, in the layer, and the intensity I_0 is at the surface [2.41].

As the light is reflected off the particles and atoms in the material, some of the light is scattered. This scattering process is due to thickness of the thin film and inhomogeneity in the thin film material, as well as substrate effects. Together they account for the formation of interference fringes in the reflection spectra. For

Transmission spectra, the optical constants as well as layer roughness of inhomogeneous thin films can be calculated as was done by Swanepoel [2.42]. Similarly, this process can be performed on reflection spectra. Conversely, inhomogeneity's caused by the formation of voids and crystallites containing varying dielectric functions as the host matrix needs to be described through the use of effective medium approximations (EMA).

Effective Medium Approximations

The effective medium approximation has been used to describe inhomogeneous systems and composite materials containing two or more materials with varying dielectric functions, such as that proposed by Bruggermann [2.43], for determination of the optical responses to stimuli.

UNIVERSITY of the
WESTERN CAPE

To describe an EMA system as uniform, consider two types of grains, A and B, that are mixed together such that the relative volume fractions, A and B, each containing their own dielectric functions contained in regions so small compared to the wavelength of the light that the regions in question may then be considered as a uniform effective medium approximation [2.44]. The EMA system will then have a uniform dielectric response taking into account the screening effects of charge accumulation at the boundaries of the varying regions. The composite material is made up of fractions of A and B of f_A and f_B respectively, such that

$$f_A + f_B = 1. \tag{2.73}$$

Then the effective dielectric function, ε_{eff}, of the EMA system is given by

$$f_A \varepsilon_A + f_B \varepsilon_B = \varepsilon_{eff}, \tag{2.74}$$

where ε_{eff} is the optical equivalent of capacitors in parallel if ε_B is the dielectric function of a material. The optical equivalence of a capacitor in series is given as

$$\frac{f_A}{\varepsilon_A} + \frac{f_B}{\varepsilon_B} = \frac{1}{\varepsilon_{eff}}. \qquad (2.75)$$

The Maxwell-Garnett mixing rule [2.45] is the earliest known form of effective mixing theories. In this mixing rule he assumed that the particles are spherical and compact in size. The spherical particles are surrounded by the host material, and are far removed from any neighbouring regions. This is described by

$$f_A \frac{\varepsilon_A - \varepsilon_B}{\varepsilon_A + 2\varepsilon_B} = \frac{\varepsilon - \varepsilon_B}{\varepsilon + 2\varepsilon_B}, \text{ where} \qquad (2.76)$$

$$f_A = \frac{\frac{4\pi}{3} r^3{}_A}{V}$$

is the volume fraction occupied by material A, and V is the total Volume of the EMA system. The Bruggermann Effective Medium Approximation (BEMA) deals with difficulties which the Maxwell-Garnett approach could not overcome. One of the considerations made by Bruggermann was to treat the inclusions as part of the effective medium itself and to determine them self-consistently. The self-consistency condition of the BEMA then simplified out to form:

$$0 = f_A \frac{\varepsilon_A - \varepsilon_h}{\varepsilon_A + s\varepsilon_h} + f_B \frac{\varepsilon_B - \varepsilon_h}{\varepsilon_A + s\varepsilon_h}, \qquad (2.77)$$

where h denotes the host material containing fractions of A and B. For an isotropic material described in three dimensions it is assumed that s = 2. The Maxwell-Garnett theory accounts for the spherical inclusions, and places them apart in isolation (cement microstructure), while the Bruggermann model allows the inclusions to intermix and can, therefore, account for the correlations due to self-consistent determination of the dielectric properties (aggregated microstructure).

Semiconductors, whether crystalline or amorphous in nature, possess band gaps. These band gaps separate the top of the valence band from the bottom of the conduction band as previously described. In the ensuing section, a discussion of the electronic properties of an amorphously bonded network will be described. Before defining the optical band gap of the amorphous material, it is necessary to revisit the density of states and conductivity of the layer, and to investigate the optical processes active in the material.

Optical Band Gap

One response of materials due to an electromagnetic stimulus is the photo conductivity; for an amorphous material this is described by [2.46]:

$$\sigma(\omega) = \frac{2\pi e^2 \hbar^3 \Omega}{m^2 \hbar\omega} \int \{f(E) - f(E + \hbar\omega)\} N(E) |P(\omega)|^2 N(E + \hbar\omega) dE. \qquad (2.78)$$

For the remainder of this section the frequency will be denoted with the use of ω. When interband transitions occur, N(E) and N(E+$\hbar$ω) refers to the valence and conduction band respectively. Ω is the size of the volume element containing one electron, f(E) is the Fermi-Dirac distribution, and P(ω) is the constant momentum matrix element for absorption. The strength of the optical absorption of the material is given by the logarithmic fraction of photons absorbed per cm^2. From this, the absorption coefficient (α) is proportional to the product of the density of occupied states with the density of the unoccupied states, which can be bridged by the energy, hv or $\hbar$ω, of the photon, if the probability of a transition occurring is the same for all states. The Fermi-Dirac distribution gives a good approximation of interband transitions when T = 0 K. The photoconductivity equation can then simplify to form

$$\sigma(\omega) = \frac{2\pi e^2 \hbar^3 \Omega}{m^2 \hbar\omega} \int N(E) |P(\omega)|^2 N(E + \hbar\omega) dE, \qquad (2.79)$$

UNIVERSITY of the
WESTERN CAPE

which can further be rewritten in terms of α such that

$$\alpha(\omega) = \frac{2\pi e^2\hbar^3\Omega}{m^2\hbar\omega\varepsilon_0 n(\omega)c} \int N(E)|P(\omega)|^2 N(E+\hbar\omega)dE. \quad (2.80)$$

The absorption coefficient is related to the photoconductivity through [2.46]

$$\alpha(\omega) = \frac{\sigma(\omega)}{\varepsilon_0 n(\omega)c}. \quad (2.81)$$

A schematic of the density of states is shown in figure 2.29 below.

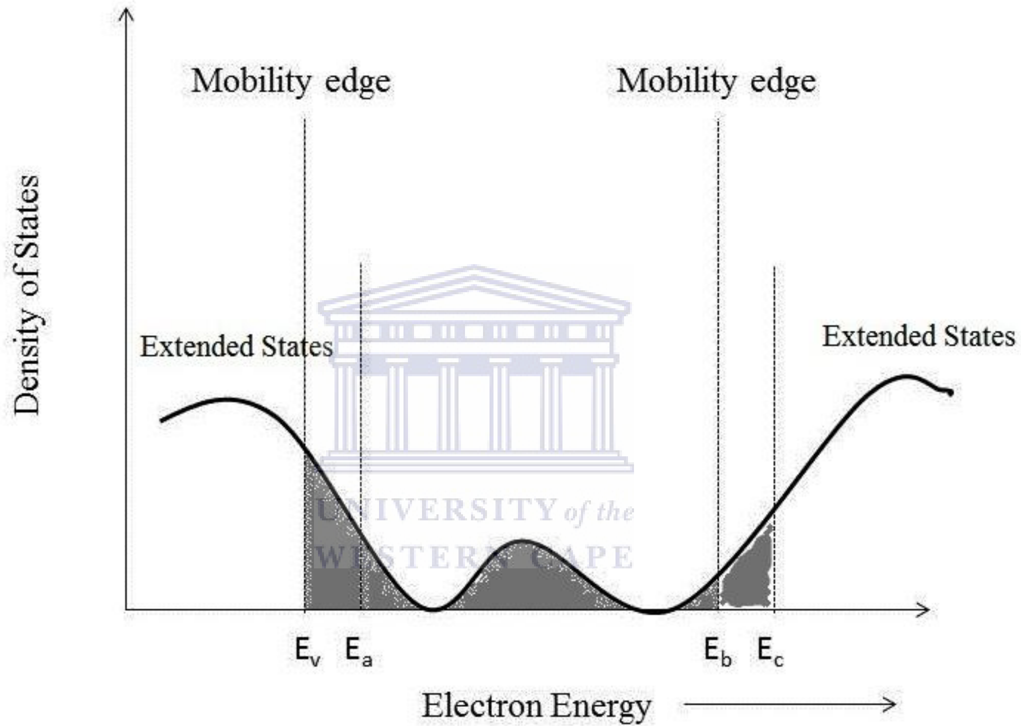

Figure 2.29: Density of states showing extended states and mobility edges [2.47].

E_a and E_b are the localised states amongst the mobility states in the valence and conduction band respectively. The density of states for the valence and conduction bands is given by [2.47]:

$$N = N_v\left(\frac{E_a - E}{E_a - E_v}\right)^p \; for\; E \le E_a \text{ and}$$

$$N = N_c\left(\frac{E - E_b}{E_c - E_b}\right)^q \; for\; E \ge E_b, \quad (2.82)$$

where p and q are the density of states distribution in the valence and conduction bands respectively. Equation 2.83 is formed by substituting equation 2.82 and equation 2.81 into equation 2.80, such that a solution for the absorption coefficient is given as [2.47]

$$\alpha(\omega) = \frac{2\pi e^2\hbar^3\Omega}{m^2\hbar\omega\varepsilon_0 n(\omega)c}\frac{\Gamma(p+1)\Gamma(q+1)}{\Gamma(p+q+2)} \times \frac{N_v N_c}{(E_a-E_v)^p(E_c-E_b)^q} < |P(\omega)|^2 > (\hbar\omega - E_g)^{1+p+q}. \qquad (2.83)$$

The momentum transition matrix for absorption P(ω) is also averaged over the energy range, and is assumed to be independent of ω, such that

$$[\alpha(\omega)n(\omega)\,\hbar\omega]^{1/1+p+q} = B_g(\hbar\omega - E_g), \qquad (2.84)$$

where B_g is a constant, and E_g is the optical band gap.

The Tauc band gap [2.48] describes a situation where p = q = ½, and at this point the DOS distribution for the valence band as well as the conduction band takes on a parabolic shape. The band gap is taken from the extrapolation of $[\alpha(\omega)n(\omega)\,\hbar\omega]^{1/2}$ versus $\hbar\omega$. The extrapolation is performed to a point where α(ω) = 0, that is as the line crosses the x-axis, and the value at that point equals the Tauc band gap.

UNIVERSITY of the
WESTERN CAPE

The OJL model for An Amorphous Semiconductor

The O'Leary, Johnson, Lim (OJL) [2.49] model is an empirical model which describes the distribution of electronic states in an amorphous semiconductor, with the determination of the functional form of the optical absorption spectrum and focuses on the joint density of states which dominates the absorption spectrum in the photon energy range. The aim of the model is to allow the experimentalist to physically interpret the significance of the absorption spectrum.

The OJL model adopted an elementary empirical model for the distribution of electronic states. The density of states (DOS) of the conduction band is given as

$$N_c(E) = \frac{\sqrt{2}{m_c^*}^{3/2}}{\pi^2\hbar^3}\begin{Bmatrix} \sqrt{E-V_c},\ E \geq V_c + \frac{\gamma_c}{2} \\ \sqrt{\frac{\gamma_c}{2}}\exp\left(-\frac{1}{2}\right)\exp(\frac{E-V_c}{\gamma_c}), \\ E < V_c + \frac{\gamma_c}{2} \end{Bmatrix}, \quad (2.85)$$

where m_c^* represents the DOS effective mass for the conduction band, V_c is the disorderless band edge of the conduction band, γ_c reflects the breadth of the conduction band tail, and $V_c + \gamma_c/2$ is the transition point between the square root and the linear exponential distribution of states [2.42]. $N_c(E)$ denotes the continuous first derivative at this point, $V_c + \gamma_c/2$. A similar situation can be described for the valence band DOS, such that:

$$N_v(E) = \frac{\sqrt{2}{m_v^*}^{3/2}}{\pi^2\hbar^3}\begin{Bmatrix} \sqrt{\frac{\gamma_v}{2}}\exp\left(-\frac{1}{2}\right)\exp(\frac{V_v-E}{\gamma_v}) \\ , \\ E \geq V_v + \frac{\gamma_v}{2} \quad , \\ \sqrt{V_v-E},\ E < V_v - \frac{\gamma_v}{2} \end{Bmatrix}, \text{ where} \quad (2.86)$$

m_v^* represents the DOS effective mass for the valence band, V_v is the disorderless band edge of the valence, γ_v reflects the breadth of the valence band tail, and V_v - $\gamma_v/2$ is the transition point between the square root and the linear exponential distribution of states. $N_v(E)$ denotes the continuous first derivative at this point, V_c - $\gamma_c/2$.

Band tailing in an amorphous material can act as a measure of disorder, and is provided by the tail breadth parameters γ_c and γ_v of the conduction and valence bands respectively. The sensitivity in $N_c(E)$ with variations in γ_c was tested, and when $\gamma_c \rightarrow 0$ the conduction band DOS terminates abruptly at the disorderless band edge, V_c. For finite values of γ_c the distribution of the tail states appears below the mobility edge. For increasing values of γ_c away from the disorderless limit the total number of localised tail states increases, with the encroachment of

the tail states distribution into the band gap area. Similar results were observed for the DOS functions, $N_v(E)$. Excellent agreement was observed between the empirical model and experimental values [2.42].

2.3.7.3 Experimental Setup

UV-Vis spectroscopy was performed in Reflection mode using a Semiconsoft mProbe system, employing a diode array detection system allowing simultaneous measurements of both the UV and visible spectrum. Samples belonging to sets MW 303 and MW 304 deposited on c-Si substrates as-deposited as well as the annealed were measured. The visible spectrum was measured with the use of a halogen bulb, while the UV part of the spectrum was measured using a Deuterium lamp. The light from both sources travel along fibre optic cables and measurements were conducted on the spectral range 200 to 1000 nm.

The reflectance spectra were analysed using Scout® [2.50] software making use of an iterative function employing the OJL fitting parameters as described above. Included in the optical model were EMA structures to help describe the complexities of the amorphous material.

UNIVERSITY of the
WESTERN CAPE

References

[2.1] K.E. Spear, *Pure & Appl. Chem.*, **54** (1982) 1297.

[2.2] Y. Xu, X.-T. Yan, '*Chemical Vapour Deposition, An Integrated Engineering Design for Advanced Materials*', Springer-Verlag London Limited (2010).

[2.3] H. Wiesmann, A. K. Gosh, T. McMahon, and M. Strongin, *J. Appl. Phys*. **50**, (1979) 3752.

[2.4] H. Matsumura, *Jap. J. Appl. Phys*., Part 2-Letters **25,** L949-L951 (1986).

[2.5] R.E.I. Schropp, *Thin Solid Films*, **395** (2001) 17.

[2.6] C.J. Arendse, '*Hydrogenated Amorphous Silicon: Optical Properties and Hydrogen Concentration*', MSc thesis, University of the Western Cape, South Africa.

[2.7] B. Stannowski, J. K. Rath and R. E . I Schropp, *J. Appl. Phys.*, **93** (2003) 2618.

[2.8] R.E.I. Schropp, C.H.M. van der Werf, V. Verlaan, J. K. Rathn H. Li, *Thin Solid Films*, **517** (2009) 3039.

[2.9] V. Verlaan, Z.S. Houweling, C.H.M. van der Werf, I.G. Romijn, A.W. Weeber, H.D. Goldbach, R.E.I. Schropp, *Thin Solid Films*, **516** (2008) 533.

[2.10] Y.J. Shi, B.D. Eustergerling, X.M. Li, *Thin Solid Films*, **516** (2008) 506.

[2.11] G.V. Gadiyak, V.G. Gagiyak, M.L. Kosinova, E.G. Salman, *Applied Surface Science*, **113/114** (1997) 647.

[2.12] Z. Lu, P. Santos-Filho, G. Stevens, M.J. Williams, G. Lucovsky, *J. Vac. Sci. Technol*. **A 13** (1995) 607.

[2.13] F. L. Martínes, and I. Mártil, G. González-Díaz, B. Selle, I. Sieber, *J. Appl. Phys*. **86** (1999) 2055.

UNIVERSITY of the
WESTERN CAPE

[2.14] M. Birkholz, '*Thin Film Analysis by X-Ray Scattering'*, Wiley-VCH Verlag GMbH & Co. (2006).

[2.15] B.D. Cullity, '*Elements of X-Ray Diffraction*', Addison-Wesley Publishing Compant, Inc. (1956).

[2.16] W.H. Bragg, W.L. Bragg, *Proc. R. Soc. Lond. A*, **88** (1913) 428.

[2.17] W.E. Smith, G. Dent, '*Modern Raman Spectroscopy- A Practical Approach'*, John Wiley & Sons, Ltd. (2005).

[2.18] T. Searle, '*Properties of Amorphous Silicon and its Alloys'*, Inspec, The Institute of Electrical Engineers, London, (1988)

[2.19] C.J. Oliphant, '*Hot-Wire Chemical Vapour Deposition of Nanocrystalline Silicon and Silicon Nitride: Growth Mechanisms and Filament Stability*', PhD thesis, The University of the Western Cape, South Africa.

[2.20] W.S. Lau, '*Infrared Characterisation for Microelectronics'*, World Scientific Publishing Co. Pte Ltd. (1999).

[2.21] B. George, P. McIntyre, '*Infrared Spectroscopy'*, John Wiley & Sons (1987).

[2.22] M.H. Brodsky, M. Cardona, J.J. Cuomo, *Physical Review B*, **16** (1977) 16.

[2.23] N. Maley, *Physical Review B*, **46** (1992) 46.

[2.24] F. Demichelis, F. Georgis, C.F. Pirri, *Philosophical Magazine B*, **74** (1996) 155.

[2.25] F. Georgis, P. Rava, R. Galloni, R. Rizzoli, C. Summonte, G. Crovini, F. Demichelis, C.F. Pirri, E. Tresso, V. Rigato, *Journal of Non-crystaline Solids***198-200** (1996) 596.

[2.26] E. Bustarret, M. Bensouda, M.C. Habrard, J.C. Bruyère, S. Poulin, S.C.

UNIVERSITY of the
WESTERN CAPE

Gujrathi, *Physical Review B*, **38** (1998).

[2.27] D. V. Tsu, G. Lucovsky, M.J. Mantini, *Physical Review B*, **88** (1986) 33.

[2.28] J. L'Ecuyer, C. Brassard, C. Cardinal, J. Chabbal, L. Deschenes, J.P. Labrie, B. Therrault, J.G. Martel, R. St-Jacques, *J. Appl. Phys*. **47** (1976) 381.

[2.29] W.M.A. Bik, F.H.P.M. Habraken, *Rep. Prog. Phys*. **56** (1993) 859.

[2.30] T.L. Alford, L.C. Feldman, J.W. Mayer, '*Fundamentals of Nanoscale Film Analysis*, Springer-Science and Business Media Inc., (2007)

[2.31] M. Mayer, SIMNRA UserGuide.

[2.32] G. Binnig, C.F. Quate, Ch. Gerber, *Phys. Rev. Lett*., **56** (1986) 930.

[2.33] G. Binning, H. Rohrer, Ch. Gerber, and E. Weibel, *Phys. Rev. Lett*. **49** (1982) 57.

[2.34] P. Eaton, P. West, '*Atomic Force Microscopy'*, Oxford University Press (2010).

UNIVERSITY of the
WESTERN CAPE

[2.35] Accessed on: September 2012, from: www.veeco.com

[2.36] M.T. Postek, K.S. Howard, A.H. Johnson, K.L. McMichael, '*Scanning Electron Microscopy, A Students Handbook*', Ladd Research Industries (2001).

[2.37] A.V. Crewe, D.N. Eggenberger, J. Wall, L.M. Welter, *The Review of Scientific Instruments*, **39**, (1968) 576.

[2.38] J. K. Holt, D. G. Goodwin, A. M. Gabor, F. Jiang, M. Stavola, H. A. Atwater, *Thin Solid Films*, **430** (2003) 37.

[2.39] J.M. Ziman, '*Principles of the Theory of Solids*', Cambridge University Press (1964).

[2.40] S. G. Tomlin, *J. Phys. D*, **1** (1968) 1667.

[2.41] M. Fox, '*Optical Properties of Solids*', Oxford University Press (2001).

[2.42] R Swanepoel, *J. Phys. E: Sci. Instrum.*, **17** (1984) 896.

[2.43] D.A.G. Bruggermann, *Ann. Physik (Leipzig)*, **24** (1935) 636.

[2.44] K. Kim, PhD Thesis, North Carolina State University, Raleigh, USA (2006).

[2.45] J.C. Maxwell Garnett, Phil. Trans. *R. Soc. Lond. A* (1904) 203.

[2.46] N. F. Mott and E. A. Davis, in '*Electronic Processes in Non-Crystalline Materials*', Clarendon Press, Oxford, U.K. (1971).

[2.47] R. Zallen, in '*The Physics of Amorphous Solids*', John Wiley & Sons (1983).

[2.48] J. Tauc, R. Grigorovici, A. Vancy, *Phys. Stat. sol.*, **15** (1966) 627.

[2.49] S.K. O'Leary, S.R. Johnson, P.K. Lim, *J. Appl. Phys.*, **82** (1997) 3334.

[2.50] W. Theiss Hard- and Software, Accessed on April 2012, from http://www.mtheiss.com.

UNIVERSITY of the WESTERN CAPE

Chapter 3: Results and Discussion

3.1 Introduction

The as-deposited thin films investigated can be described as silicon rich- (SR) SiN_x thin films. Although they both contain nitrogen, one set, MW 304 contains more nitrogen than the other. The N/Si ratio (x-value) in SiN_x was determined using heavy ion ERDA [3.1], which was conducted as part of another study, and therefore the heavy-ion depth profiling results and plots are not shown in this thesis.

The as-deposited set with the lowest ammonia flow rate, MW 303, contained the lowest fraction of nitrogen to silicon, $x = 0.12$, while the second set, MW 304 had a higher flow rate of ammonia combined with the silane gas and more nitrogen was incorporated into the silicon matrix, with $x = 0.26$. The varying amounts of nitrogen incorporated into the matrix affects the characteristics of the resulting thin films. This is discussed in the sections which follow.

The as-deposited thin films are assumed to be homogenous in every respect (N/Si ratio and thickness) as described by the gas law theory and interaction of the molecules with themselves and the surrounding chamber. During the optical modelling it became apparent that this was not the case, as more complex models were developed. The inhomogeneity is due to the position and size of the substrates in relation to the catalytic wire, thus causing the thin film to form heterogeneously. Large substrates were used during the deposition of the thin films as described in Section 2.2.1. Consequently the size of the substrate in

UNIVERSITY of the
WESTERN CAPE

comparison to the area covered by the hot wire is that the radicals which may form is given time to react with other gas species before settling onto the substrate, as well as the edges may not be homogenously cover by the thin film.

Computational simulation of Si_3N_4 has been performed with the use of molecular dynamics, and the Carl Parrinello method [3.2]. The molecular dynamics model which was proposed began with c-Si bonded in a diamond-cubic lattice. The lattice was subsequently changed to that of Si_3N_4 with the insertion of nitrogen atoms at intermediate distances along the Si-Si bond, exhibiting a Si-N bond length of 1.729 Å. An empty state was observed in the top of the valence band in the model, and two hydrogen atoms were added close to two Si atoms which were threefold coordinated, thus preventing dangling bonds from accruing. After relaxation was achieved the H atoms moved to a site closer to two N atoms, the electronic and structural properties were only slightly affected by the addition of hydrogen to the system.

UNIVERSITY of the
WESTERN CAPE

Experimentally the valence band of SiN_x has been shown to comprise of two subbands which is kept apart by an inner energy gap [3.2]. Furthermore the top of the valence band has been shown to be constructed of the nonbonding nitrogen 2p lone-pair band, this arrangement is typical of the planar bonding exhibited in an $N\text{-}Si_3$ unit [3.3]. This is in agreement with the computational model discussed above. The model also describes the conduction band as mainly consisting of Si-N antibonding pairs, which is common in the short range bonding environment of tetrahedral units [3.2].

Hydrogen dilution of SiH_4 + NH_3 during the deposition of silicon nitride by Plasma Enhanced Chemical Vapour Deposition has shown that nitrogen

incorporation is heightened while the incorporation of hydrogen is observed to decrease [3.4]. The nitrogen incorporation can be increased either through an increased flow rate of NH_3 gas, or through the increase of the gas pressures during the deposition [3.5]. Both methods yield the same effects on the characteristics of the thin films [3.5]. It has been noted that the optical properties of silicon nitride is dependent on the x-value. The optical energy gap is observed to increase, while the refractive index decreases as the N/Si ratio increases [3.6]. These trends have been confirmed for other methods of deposition as well [3.7]. Another optical constant which is affected by the increasing nitrogen content is the oscillator energy (E_0), which is observed to increase as the absorption edge moves to higher energies with the incorporation of nitrogen to the silicon matrix, while at the same time the dispersive energy parameter (E_d) is observed to remain fairly constant [3.6].

UNIVERSITY of the
WESTERN CAPE

FTIR bonding configurations for SiN_x, like other properties of the thin films, are also affected by an increase in nitrogen incorporation, and a shift to higher wavenumbers is observed as the x-value increases [3.8]. The shift to higher wavenumbers of the Si-H network is assigned to the high electronegativity of the nitrogen atoms, which causes the bond strength fluctuations in the back bonding of the hydrogen complexes [3.8]. SiN_x thin films may be characterised as either SR-SiN_x or nitrogen rich (NR)-silicon nitride with the determination of the maximum absorption in the IR range. In SR-SiN_x the maximum absorption will be located near the Si-H bonding configuration at approximately 610 cm^{-1}. For NR thin films the maximum absorption will be associated with the Si-N bonding modes [3.5].

The growth of SiN_x by rf-magnetron sputtering can be split into two phases [3.9]: (i) during the first phase of growth, dense, smooth, uniform thin film are formed until a thickness of roughly 300nm is achieved, where after the second phase of growth takes over. (ii) During this phase column structures begin to form on the surface of the film, increasing surface roughness as this occurs.

SiN_x is used as a passivation layer and antireflective coating on top of microcrystalline silicon solar cells, which undergoes a final firing step, during which hydrogen effuses into the solar cell and pacifies the grain boundaries and any dangling bonds which may exists [3.10]. It is therefore important to determine the reaction of the thin films to extreme temperatures. At temperatures below 400°C not much change to the structural and optical properties has been observed [3.4]. Major changes to the structure of the SiN_x thin films only occur after annealing at 500°C. These changes are related to the effusion and loss of hydrogen which is bonded to both Si and N. Thin films of varying composition will experience varying rates of effusion and losses.

UNIVERSITY of the
WESTERN CAPE

Not all the annealing temperatures are shown for each characterisation technique; the highest temperature shown is dependent on the type of substrate used in the analytical technique, and whether the thin films remained intact during the annealing experiment. The thin films deposited on the Corning 7059 glass could not withstand annealing temperatures of 700°C for both the MW 303 and MW 304 annealing series, and after annealing at 700°C some deformation of the substrate occurred.

The thin films deposited on the c-Si substrates belonging to the MW304 set remained stable at the highest annealing temperature of 1000°C compared to the

MW303 set which behaved differently. The thin films belonging to the MW 303 set could not withstand annealing temperatures above 500°C, and after being exposed to temperatures exceeding this annealing regime no film was detected as it had peeled off due to stress and strain in the bonding network caused by the effusion of the hydrogen gas during the annealing process.

3.2 Characterisation of a-SiN_x:H

3.2.1 Structural Characteristics

3.2.1.1 X-ray Diffraction

UNIVERSITY of the
WESTERN CAPE

Diffraction patterns were obtained for the thin films deposited on the Corning 7059 glass substrates for both sets, as-deposited as well as annealed. The structure of the thin films were characterised to be amorphous, with no long range order being detected as shown in the XRD section of Chapter 2.

It is not expected that any significant crystallisation should take place at annealing temperatures lower than ~800°C [3.11], but this may be dependent on the initial deposition parameters, as well as the method of producing the thin films. Figure 3.1 below shows the diffraction patterns belonging to MW 304 and MW 303 which was annealed at 700°C. No crystalline peaks are observed after the high temperature annealing experiment as the lack of long range order was preserved, and thus the films are characterised to be amorphous. Since no long range order was observed, Raman spectroscopy was then used to determine if short range order was present thus indicating the presence of Si crystallites.

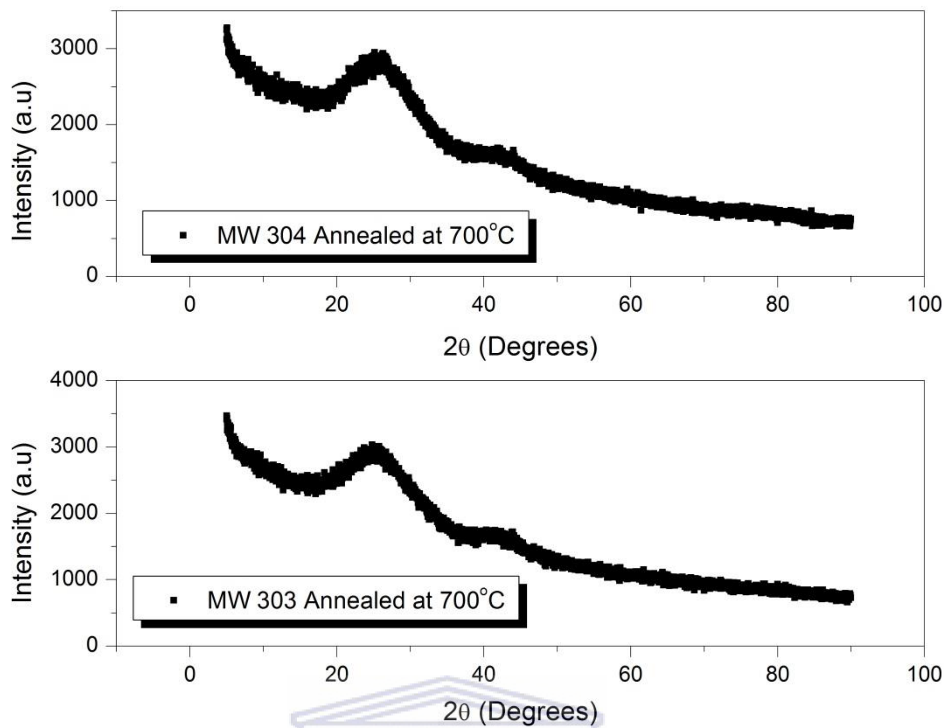

Figure 3.1: XRD patterns showing no crystalline features.

3.2.1.2 Raman Spectroscopy

UNIVERSITY of the
WESTERN CAPE

Raman Spectroscopy was performed on the SiN_x thin films deposited on the Corning 7059 substrates as a way to determine the presence of silicon either in its crystalline or amorphous form. No long range order was detected in the silicon matrix with the absence of any crystalline feature around 520 cm^{-1} belonging to c-Si which may have been induced [3.11, 3.12]. XRD results were confirmed with the further absence of any short range bonding order which may have appeared between 480 cm^{-1} and 520 cm^{-1}.

Since the SiN_x thin films are characterised to be SR-SiN_x, a relationship between the full width half maximum (FWHM) of the transverse-optical (TO) peak belonging to the a-Si contribution (Γ) and the RMS bond angle ($\Delta\vartheta_b$) can be established [3.13]:

$$\frac{\Gamma}{2} \cong 7.44 + 3.2\Delta\vartheta_b \,, \qquad (3.1)$$

where Γ and $\Delta\vartheta_b$ are measured in cm^{-1} and degrees respectively. The value of $\Delta\vartheta_b$ for a-Si:H was found to vary between 7.0^o and 14.1^o according to Berntsen [3.14]. With the influence of nitrogen in the matrix, $\Delta\vartheta_b$ was found to vary between 6.0^o and 18.0^o [3.15].

The values of the FWHM (Γ) belonging TO peak of the a-Si:H contribution were calculated for the respective spectra, MW 303 and MW 304 both the as-deposited and annealed at 700^oC. The TO peak was analysed to describe the change in the bonding configuration between the as-deposited and annealed samples since the SiN_x thin films presented are silicon-rich. The overall matrix consists of a hydrogenated amorphous silicon network with nitrogen intermixed the results of the TO peak analysis is displayed in Table 3.1 below.

Table 3.1: Table of Γ-values for MW 303 and MW 304 as-deposited and annealed.

UNIVERSITY of the
WESTERN CAPE

	MW 303		**MW 304**	
	Γ (cm^{-1})	**$\Delta\vartheta_b$ (^{o})**	**Γ (cm^{-1})**	**$\Delta\vartheta_b$ (^{o})**
As-deposited	65.36	7.89	68.77	8.42
Annealed	71.41	8.83	84.28	10.84

Large Γ values are characteristic of the amorphous nature of the thin films [3.16]. The $\Delta\vartheta_b$ values calculated using Equation (3.1) correlates well with what has been described by Berntsen and B. P. Swain *et al.* [3.14, 3.15]. The broadening of the TO peaks in both annealing series is an indication of an increase in disorder due to the rearrangement of bonds during the thermal treatment [3.17].

The as-deposited spectra show the presence of Si-Si and Si-N clusters which are amorphously bonded to each other, these clusters are positioned along 200 – 500 cm^{-1} and 800-1100 cm^{-1} respectively [3.18]. After annealing the thin films at 700°C a decrease in vibrational intensities is observed with the diminishing and almost complete disappearance of the SiN_x mode centred around 800 cm^{-1} as well as the 2TO mode associated with a-Si:H centred at 950 cm^{-1}. The disappearance of the SiN_x mode is indicative of the rearrangement of bonds which occurs after exposure to high temperature. Figure 3.2 displays the Raman spectra of the as-deposited as well as the annealed samples at 700°C for both annealing series.

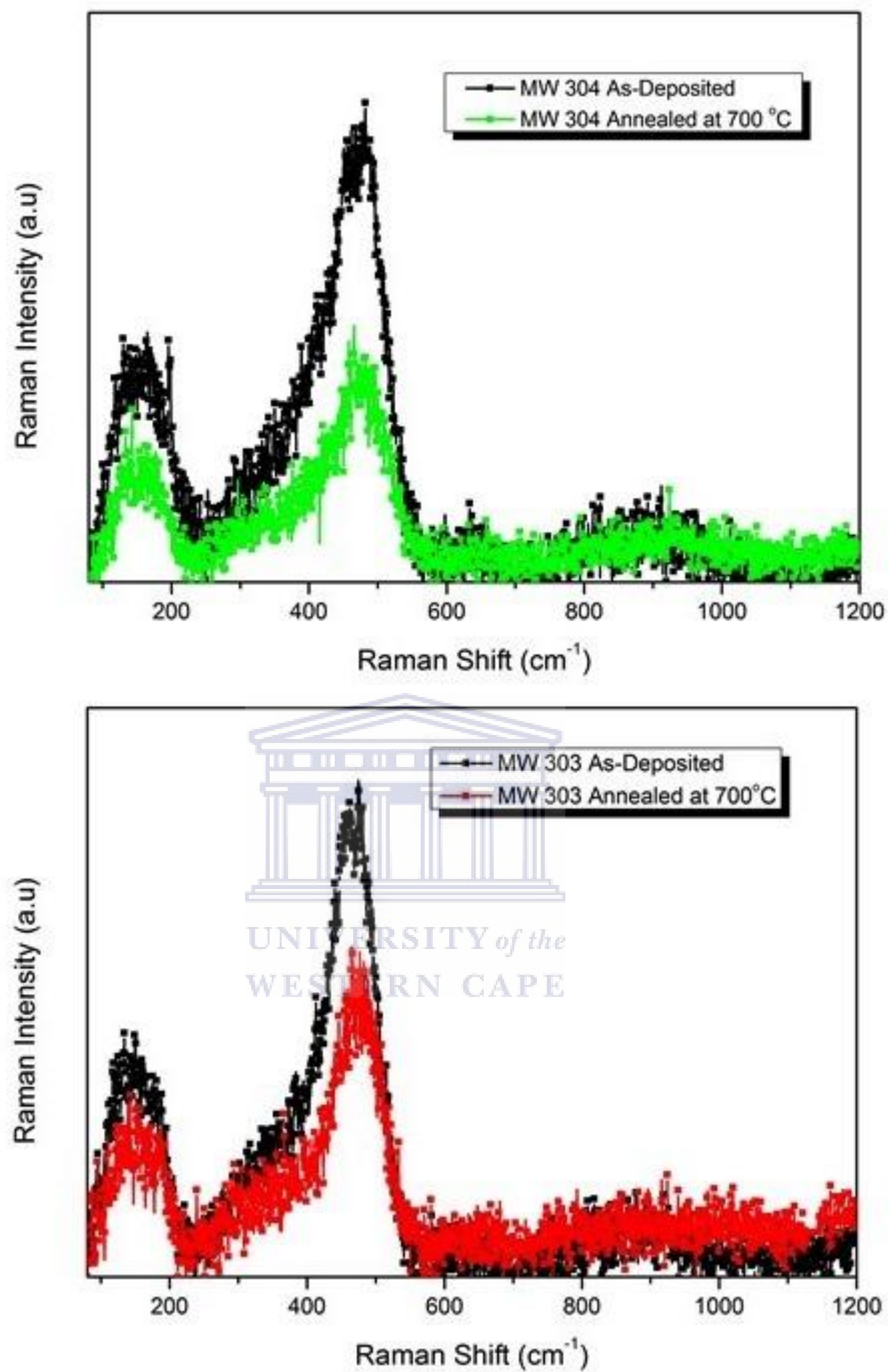

UNIVERSITY of the
WESTERN CAPE

Figure 3.2: Raman spectra for (a) MW 304 and (b) MW 303 of the as-deposited and annealed thin films.

3.2.2 Compositional Properties

3.2.2.1 Introduction

The compositional structure and hydrogen content of the SiN_x thin films is characterised through the use of FTIR spectroscopy and ERDA. The SiN_x thin films described in this study can be used as an anti-reflective coating as well as a passivation layer on top of silicon solar cells [3.10]. Understanding the changes in the bonding configuration and total hydrogen content is important for describing the passivation pathways, as shown by Verlaan [3.19].

3.2.2.2 Fourier Transform Infrared Spectroscopy

FTIR was performed on samples deposited on c-Si substrates, and the modes were treated as described in Chapter 2. A qualitative discussion of the changes in the bonding configurations during the heat treatment is now undertaken. Difference spectra were calculated for the main nitrogen and hydrogen containing modes centred around 850 cm^{-1} and 2100 cm^{-1} respectively. The difference spectra were calculated from the as-deposited thin films and the corresponding annealed counterpart for each temperature as displayed in the figure 3.3 below.

A positive result shows an increase in vibrational intensities for a specific bonding configuration, and a negative result indicates a loss in intensity of the bonding configuration. The overall consequence of annealing whether it is a positive or negative result indicates that a structural rearrangement has taken place. This rearrangement could lead to a total destruction of the bonding configuration and the increase of another bonding type due to the heat treatment, similar to what has been observed in Raman spectroscopy. N-H stretching bonds were not observed in

UNIVERSITY of the
WESTERN CAPE

all of the as-deposited thin films, and if the bonding configuration was present, only trace amounts were detected in the as-deposited samples. After the heat treatment some bond configurations changes were induced causing the N-H stretching bonds to disappear. The large negative peaks in the difference spectra is as a result from the annealed spectra containing less of the specific bonding configuration compared to that of the as-deposited spectra. The absence of the N-H peaks in the as-deposited spectra is as a result of the in homogeneities described earlier.

UNIVERSITY of the
WESTERN CAPE

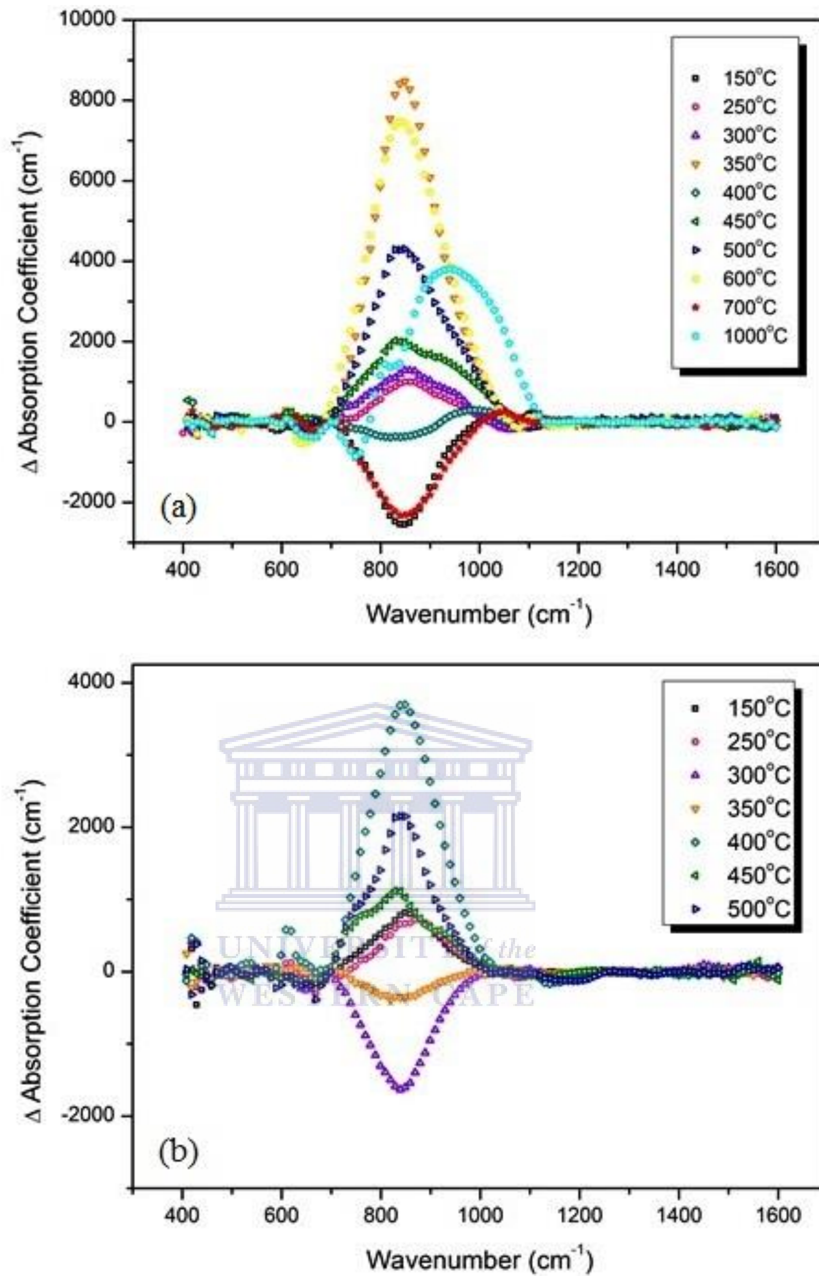

Figure 3.3: Difference spectra for the main SiN containing modes, (a) MW 304 and (b) MW 303, each centred around 850 cm^{-1}.

In MW 304 a shift to higher wavenumbers is observed for the Si-N bonding modes as well as an enhancement of the mode after excessive heat treatment [3.12]. This is confirmed by figure 3.4 which represents the shift in peak positions for the main Si-N bonding configurations, usually SiN_n stretching vibration and NSi_3 asymmetrical vibrations are located at 790 cm^{-1} and 850 cm^{-1} respectively.

The rearrangement and enhancement of the Si-N modes at 790 cm^{-1} and 850 cm^{-1} at high temperatures is promoted by a decrease in the 2100 cm^{-1} mode in both series. This has been previously observed in SiN_x thin films with a vastly varying composition [3.20], compared to what is described by the thin films in this.

The modes observed in the as-deposited thin films were already shifted away from the ideal position and were found to be at slightly higher wave numbers; this is attributed to the deposition conditions, which causes the chemical bonds to form away from their ideal bonding configuration. This ultimately impacts on the differences in electronegativity between the Si-H bonds and Si-N bonds in silicon-rich silicon nitride [3.21, 3.22]. A further shifting of the modes was then experienced as the annealing temperature increased. The shifting to higher wavenumbers could be caused through a network interchange reaction which occurs at high temperatures [3.23]. This reaction involves all the bonds present in the thin film and often leads to the loss in both hydrogen as well as nitrogen [3.23]:

UNIVERSITY of the
WESTERN CAPE

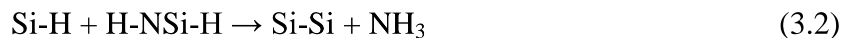

$$\text{Si-H} + \text{H-NSi-H} \rightarrow \text{Si-Si} + \text{NH}_3 \quad (3.2)$$

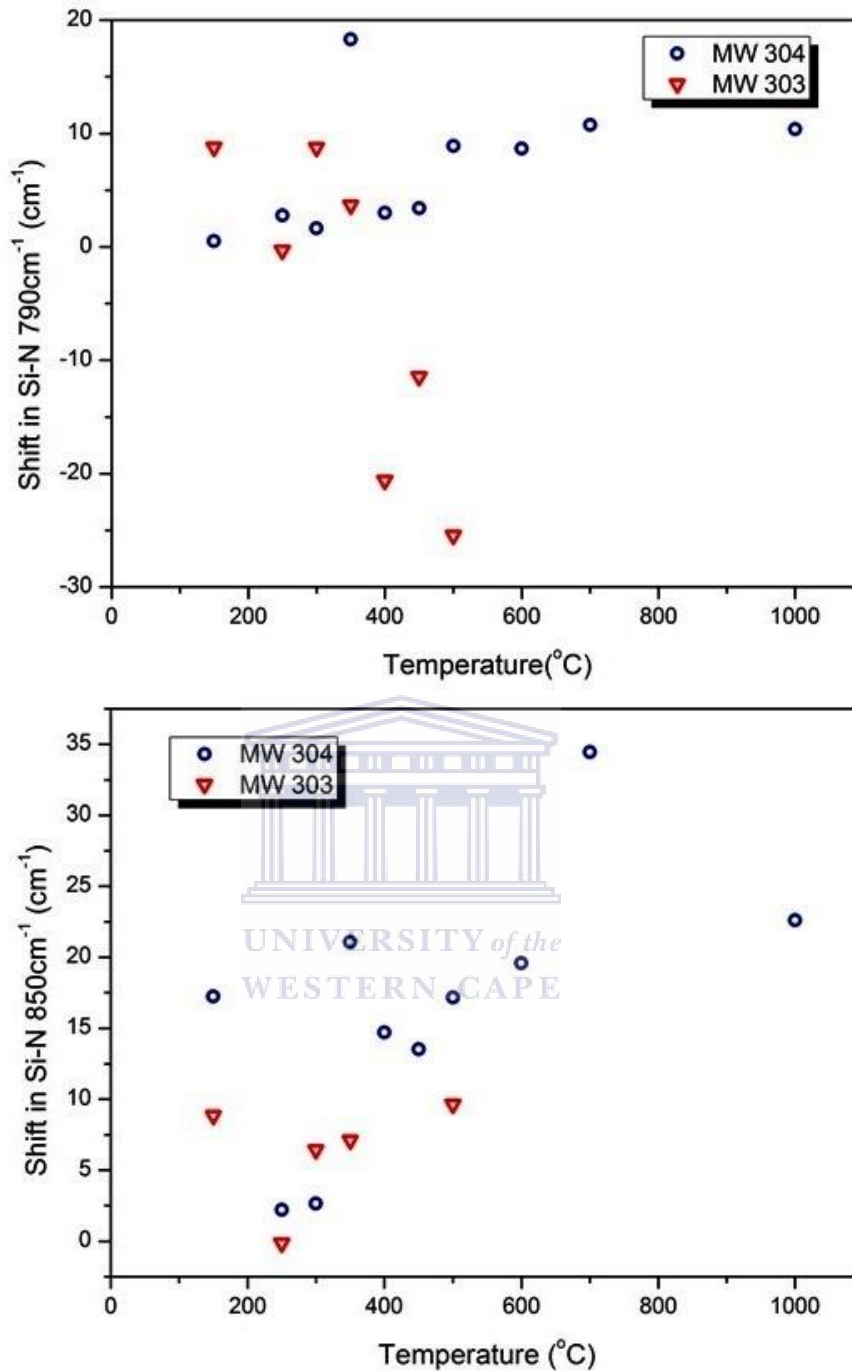

UNIVERSITY of the
WESTERN CAPE

Figure 3.4: Difference in peak positions for the main Si-N modes (a) 790 cm^{-1} (b) 850 cm^{-1}.

A shift to lower wavenumbers is observed for MW 303 for the stretching vibrations at 790 cm^{-1}. This trend is opposite to what is observed for the higher N/Si ratio film (MW 304), which has an overall increasing trend for the same mode. The change in the asymmetrical vibrating mode belonging to MW 303

decreases slightly but when annealed at 500°C the change in the mode enhances again. It is this difference in bonding rearrangements which cause the stability of the thin films to differ so vastly at high temperatures, and causes the delamination of the thin film to occur when exposed to temperatures exceeding 600°C.

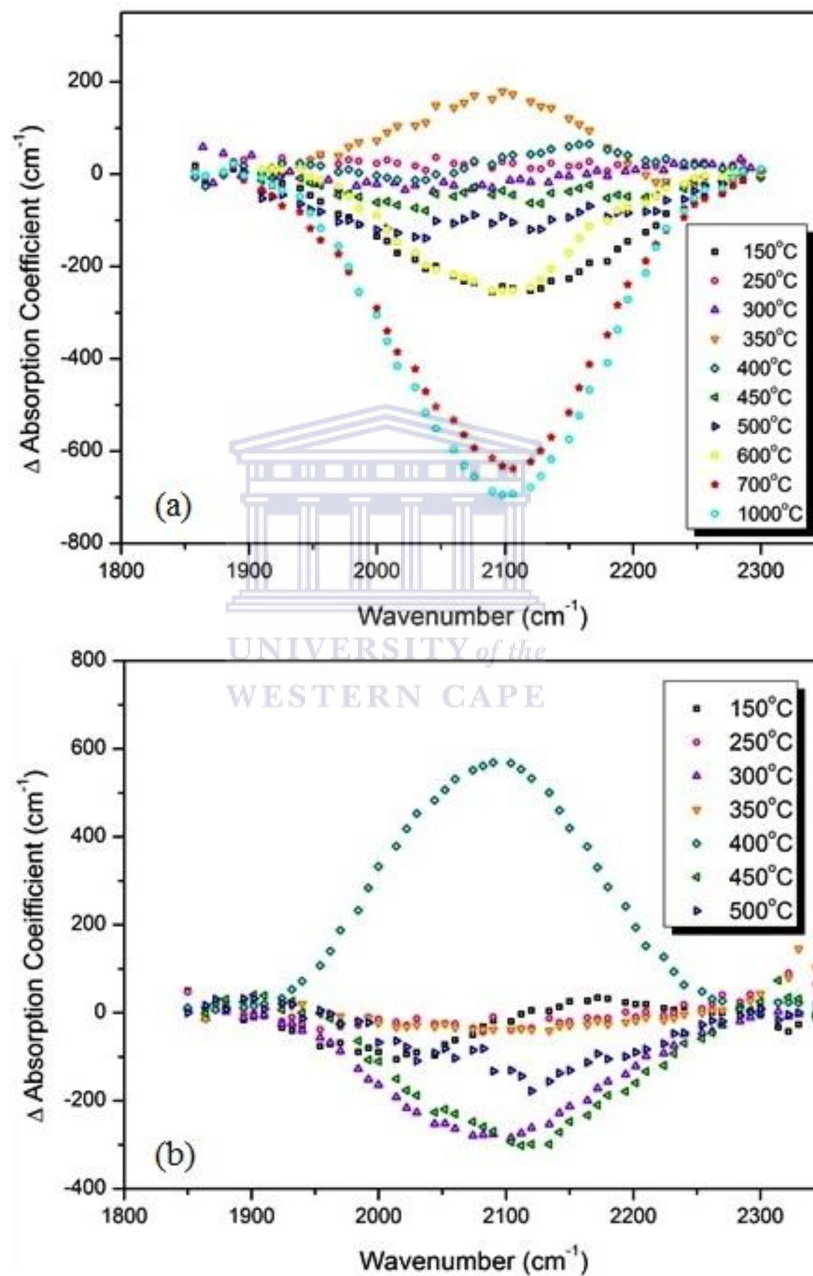

UNIVERSITY of the
WESTERN CAPE

Figure 3.5: Difference spectra for the Si-H and SiN-H bonding configuration of (a) MW 304 and (b) MW 303 centred around 2100 cm^{-1}.

Figure 3.5 above displays the evolution of the SiN, Si-H and SiN-H bonding configuration. The evolution kinetics was explained in Chapter 2; the decrease in the SiN intensities after annealing is due to the formation of NH_3 fragments such as NH_2 in Si-rich SiN_x [3.24].

3.2.2.3 Elastic Recoil Detection Analysis

ERDA was conducted on the thin film samples deposited on c-Si substrate and was used to determine the total hydrogen content $[H]_{total}$ of the thin film [3.25]. The evolutionary changes to the hydrogen content of the thin films were tracked, serving as an indicator to the structural changes which may have occurred.

The $[H]_{total}$ and depth profiles were calculated from the experimental spectra with the help of SIMNRA® [3.26] computer software which uses an iterative process to fit the experimental data with the user input. A theoretical model which represents the physical structure of the thin film is constructed consisting of layers with varying thicknesses each containing the ratios in which constituent atoms are bonded. The surface of the thin film is detected on the high energy side of the spectra, where the impinging ion beam contains all of its energy, and loses energy after each interaction through the depth of the thin film.

UNIVERSITY of the
WESTERN CAPE

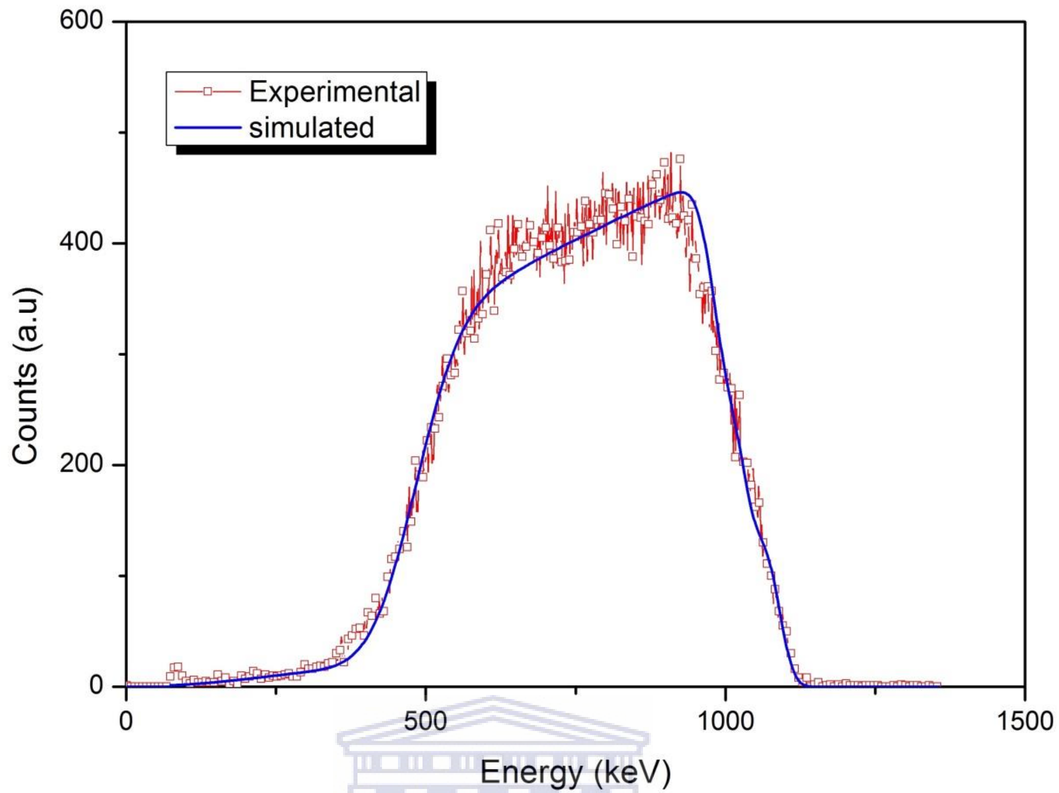

Figure 3.6: A representative ERDA spectrum showing the experimental data and the simulated fit.

UNIVERSITY of the
WESTERN CAPE

Figure 3.6 is a representative of one of the series showing the experimental data as well as the simulated fits. The total hydrogen content is calculated as a weighted average of the overall theoretical thickness and the hydrogen content in each layer such that:

$$[H]_{total} = \sum_{i=1}^{n} \frac{x_i H_i}{X_n} \qquad (3.2)$$

where x_i is the theoretical layer thickness, H_i is the hydrogen content of the layer and X_n is the total theoretical thickness of the thin film as calculated by SIMNRA in units of 1 x 10^{15} at/cm^2.

The as-deposited thin films were calculated to have a fractional concentration of hydrogen of 9.0 at. % for both sets of samples, MW304 and MW303. During the annealing treatment at temperatures below 400°C no significant change in the hydrogen content was observed. After exposing the thin films to a temperature of

400°C the fractional concentration of hydrogen decreased to 5.0 and 6.0 at. % for MW304 and MW303 respectively. The thin film belonging to MW303 delaminated after exposure to temperatures exceeding 600°C, while the films of MW304 remained intact. At 600°C MW304 had a hydrogen concentration of 2 at. %, and after annealing at 1000°C only surface hydrogen was detected with a total hydrogen concentration of 0.3 at. %.

UNIVERSITY of the
WESTERN CAPE

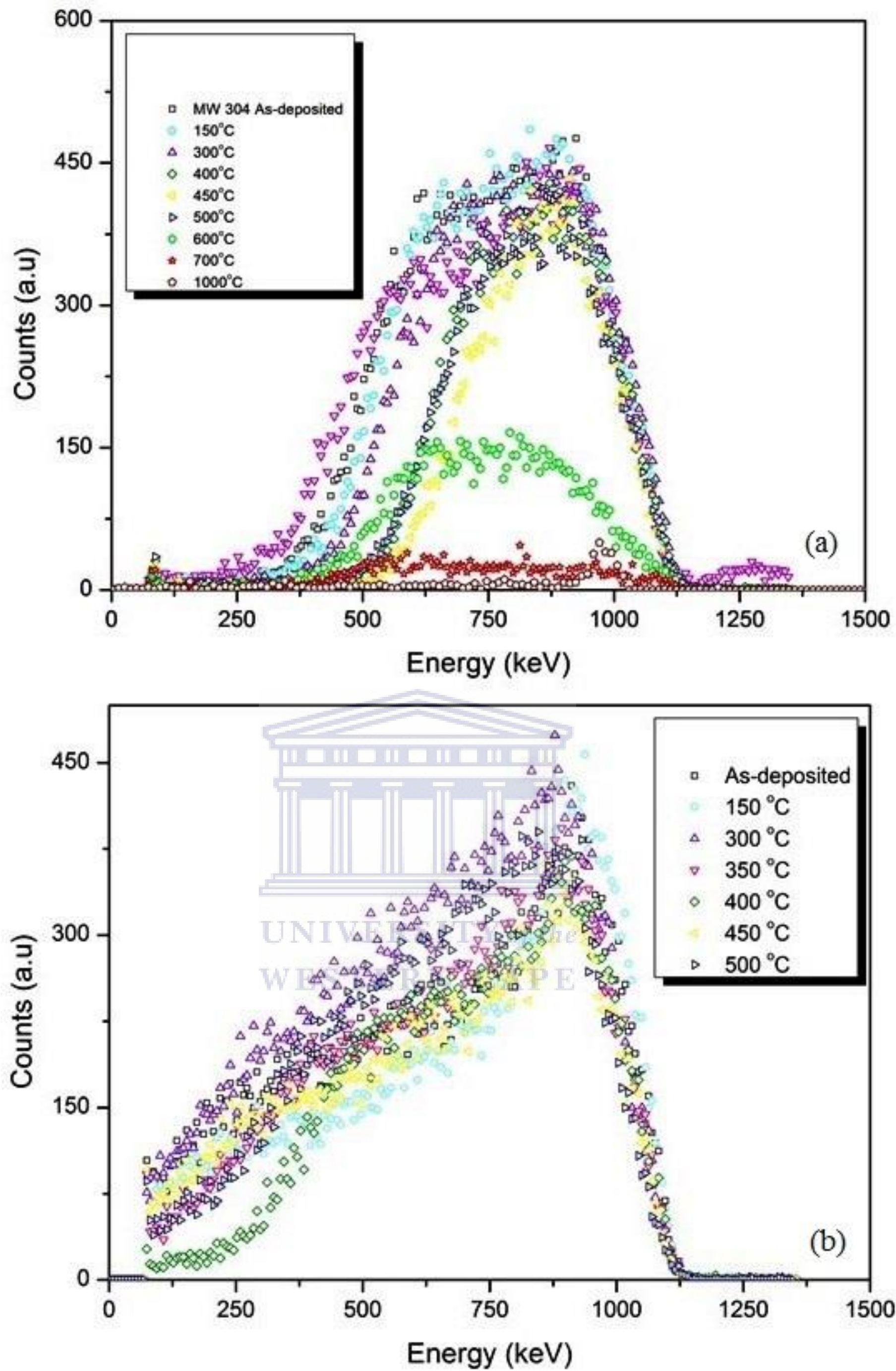

Figure 3.7: ERDA spectra (a) MW 304 and (b) MW 303 displaying changes in hydrogen content with increasing annealing temperature.

Figure 3.7 (a) displays the changes in hydrogen concentration for MW 304 between the as-deposited and the annealed samples at every temperature. For the temperatures ranging between 150°C and 500°C no change in the surface

hydrogen was detected, and only hydrogen located in the bulk of the thin film showed a decrease. This can be linked to the changes observed in the FTIR 2100 cm^{-1} mode on the same temperature range as displayed in figure 3.5 (a). The changes observed are characteristic of structural rearrangement taking place deep in the bulk of the thin film. A change to the overall hydrogen content was only observed at temperatures above 500°C, with a sharp decrease in the amount of hydrogen being detected, and a similar trend is observed in the 2100 cm^{-1} mode of the FTIR of figure 3.5 (a). After being exposed to 1000°C only trace amounts of hydrogen is detected on the high energy end of the spectra indicating a total depletion of the hydrogen previously detected in the bulk, leaving behind only surface hydrogen.

UNIVERSITY of the
WESTERN CAPE

A similar trend is observed for MW 303 as observed with MW 304 for low temperatures, an overall decrease in total hydrogen content with an increase in annealing temperature. For annealing temperatures between 150°C and 250°C no significant change had occurred to the bonding configuration in figure 3.5 (b) in the FTIR section, which correlates well with the ERD analysis. Figure 3.7 (b) shows a decrease in hydrogen content for the sample annealed at 400°C, in comparison to the 2100 cm^{-1} mode in figure 5 (b) which displayed an increase at the same annealing temperature. For the thin films the opposite trend observed for the same temperature can be explained by the fact that a positive result in the FTIR difference spectra shows an increase in bonding configuration quantity, and not the formation of hydrogen, whereas a decrease observed in ERDA is an indication of hydrogen migration and loss due to the elevated temperatures. A

reduction in hydrogen content is expected from the ERDA spectra as diffusion of hydrogen occur as the annealing temperature increases [3.27; 3.28].

3.2.3 Surface Characteristics

3.2.3.1 Introduction

The determination of surface characteristics of thin films used for optical applications is important. Changes in the topography landscape of the thin film may influence the scattering of light off the surface. For use as an anti-reflective coating on solar cells wide angle scattering could diminish the amount of useful light being transmitted to the active layer, thus adversely affecting the efficiency of the solar cell. In this section the results of two surface techniques, AFM and HRSEM, are discussed. The measurements were performed on samples which were deposited on the c-Si substrates.

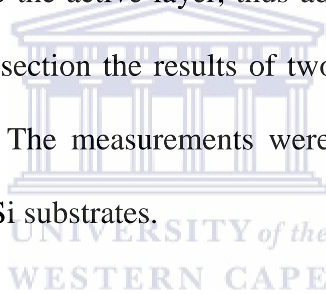

UNIVERSITY of the
WESTERN CAPE

3.2.3.2 Atomic Force Microscopy

The Root Mean Square (RMS) roughness was chosen to characterise the overall roughness of the as-deposited and annealed thin films due to its sensitivity to peaks and valleys compared to the average roughness [3.29] as defined in Chapter two.

The overall surface appearance of the as-deposited thin films belonging to MW 304 appeared to be smoother and uniform when comparing it to the as-deposited thin film set of MW 303. Figure 3.8 (a) and (b) below depicts the three dimensional view of the as deposited thin films. The values describing the roughness of the thin films were determined using Nanoscope 7.3 ® software, and the images were obtained from WSXM software [3.30] after the flattening

correction was applied. The flattening correction is necessary to calculate peak heights in instances where the substrate may be curved as a consequence of processing such as annealing.

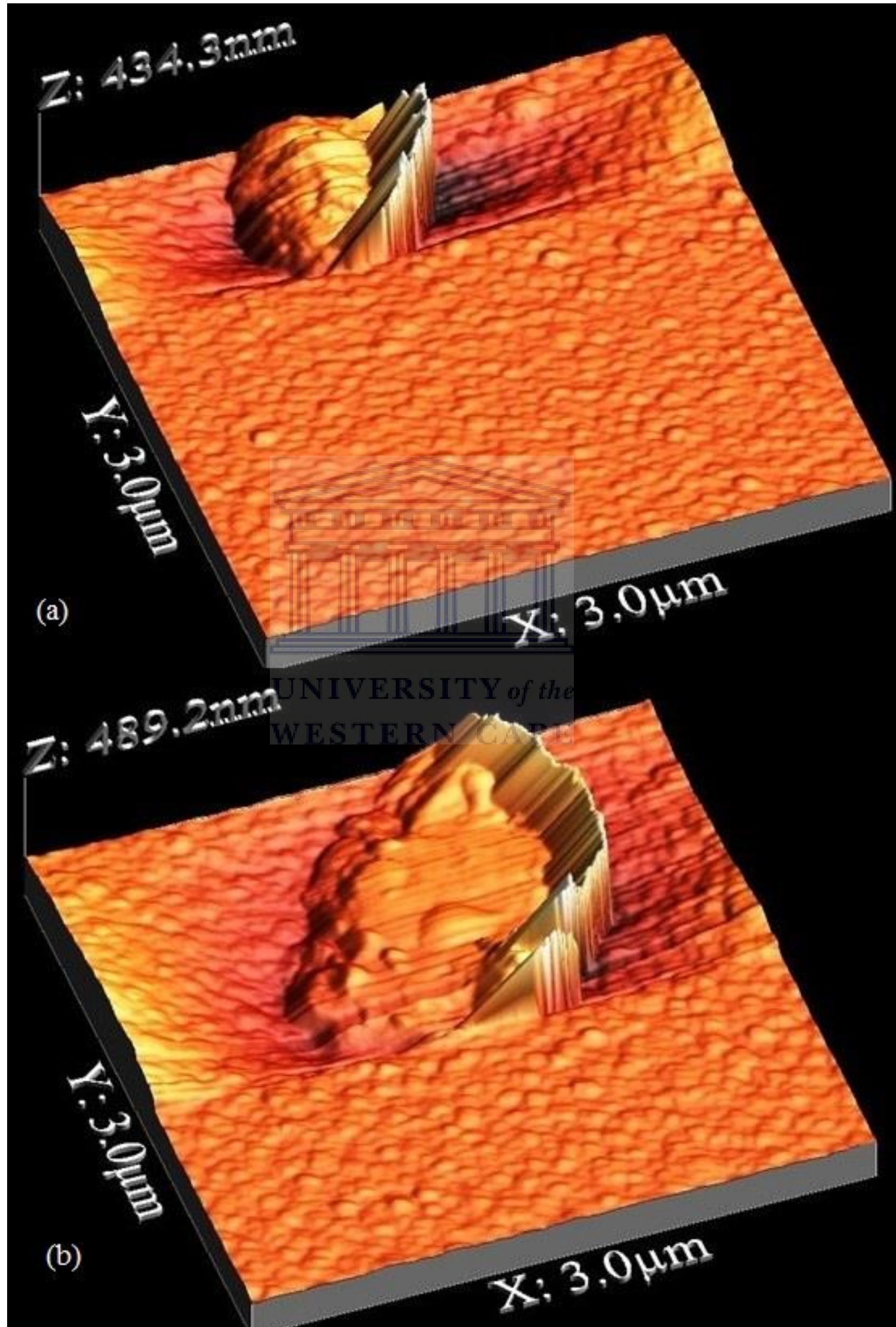

UNIVERSITY of the
WESTERN CAPE

Figure 3.8: (a) 3-Dimensional AFM image of the as-deposited thin films of (a) MW 304 and (b) MW 303.

Figure 3.8 (a) and (b) both shows large protrusions on the as-deposited sample while other regions appear to be flatter. The protrusions are caused by defects due to growth process and thicknesses effects [3.31], and form lower than the average level of the thin film and protrude from a valley-like structure.

The RMS roughness and the associated error values for the as-deposited thin films were calculated by selecting five areas, each of one square micron, across the surface of the thin film using the Nanoscope 7.3 ® software. The large protrusions seen in figure 3.8 influences the roughness values determined as they are not uniform in height; the area surrounding the tower structure are lower compared to the mean surface level of the thin film giving the effect of roughness. The fact that the as-deposited thin films are not homogenous in thickness due to the position of the substrate in the deposition chamber in relation to the hot wire, and the fact that the thin film measured in each set does not originate from the same area on the substrate causes a disparity in the measured roughness values.

UNIVERSITY of the
WESTERN CAPE

MW 303 contains a reduced N/Si ratio compared to that of MW 304. The variations in bonding quantities in the as-deposited samples for the two sets contribute to the surface characteristics [3.19], as the N/Si ratio increases due to an increase in the flow of NH_3 the stress experienced by the thin film changes from compressive to tensile thus indicating the rearrangement of the Si-N network [3.32]. The Si-N bond lengths are shortened, thus resulting in the contraction of the thin film. A consequence of an increase in NH_3 flow is an increase in concentration of atomic hydrogen in the deposition chamber. The new elevated level of atomic hydrogen promotes the deposition of smoother surfaces [3.32].

The roughness values for MW 304 and MW 303 as-deposited thin films are displayed in the table 3.2 below. The associated errors displayed are comparative in magnitude to the calculated roughness value, which does not make physical sense. The large uncertainty in the value is due to effects from the protrusion as described above.

Table 3.2: As-deposited roughness values for MW 304 and MW 303.

As-deposited Roughness (nm)	
MW 304	**MW 303**
9.54 ± 9.22	25.73 ± 26.98

UNIVERSITY of the WESTERN CAPE

An overall decrease in the RMS roughness is observed with an increase in annealing temperature for both series, with the roughness of MW 303 remaining higher than that of MW 304. The decrease in roughness can be linked to the structural rearrangement of the bonding network, with increasing annealing temperature. Since the AFM measurements were performed on the thin films deposited onto Si substrates and the MW 303 thin films on these substrates were not stable at high annealing temperatures, no roughness values were obtained for the thin films annealed at temperatures higher than 500°C.

At 300°C many more protrusions are visible over the surface of the annealed thin film for both series as displayed in figure 3.9 (a) and (b). These protrusions are smaller and sharper compared to those observed on the as-deposited samples. In figure 3.9 (a) depicting MW 304 the protrusions are scattered with regions of uniform smoothness around it and a roughness of 2.40 ± 0.26 nm was calculated. Figure 3.9 (b) shows clusters of protrusions appearing in the top corner and

stretching along the edge of MW 303 a RMS roughness of 4.30 ± 0.81 nm was calculated for the thin film surface.

Annealing the thin films at 500°C further reduced the size and frequency of the protrusions on the surface of the thin films as observed in figure 3.10 (a) and (b) respectively. The roughness for each thin film was calculated to be 2.24 ± 0.24 nm and 3.03 ± 0.06 nm for MW 304 and MW 303 respectively.

UNIVERSITY of the
WESTERN CAPE

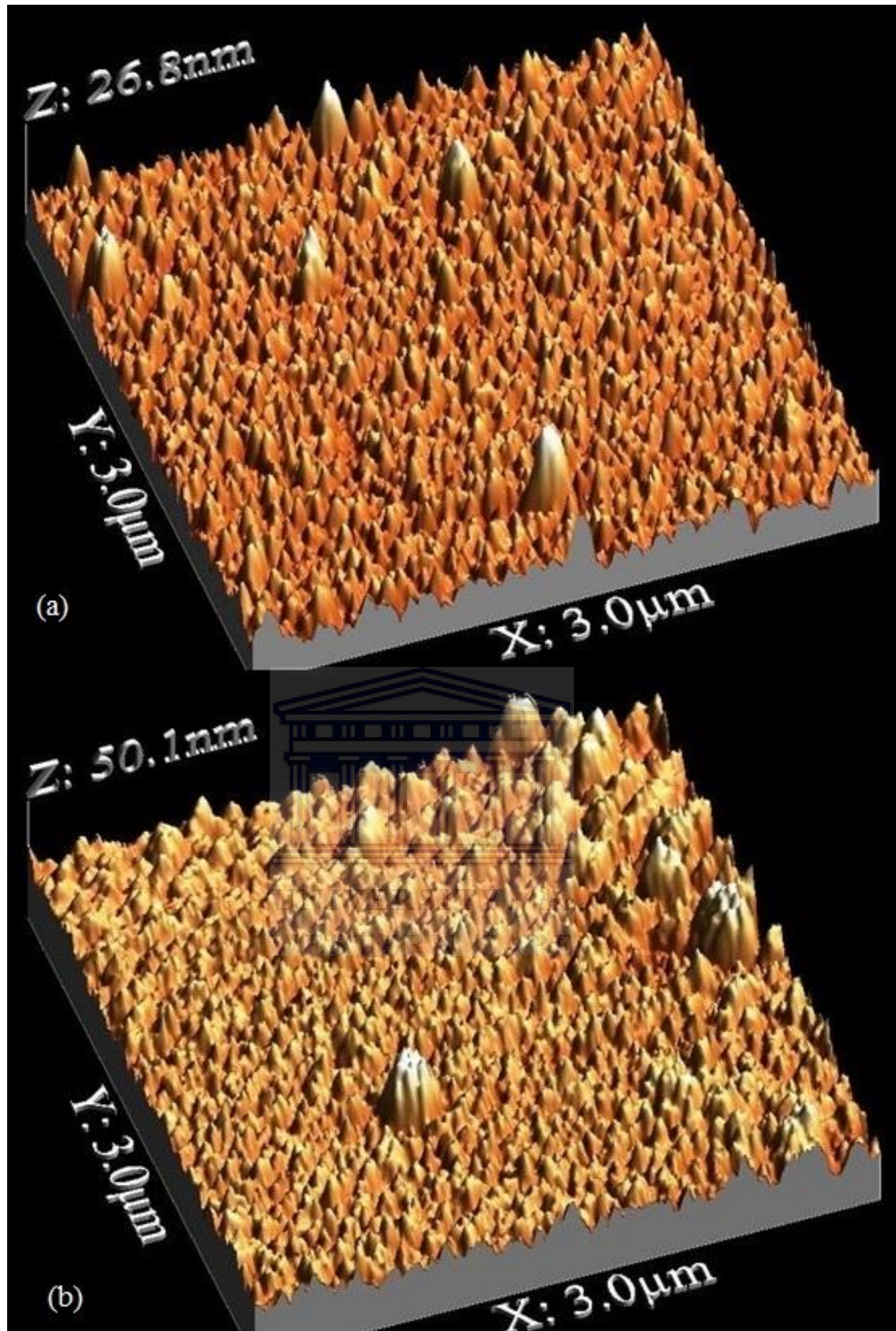

Figure 3.9: 3-Dimensional AFM image of (a) MW 304 and (b) MW 303 annealed at 300^{0}C.

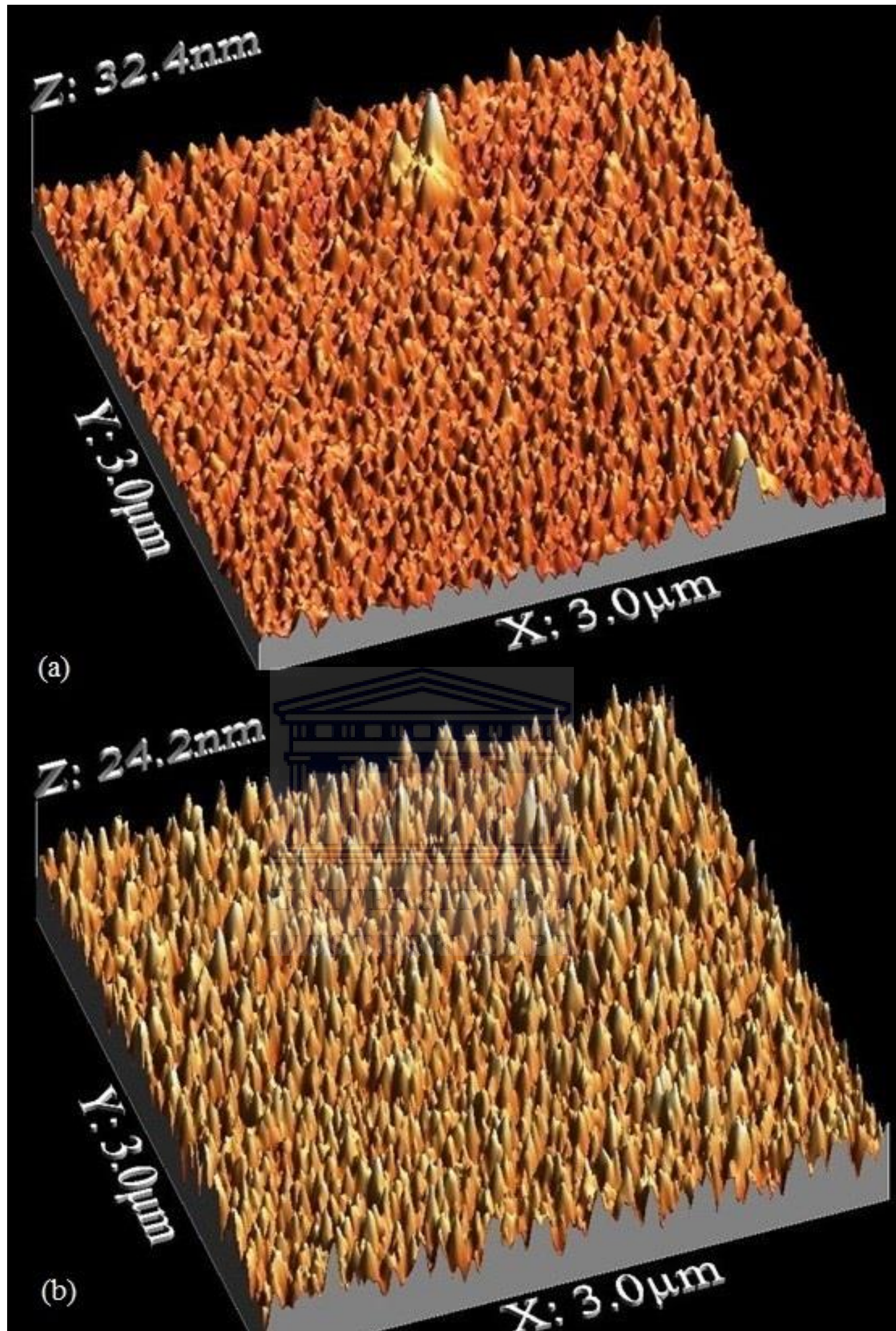

Figure 3.10: 3-Dimensional AFM image of (a) MW 304 and (b) MW 303 annealed at 500^{0}C.

At temperatures above 500°C two surface types can be discerned on the AFM images of MW 304 shown in figure 3.11. The first type of surface as depicted by figure 3.11 (a) shows a porous and blistered surface. This was most likely caused by rapidly escaping gas trapped under the surface and bursting through, thereby

scarring the surface. The second type of surface detected, illustrated in figure 3.11 (b), was unscarred and uniform, containing the usual surface features. This confirms the inhomogeneity within the thin film, including an uneven distribution of trapped gas.

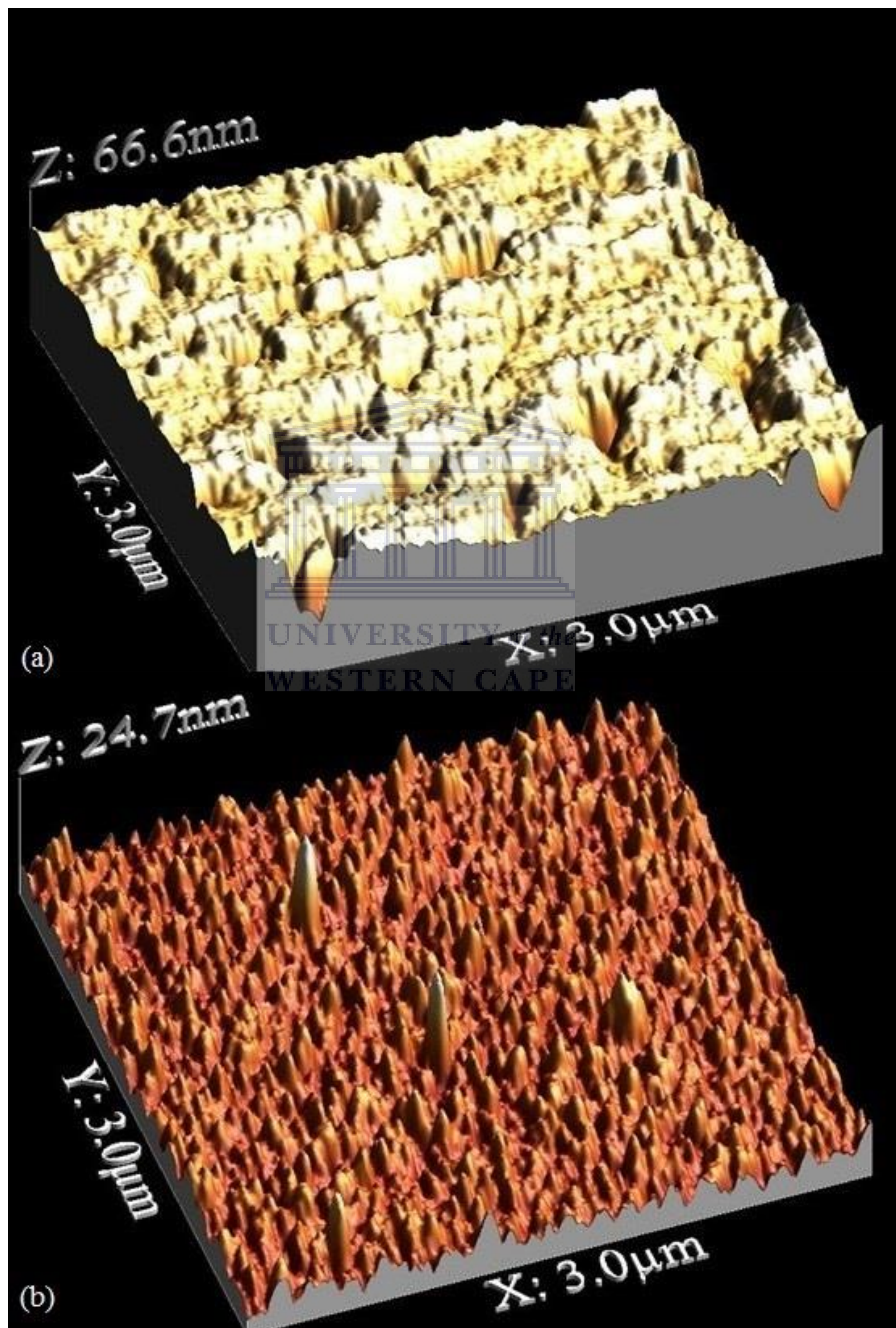

Figure 3.11: 3-Dimensional AFM image of MW 304 for (a) blistered surface region and (b) smooth surface region for films annealed at 1000°C.

The RMS roughness for each surface was calculated; figure 3.11 (a) and (b) has an RMS roughness of 4.74 ± 1.08 nm and 1.93 ± 0.19 nm respectively.

3.2.3.3 High Resolution Scanning Electron Microscopy

High resolution scanning electron microscopy (HRSEM) was conducted on the thin films deposited on silicon substrates which were coated with a silver paste to prevent charging effects. HRSEM was conducted to track the evolutionary changes of the surface features due to exposure to high temperatures and to confirm the trends observed with AFM.

Due to the delamination at high annealing temperatures of the thin films belonging to MW 303, the HRSEM measurements were only conducted on MW 304. Measurements were performed on the as-deposited thin films as well as films exposed to 1000°C.

Results observed are similar to that obtained by AFM. The protrusions are seen in greater detail with HRSEM when greater magnifications are used as shown in figure 3.12. The area around the protrusion appears darker than in the AFM; this is interpreted as an area which is recessed below the surface, and can be clearly detected by the HRSEM.

UNIVERSITY of the
WESTERN CAPE

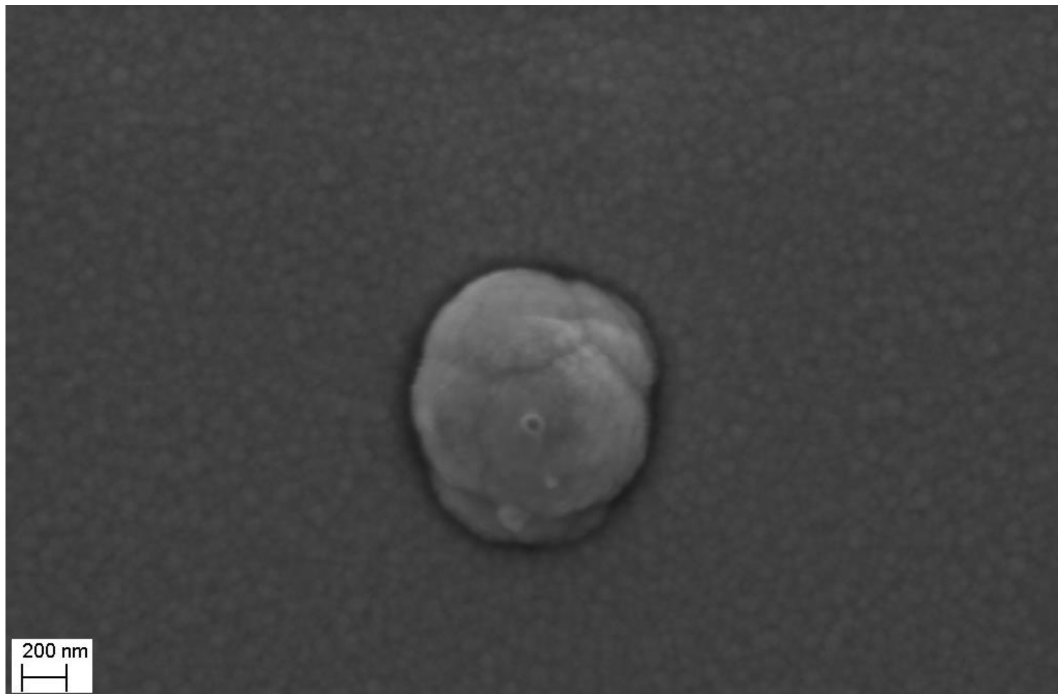

Figure 3.12: HRSEM images of the as-deposited MW 304 thin film showing an isolated growth defect surrounded by a uniform surface.

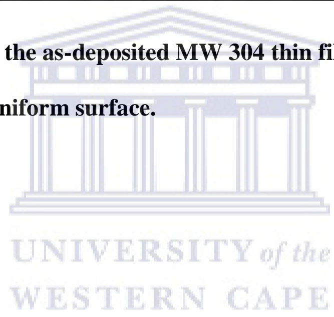
UNIVERSITY of the
WESTERN CAPE

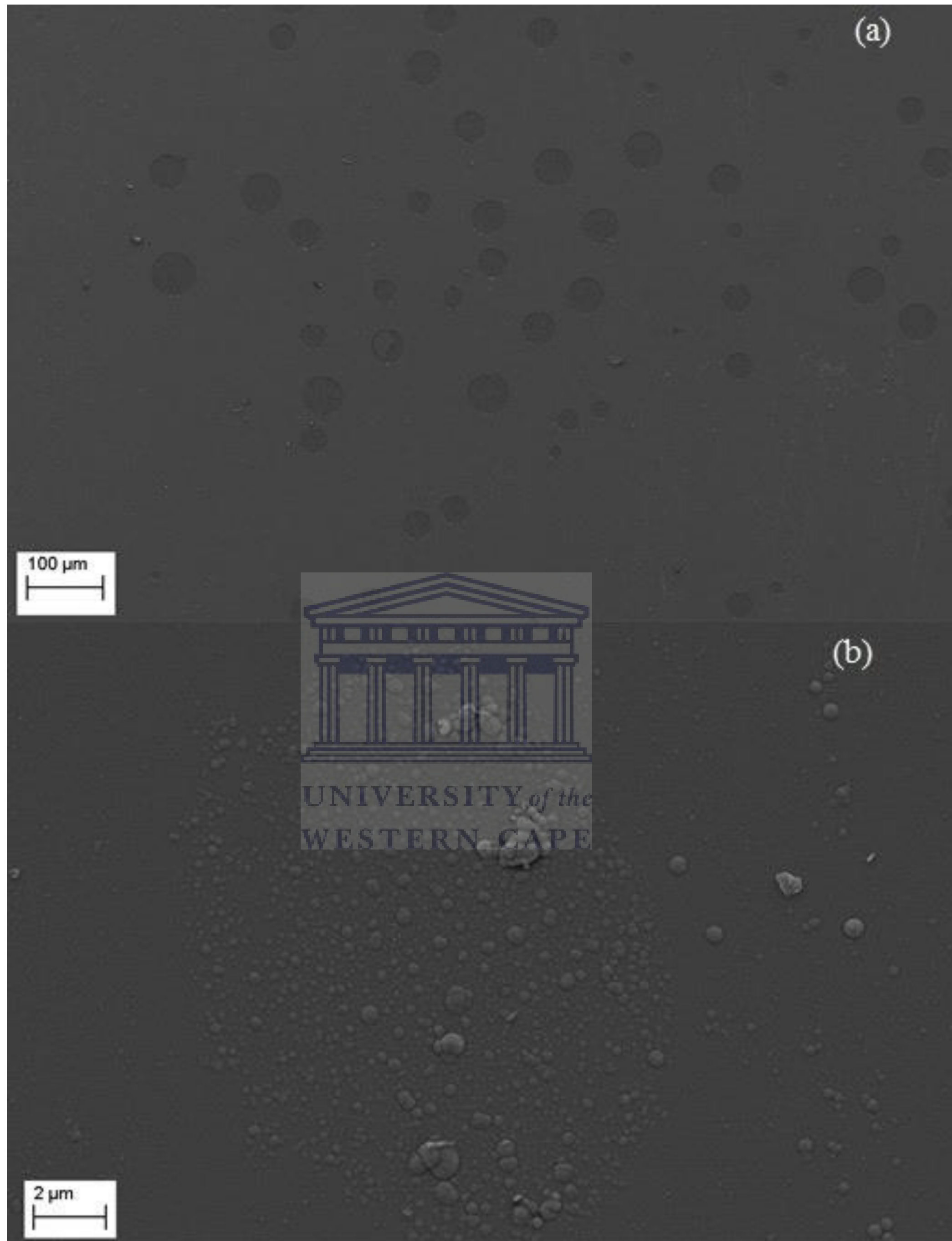

UNIVERSITY of the
WESTERN CAPE

Figure 3.13: HRSEM image of MW 304 annealed at 1000°C showing (a) blistered area and (b) area showing protrusions and uniform features.

Figure 3.13 (a) and figure 3.13 (b) shows the two regions identified on a sample of MW 304 annealed at 1000°C as described by AFM. The non-blistered surface

which remains intact after being exposed to high temperatures is littered with islands of protrusions. These protrusions seen in the HRSEM images serves as a representation of the surface features observed elsewhere on the thin film surface.

3.2.4 Optical Characteristics

3.2.4.1 Introduction

It is important to determine the changes in the optical properties of a material after exposure to high temperatures, especially since the material is intended for use in the PV industry as an antireflective coating on top of silicon solar cells.

As stated earlier, the conditions in the chamber during deposition influence the properties of the thin films. The optical properties of the thin film are directly related to the structure of the film, and hence the N/Si ratio will affect the overall optical properties of the thin film [3.33].

UNIVERSITY of the
WESTERN CAPE

The optical properties that will be discussed in the following section are the absorption coefficient, static refractive index (n_0), and the optical band gap ($E_{g\,(Tauc)}$). The Wemple–DiDomenico (WD) Model [3.34] will be discussed using parameters such as the single oscillator energy (E_0) and the dispersive energy (E_d) to describe the changes to the local bonding environment.

3.2.4.2 The Extraction of Optical Parameters

The optical properties of thin films can be calculated from optical transmission measurements performed on a transparent substrate as described by Swanepoel [3. 35] through the use of the envelope method. The method utilises rigorous calculations and manipulation of the formulae to describe the transmission of light through the thin film, as well as the fitting of envelopes to the fringes of the

transmission spectra as shown in figure 3.14 below. The optical properties, refractive index (n) and extinction coefficient (k) as well as the thickness of the thin film are calculated to an accuracy of better than 1%. Even though the inversion method offers high accuracy and is easy to use, this method assumes homogeneity throughout the thin film, which is not the case with SiN_x thin films. Another drawback of the Swanepoel method is the use of transmission measurements instead of reflection measurements. In general, it is preferred that optical spectroscopy of thin films deposited on thick absorbing substrates is performed in reflection mode rather than transmission mode, as the results yielded are far superior [3.36]. This allows for a mathematical model to be used to describe the DOS functions of the thin film material. The OJL [3.37] model is proficient in describing the dielectric function of any amorphous semiconducting material, and is capable of calculating the optical constants of measurements taken in either reflection or transmission mode.

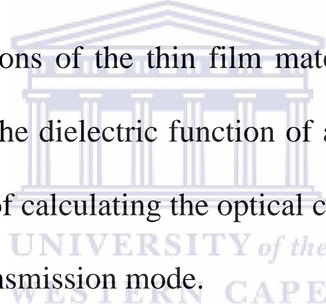
UNIVERSITY of the
WESTERN CAPE

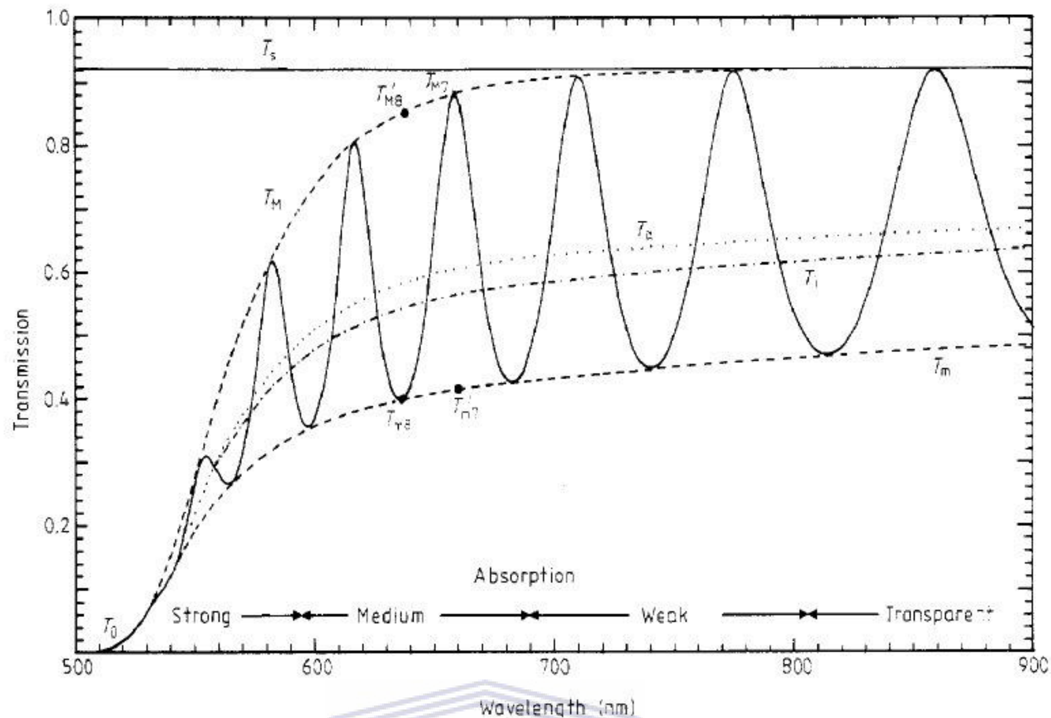

Figure 3.14: Simulated transmission spectra used in the calculations of the optical constants in the Swanepoel inversion method [3.33].

UNIVERSITY of the
WESTERN CAPE

The optical parameters were extracted from the resulting reflectance spectra with the help of Scout® software [3.38]. The optical model used not only employed the OJL empirical framework, but made use of the EMA theory to describe the complex material. The OJL model mathematically defines the shape of the valance and conduction bands DOS functions as a function of energy (E_0), which describes the band gap between the edge of the conduction and valence bands. The model explained in chapter 2 defines with the help of equation 2.85 and 2.86 a mass and gamma value which describes the shape of the DOS and the width of the exponential band tails respectively. The optical absorption is calculated using the joint DOS functions, calculated from the valence and conduction bands. The refractive index is calculated as a function of energy from the absorption coefficient and the Kramers–Kronig relation (KKR) [3.39].

The growth process of the thin film on the substrate is not only dependent on the position of the substrate in relation to the hot wire for the formation of a homogeneous layer, but is also dependent on the deposition conditions as described in Table 2.1 of Section 2.22. The variation in position and gas species causes compositional and thickness inhomogeneity to form in the thin film, making it difficult to describe the optical behaviour, and the use of a single model such as the OJL model become inadequate in describing the interaction of the light with the thin film. Figure 3.15 below shows the limitations of a single layer OJL model in fitting the reflectance spectrum of a-SiN_x:H, thus showing the need for more complex optical models.

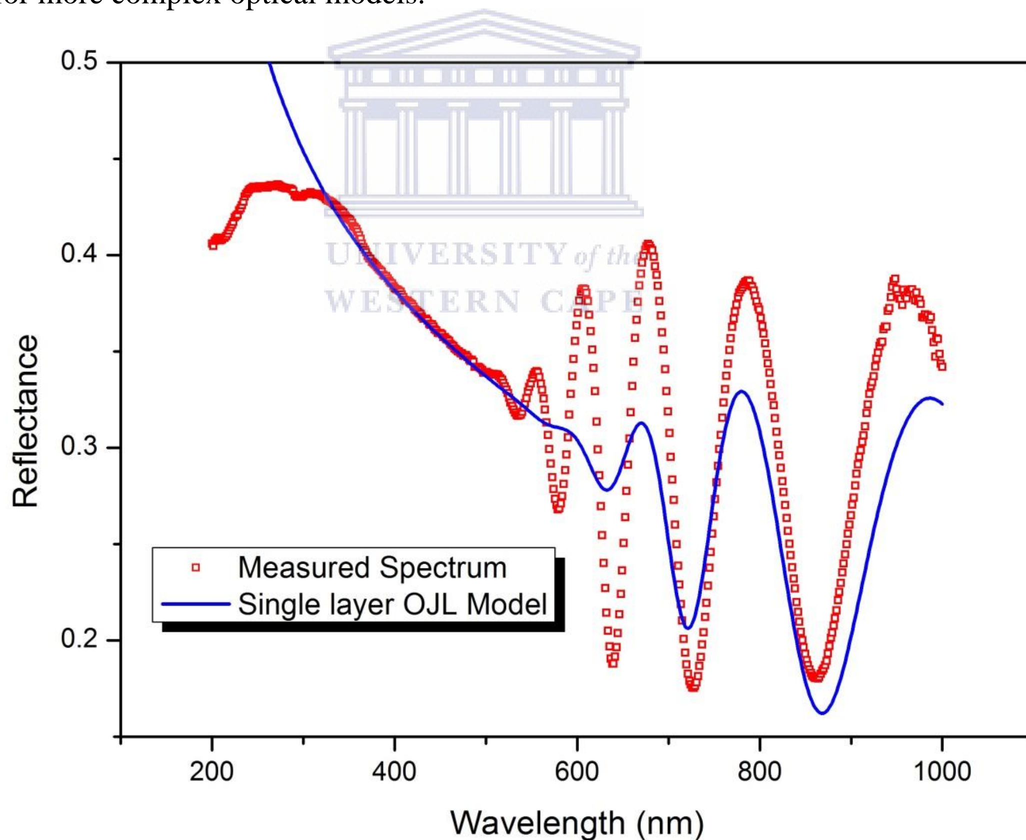

Figure 3.15: OJL model simulation of ineffective fit.

A Bruggermann Effective Medium Approximation (BEMA) [3.40] model was used to describe the heterogeneous nature of the material; this model consists of

the host material with particles embedded in it. Each material containing its own dielectric function and was treated as described in Chapter 2.

The BEMA utilized in the description of the thin film SiN_x material consisted of the following elements:

Table 3.3: A description of elements in the BEMA model.

	Matrix	**Particles**
(i)	OJL amorphous semiconductor	Si crystallites
(ii)	SiN mixture	SiN_x and Si_3N_4
(iii)	OJL amorphous semiconductor + Si crystallites	SiN mixture
(iv)	OJL amorphous semiconductor + Si crystallites + SiN mixture	Voids (air particles)

UNIVERSITY of the
WESTERN CAPE

The OJL model is capable of describing any homogeneous semiconductor; the SiN_x described in this study are not homogenous and therefore warrant the addition of particles such as crystallites, to describe regions in the material which may be very ordered, as well as air particles to describe voids which may have formed. The need for a mixture of stoichiometric and non-stoichiometric silicon

was used to steer the fits to a SiN-type material. A single layer BEMA model was shown to be ineffective as depicted in figure 3.16

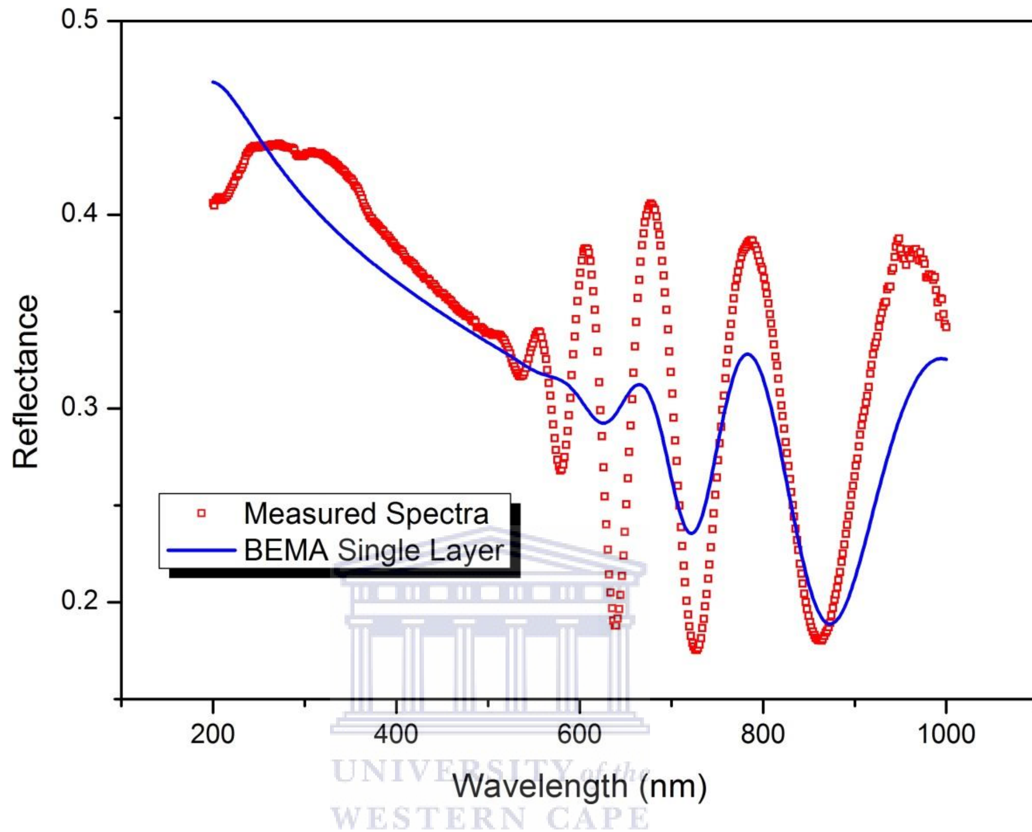

UNIVERSITY of the
WESTERN CAPE

Figure 3.16: Experimental Data with an inadequate single layer BEMA fit.

Hence a multi-layer stack [3.41, 3.42] containing the BEMA was created consisting of three layers of the BEMA as well as a fourth oxide layer on top, containing an EMA with the dielectric functions of SiONO-SiO_2 intermixed to describe post deposition oxidation which may have occurred. Each layer in the stack contained varying volume fractions of the host matrix and particulates which may be contained therein. Although it is a single thin film under investigation, the three layer stack describes a particular growth process which may have taken place during the deposition. The third layer constitutes an intermediate layer which formed on the substrate. This forms before any

preferential growth can take place. The middle or bulk layer is usually the thickest and contributes most of the overall optical properties to the thin film. The first layer represents the final growth process of the thin film, the settling of the radicals as the power was turned off to the hot wire. Post deposition oxidation is represented by the use of the oxide layer EMA, which describes the oxidation of all the constituents of the thin film. A surface representative schematic is depicted in figure 3.17 below.

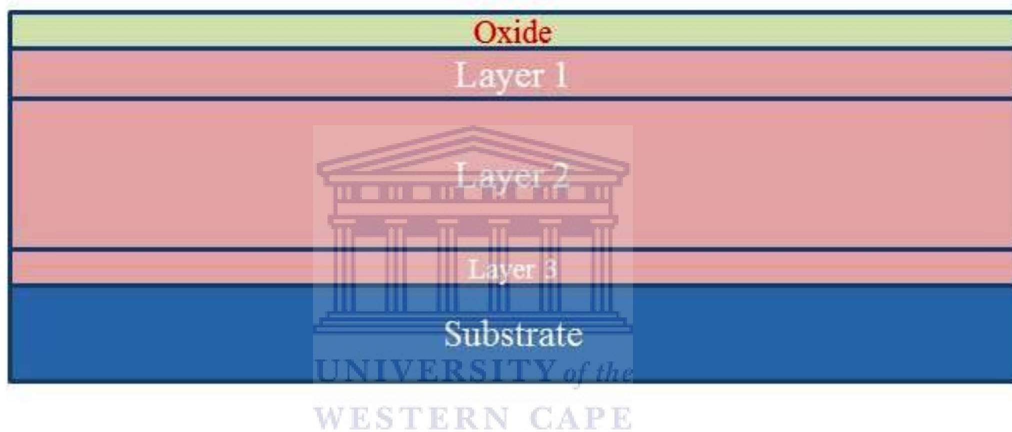

UNIVERSITY of the
WESTERN CAPE

Figure 3.17: A representative schematic of the layer stack, showing the three OJL-SiN mix plus the oxide layer.

In Scout ® the quality of the fit between the measured and the simulated spectrum is quantified with the fit deviation. The fit quality is described as follows [3.38]:

Table 3.4: Scout ® quality of fit rating system

Level	Deviation Threshold	Description
1	10^{-5}	Excellent
2	10^{-4}	Good
3	10^{-3}	Acceptable
4	10^{-2}	Bad
5	10^{-1}	Rejected

Excellent fits were achieved with the OJL plus EMA multi-layer models, with the OJL accounting for defect states and band tailing which may have occurred due to the disorder in the structure, as well as the interaction path of the light with the matter. The optical model is setup and tailored until the specific fitting parameters are achieved. The virtual multi-layer model can be used to describe both the worst case SR-SiN_x and the best case NR-SiN_x stoichiometric thin films in all facets. The absorption coefficient of the thin film was calculated as a weighted average from contribution of each layer in the stack using Beer's Law [3.43]:

$$\alpha_{total} = \sum_{i=1}^{n} \frac{\alpha_i \, x_i}{X_{total}}, \tag{3.3}$$

where α_i is the absorption coefficient in the ith layer, x_i is the thickness of the layer, and X_{total} is the total thickness of the thin film.

Figure 3.18 (a) and (b) depicts a fitted spectra as-deposited and annealed at 1000°C respectively. The deviation between the measured and simulated spectra for the as-deposited sample was calculated to be 1.54×10^{-4}, indicating an "acceptable fit". The deviation between the fit and the measured data for the annealed sample was found to be 1.87×10^{-5}, thus indicating a "good fit".

UNIVERSITY of the
WESTERN CAPE

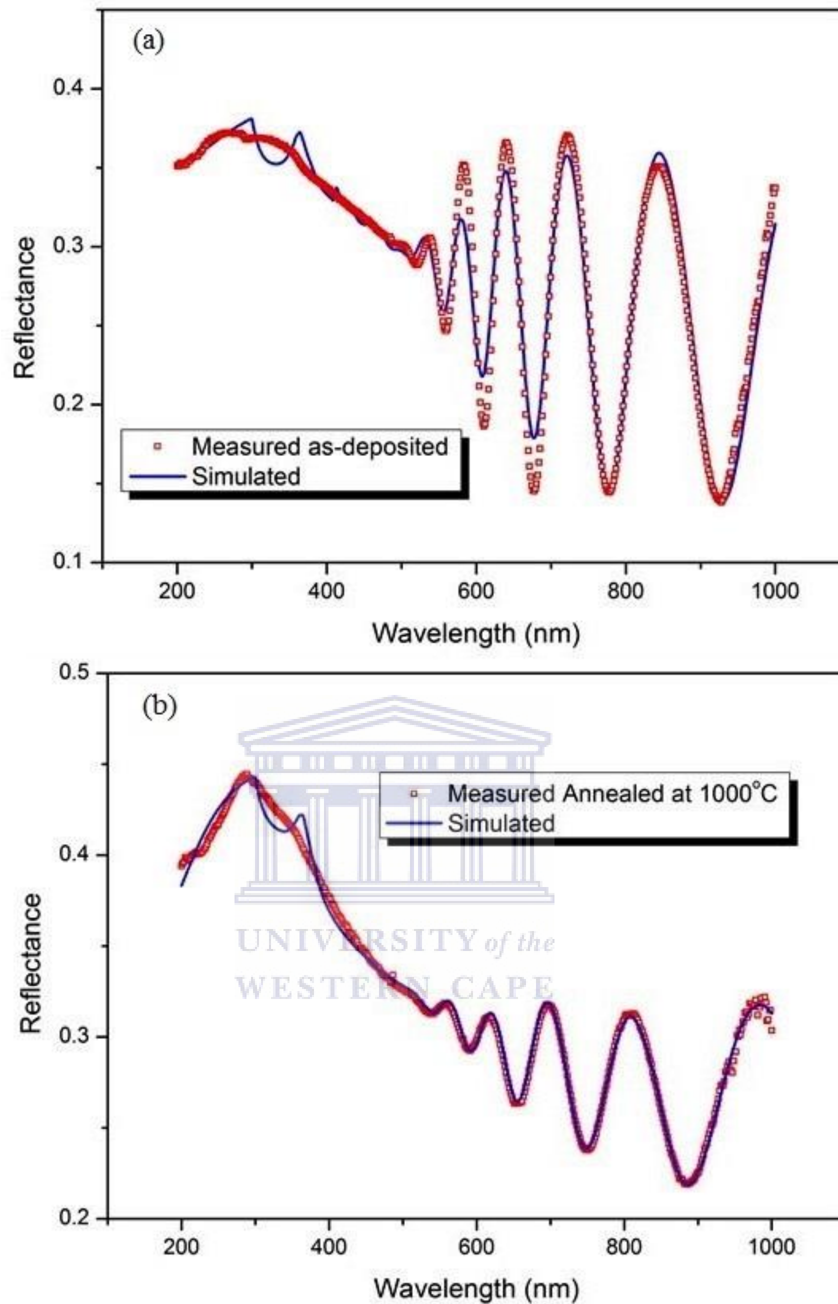

Figure 3.18: Fitting results for the multi-layered BEMA model for (a) as-deposited and (b) annealed.

3.2.4.3 The Optical Constants

The thickness of the thin films was determined through the use of interferometry as the interaction pathway of the light with the material. The thin film thickness is calculated as an average over the entire as-deposited sample for MW 303 and MW

304, and is calculated to be 1018 nm and 716 nm respectively. These thickness measurements are in close agreement with measurements taken on glass substrates and determined through optical transmission modelling. The variation in thicknesses of the two sets of thin films arises from the variation in the gas flux ratio (R = NH_3/SiH_4) of the two sets of depositions. During the deposition of MW 304, the ratio of NH_3/SiH_4 was higher compared to that of MW 303. The decrease in thickness with an increase in NH_3 arises due to an increase in atomic hydrogen during the deposition. The atomic hydrogen has an etching effect, removing weakly bonded silicides and incorporating nitrogen [3.31] thus decreasing the overall thickness. After annealing at high temperatures a decrease in thickness was observed due to the effusion of trapped gases in the underlying structures of the thin film [3.44].

UNIVERSITY of the
WESTERN CAPE

The dielectric response of a material is a consequence to an electromagnetic stimulus in the material, and is represented by a dielectric function. The dielectric function has both a real and imaginary part, which can be linked to the other optical responses such as refractive index, extinction coefficient and absorption coefficient of the material [3.45]. Considering only the real part (ε_1) of the dielectric function:

$$\varepsilon_1 = n^2 - k^2$$

and (3.4)

$$\alpha = \frac{4\pi k}{\lambda},$$

where n and k are the optical responses of the material, refractive index and extinction coefficient respectively.

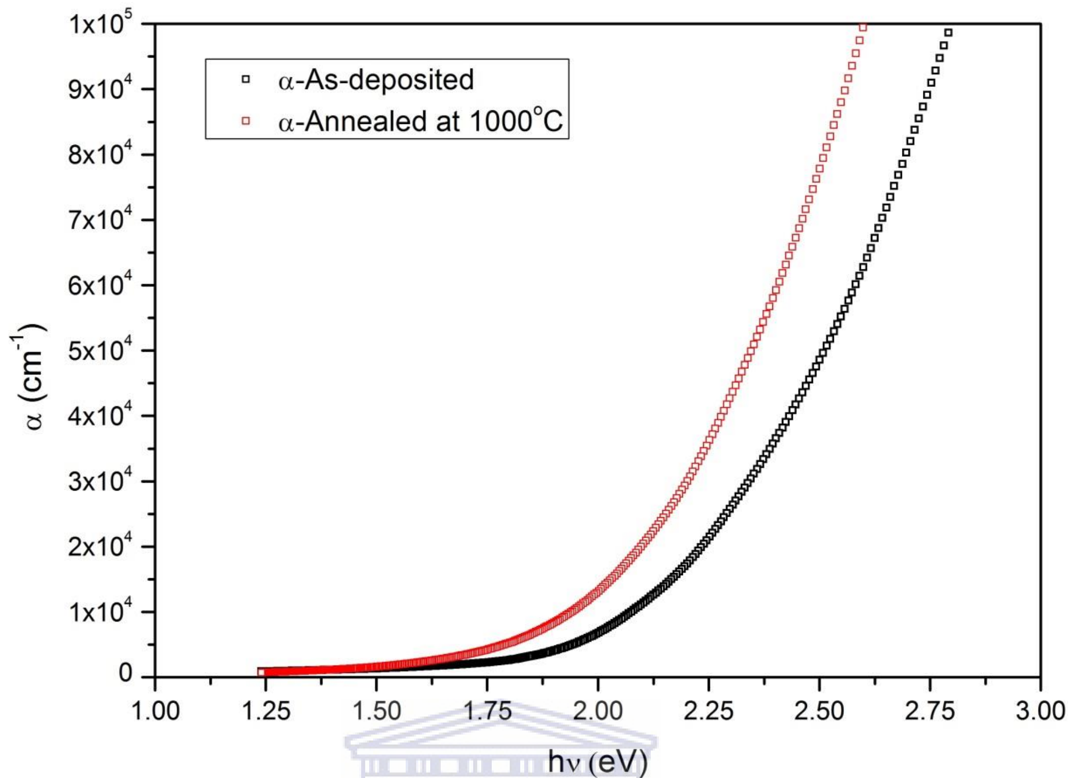

Figure 3.19: Absorption coefficient vs. energy curve for SiN_x as-deposited and annealed at 1000°C.

UNIVERSITY of the
WESTERN CAPE

An increase in absorption coefficient is observed for the SiN_x films, as the annealing temperature increases. Figure 3.19 displays a comparative plot of the absorption coefficient dispersion of an as-deposited sample with that of the highest annealing temperature. The increase in absorption is coupled with a decrease in optical band gap ($E_{g\ (Tauc)}$), which will be shown at a later stage in the section. From the plot it can be observed that a shift in absorption to lower energies occurs as the annealing temperature increases. The shifting to lower energies due to the structural rearrangement of weaker Si-N bonds forming more absorbing Si-Si bonds, coupled with the release of hydrogen as the annealing temperature is increased [3.17].

Molecules bonded together may be represented by harmonic oscillators representing the bonds between the atoms as described in Chapter 2. The

dielectric response of a material is due to the polarisation of the bonds as the EM stimulus interacts with the molecule [3.45]. If no polarisation occurs, the material will not have a dielectric response in that range of electromagnetic radiation. This may be observed when analysing ε_1 in the figure 3.20 below.

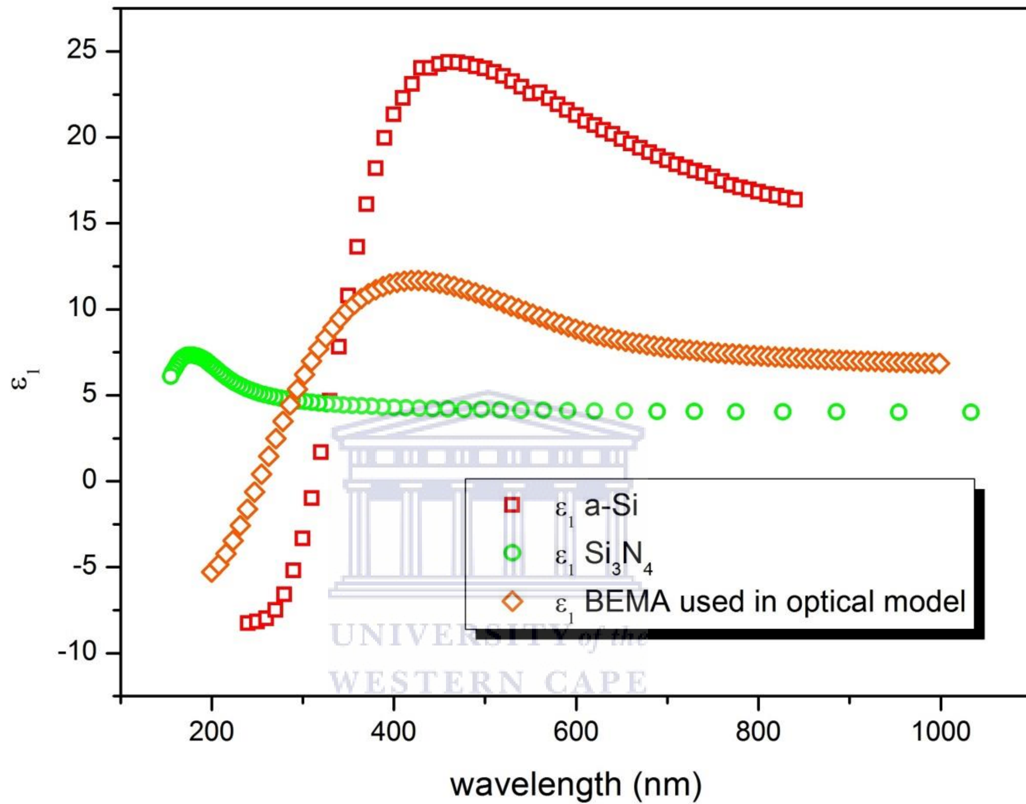

Figure 3.20: Dielectric dispersions of silicon and silicon alloys. The BEMA shown belongs to the bulk layer in the optical model constructed in section 3.2.4.2 [3.38].

Comparing the dielectric dispersions of Si_3N_4 in figure 3.20 to that of a-Si, no dielectric peaks are observed in the UV-visible region of the electromagnetic spectrum. On the contrary whilst comparing the effective dielectric function of the BEMA model used in describing the bulk optical parameters of the SiN_x thin films to that of the dielectric response of the a-Si, it can be noted that the two dielectric functions are similar in shape and have peaks at around similar wavelengths. The effective dielectric function of the BEMA contains an

amorphous host material, which may explain the simulative action observed. The resonance value of ε_1 is dependent on the composition of the silicon nitride, whether silicon-rich or nitrogen-rich thin films. For low values of x the resonance may appear sharp. As x increases the resonance peak is seen to broaden [3.46].

As explained above, the refractive index is related to the dielectric function by equation 3.4, although it is only showing the real part of the refractive index. The refractive index can be described as the ratio of the speed of light in a vacuum to the speed of light in a medium, where the medium is the thin film in question. The refractive index is dependent on the frequency of radiation, called dispersion. The refractive index dispersion is a response of the material to the electromagnetic stimulus, much like the dielectric function. The refractive index dispersion functions in figure 3.21 follow the same trends as the dielectric functions of figure 3.19. This result is expected as the two dispersion functions are related. In non-magnetic material the refractive index dispersion and the real part of the dielectric function as follows [3.45]:

$$n = (\varepsilon_1)^{1/2}, \quad (3.5)$$

which is directly derived from Maxwell's Equations.

UNIVERSITY of the WESTERN CAPE

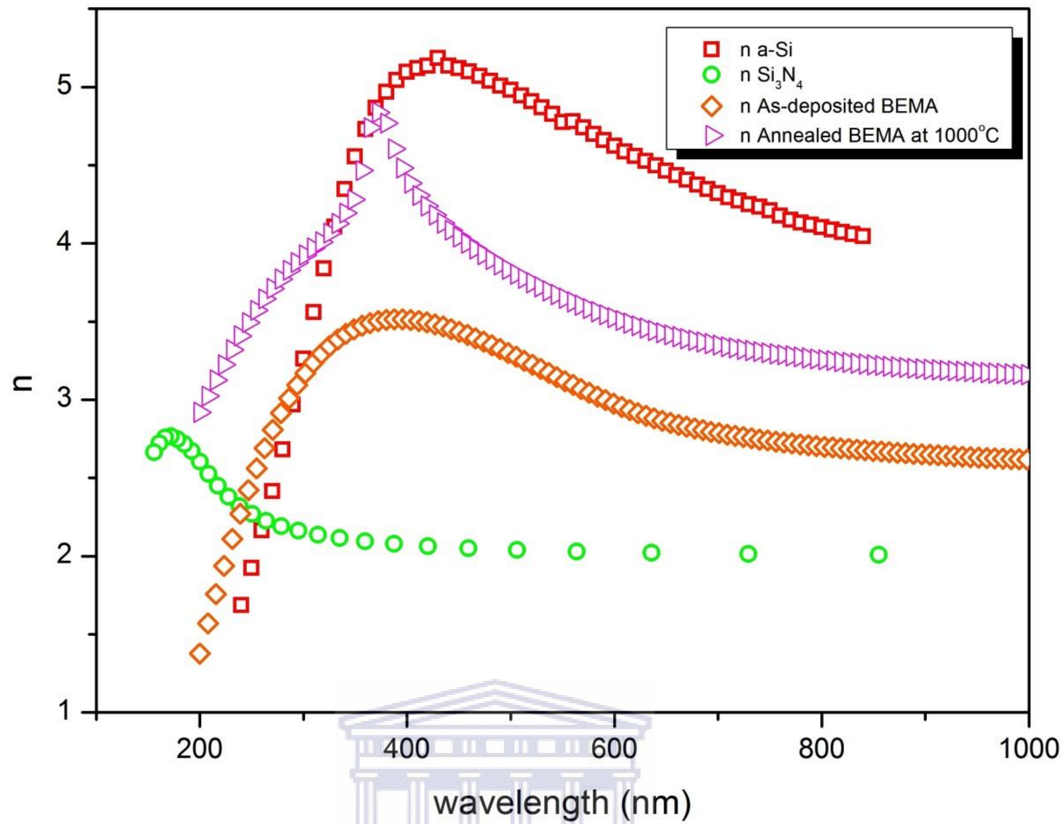

Figure 3.21: Refractive index dispersion of a-Si and silicon alloys [3.38].

UNIVERSITY of the
WESTERN CAPE

The refractive indices of a-Si and the as-deposited BEMA are similar to one another with regards to shape and behaviour in response to an electromagnetic stimulus. In Comparison the refractive index dispersion of the annealed BEMA displays a sharp resonance peak. The sharp resonance peak of the annealed dispersion and the broader resonance peak belonging to its as-deposited counterpart are observed to peak at the edge of the visible spectrum at around 400 nm.

The refractive index at infinite wavelength (n_0) of the as-deposited and annealed thin films were calculated by $1/(n^2-1)$ vs $(h\nu)^2$ using the single oscillator Wemple-DiDomenico (WD) model [3.44]. A straight line polynomial is then fitted to the data as shown in figure 3.22.

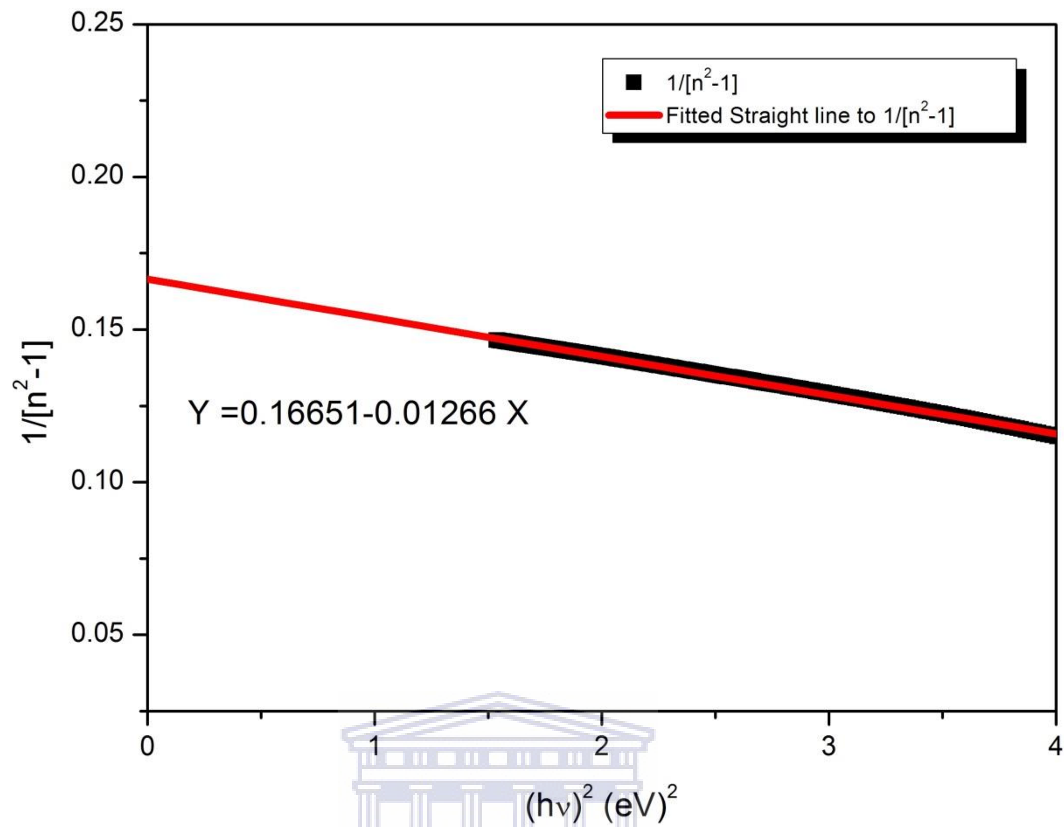

Figure 3.22: Typical plot of 1/(n^2-1) vs. (hv)^2 from the Wemple-DiDomenico model for the determination of n_0.

UNIVERSITY of the
WESTERN CAPE

The WD model can be used to describe the subgap refractive index behaviour, where the subgap is located mainly below that of $E_{g\ (Tauc)}$. The WD model can be expressed as [3.36]:

$$n(E) - 1 = {E_0 E_d}/{((E_0)^2 - (E)^2)}, \qquad (3.6)$$

where E_0 is the single oscillator energy, which reflects the difference in energy between the "centres of gravity" of the conduction and valence bands.

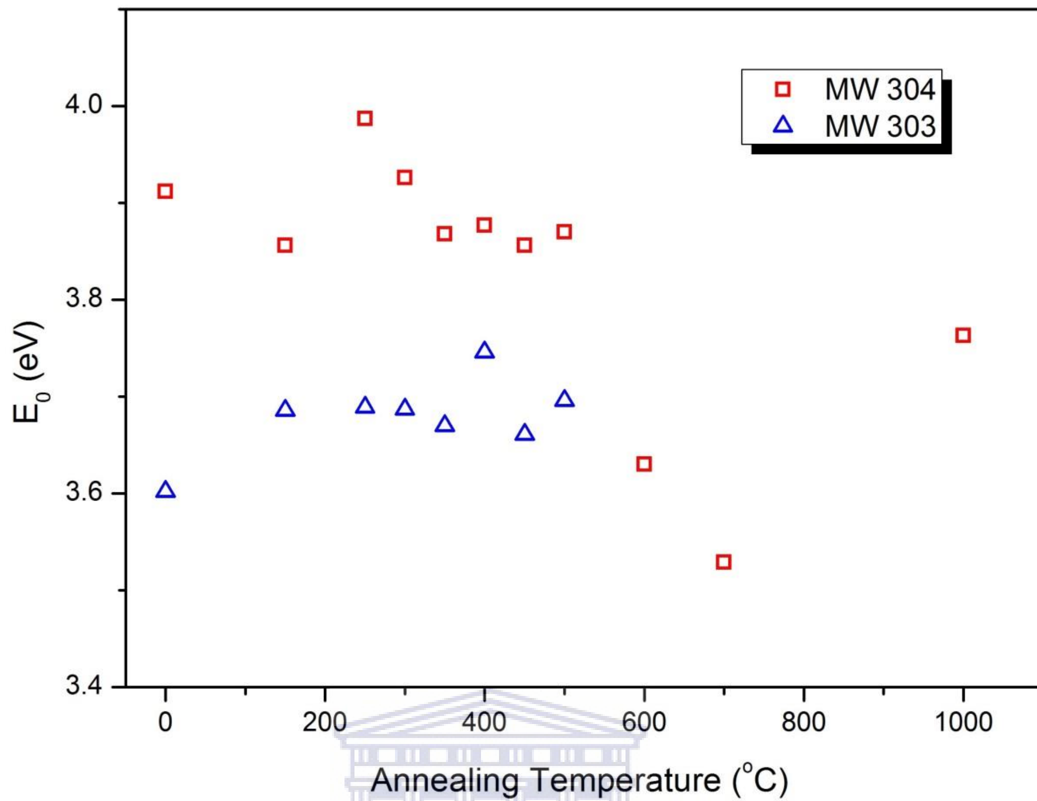

Figure 3.23: Progression of E_0 with increasing annealing temperature.

UNIVERSITY of the
WESTERN CAPE

The calculated value of E_0 is suggestive of an average band gap of the material. The calculated Tauc gap probes the optical properties near the fundamental band gap of the material, whereas the average gap calculated from the WD model provides quantitative information on the total band structure. E_d is the dispersion energy, and is a measure of the strength of the interband optical transitions. Figure 3.24 shows E_d vs. annealing temperature,

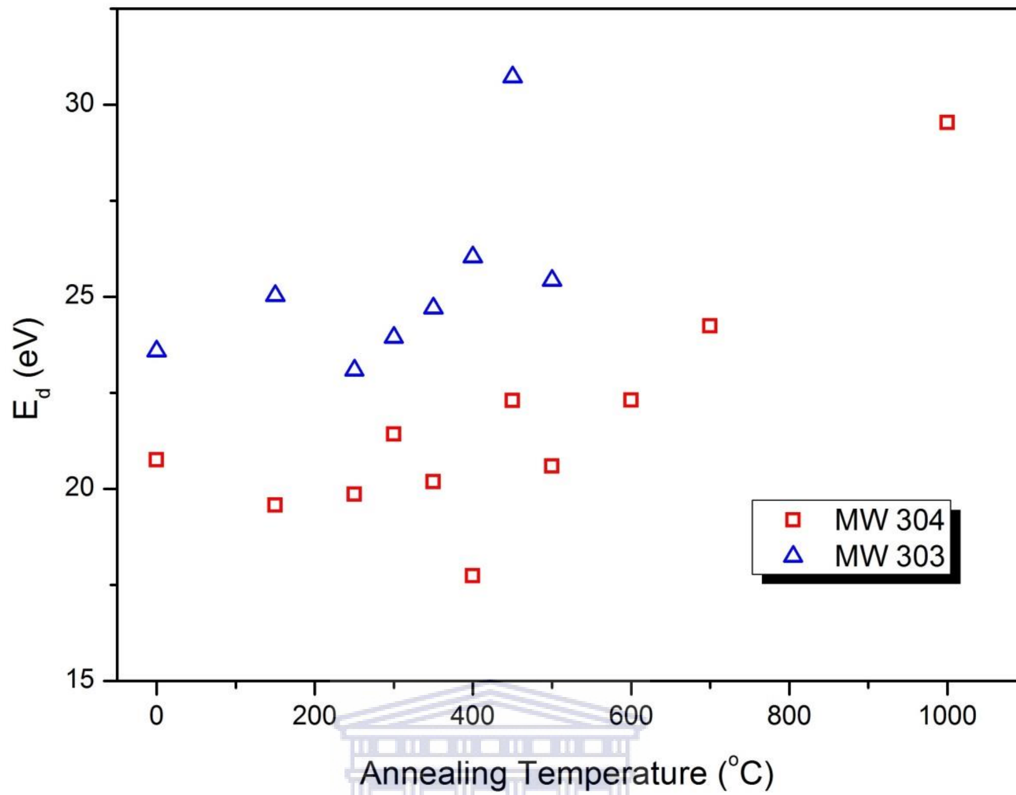

Figure 3.24: Progression of E_d with increasing annealing temperature.

UNIVERSITY of the
WESTERN CAPE

The value of E_d provides information mainly on the coordination number and mass density of the material. An overall insight on the microstructure of the material is gained from the use of these two parameters.

Table 3.5 below summarises the calculated as-deposited optical constants.

Table 3.5: Table of optical constants

	MW 303	**MW 304**	**Literature Values [3.36]**
n_0	2.75	2.50	-
$E_{g\ (Tauc)}$ (eV)	1.85	2.04	3.43
E_0 (eV)	3.60	3.91	7.85
E_d (eV)	23.59	20.75	27.1

Using the values from the fitted straight line, the static refractive index can be computed, along with the values of the variables found in equation 3.6.

The n_0 values of the as-deposited were calculated as an average value of the entire as-deposited sample. A disparity in refractive indices is observed between MW 303 and MW 304 as seen in Table 3.5 above. The large difference in refractive index is due to the varying nitrogen content in the films [3.6, 3.17]. The film containing the higher nitrogen content MW 304 has the lower refractive index, and a higher Tauc band gap. It is assumed that MW 304 has a higher density, and that the formation of N-H bonds in the thin should be higher [3.47]; although no appreciable quantity of N-H stretching vibrational bonds were observed in the FTIR of the as-deposited thin films.

After the annealing experiment, an increase in refractive index was observed with annealing temperature. The refractive indexes of both series are seen to be moving towards that of a-Si:H [3.21]. The increase in refractive index is observed when plotting the refractive index vs. annealing temperature as shown in figure 3.25. The increase in refractive index is as a consequence of the increase of polarisable bonds [3.23] which is observed at high temperatures through the use of FTIR measurements.

UNIVERSITY of the
WESTERN CAPE

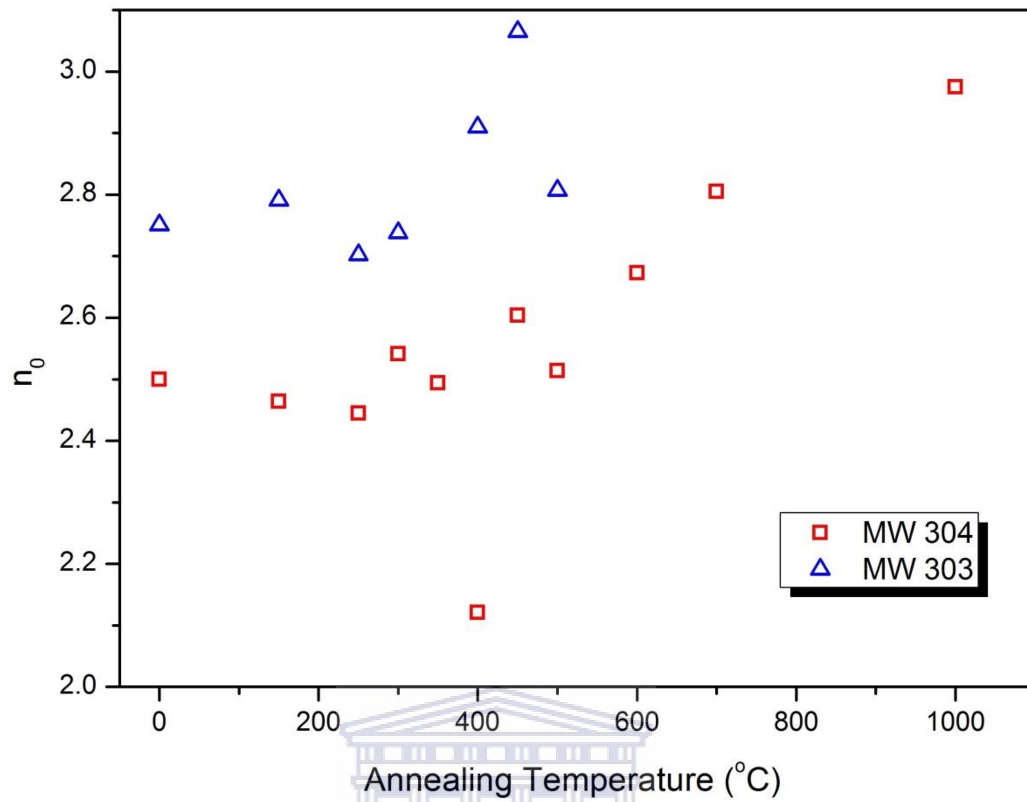

Figure 3.25: Progression of the static refractive index with annealing temperature.

UNIVERSITY of the
WESTERN CAPE

Furthermore the Tauc band gap ($E_{g\ (Tauc)}$) was calculated as explained in Chapter 2, and an average band gap was calculated for the as-deposited thin films and displayed in table 3.5. A plot of the Tauc band gap vs. annealing temperature is shown below.

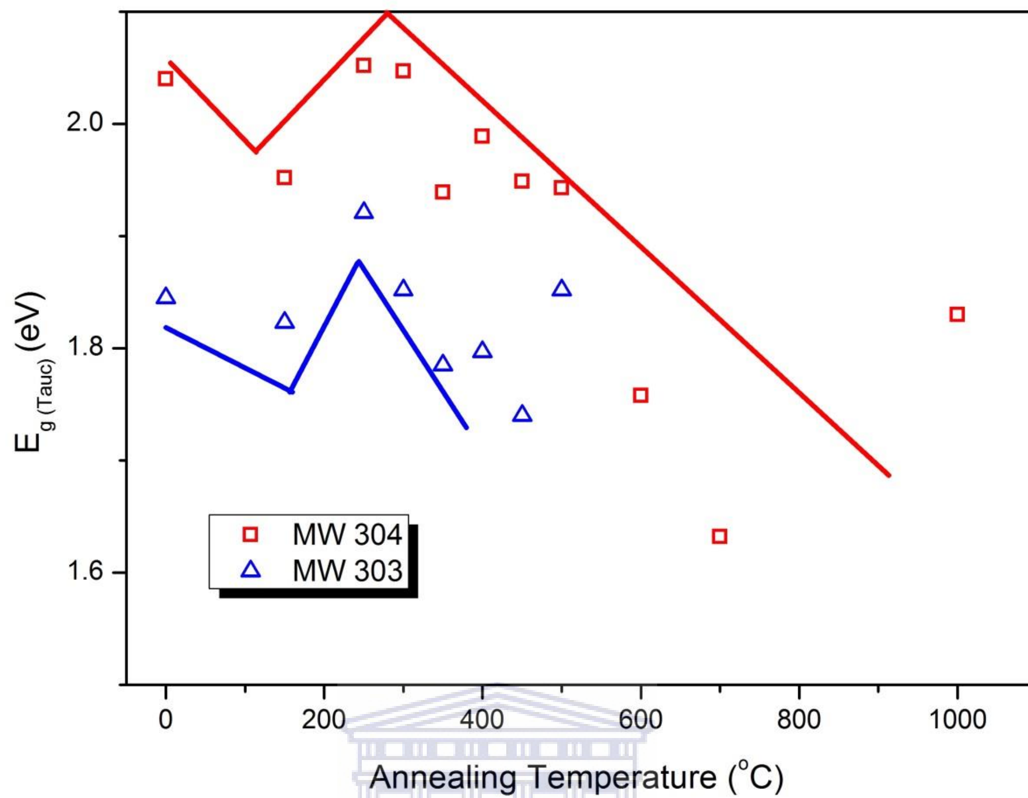

Figure 3.26: Progression of Tauc band gap with annealing temperature.

UNIVERSITY of the
WESTERN CAPE

A decrease in Tauc band gap is observed as the annealing temperature increases, as shown in figure 3.26, lines are drawn to assist in making the trend more apparent. The decrease in band gap is consistent with the thin films becoming more absorbent [3.17, 3.47]. It is difficult to establish an overall trend of the MW 303 series as the film delaminates at low annealing temperatures to moderate annealing temperature, as observed in figure 3.26. Martínez *et al*. [3.48] have noted that replacing Si-Si bond with Si-H bonds leads to an increase in $E_{g\ (Tauc)}$, equally during annealing the loss of Si-H bonds are replaced by the more absorbing Si-Si bonds thus decreasing the $E_{g\ (Tauc)}$ and increasing the absorption coefficient.

Thin films with a higher refractive experience lower losses in reflection, but at the same time the thin films become more absorbent [3.49], which can be observed for both as-deposited series as annealing temperature increases.

Similar trends are observed with the WD parameters, E_0 and E_d, compared to the $E_{g\ (Tauc)}$ as the annealing temperature increases. As the annealing temperature increases a decrease is observed in both E_0 and E_d as seen in figures 3.25 and 3.26 respectively. For MW 303 this trend is not obvious at first glance, as there are not as many data points as in MW 304.

A deeper understanding of the a-SiN_x microstructure is offered by E_d, which was obtained from the refractive index dispersion for the single oscillator model. The WD model was extensively used in describing the empirical relationship of the coordination number of the cation nearest neighbour to the anion; this was conducted on a variety of ionic, covalent and liquid samples. E_d can be expressed as [3.36]:

UNIVERSITY of the
WESTERN CAPE

$$E_d = \beta N_c Z_a N_e, \tag{3.7}$$

where β, Z_a, and N_e are constants specific to the material, and N_c the coordination number. The WD model was extended to describe amorphous materials such that

$$\frac{E_d{}^a}{E_d{}^b} = \left(\frac{\rho^a}{\rho^b}\right)\left(\frac{N_c{}^a}{N_c{}^b}\right), \tag{3.8}$$

where a and b refers to the amorphous and crystalline form respectively. In an amorphous material E_d provides information and insight on the density and coordination number of the material.

Analysis performed on the TO peak belonging to a-Si in Raman spectroscopy indicates an increase in the FWHM was observed after annealing MW 303 and MW 304 at 700°C, thus signifying an escalation in the disorder of the thin film.

The reduction in band gap, for both $E_{g\ (Tauc)}$ and E_d observed indicates structural rearrangement of the material, and a reduction in E_d indicates that the density of the thin films increases as the annealing temperatures increase. The reduction in Tauc band gap is not due to a decrease in the conduction edge, but instead may be due to further tailing of the valence and conduction bands into the forbidden region as an increase in disorder occurs as indicated by the increase in Γ values observed in Raman Spectroscopy. The increase in disorder in the thin films due to the heat treatment, which causes structural rearrangement to take place at high temperatures. During the effusion of hydrogen and nitrogen, trap states may have been formed within the forbidden region, thus giving the illusion of a decreasing band gap, while increasing the absorption coefficient of the film.

UNIVERSITY of the
WESTERN CAPE

Conclusion

XRD was performed to determine the bonding structure of the SiN_x molecules in the thin film, and was characterised as amorphous in its as-deposited state. No change in the structure was observed after high temperature annealing and the structure retained its amorphous nature.

Raman spectroscopy was used to determine if any changes in the short range bonding order occurred after being exposed to high temperatures. This was done by analysing TO peaks of the a-Si contributions in the as-deposited and annealed spectra and comparing the FWHM and $\Delta\vartheta_b$ values. No change in the short-range order for the silicon matrix was observed for the as deposited and the annealed

thin film samples in both series, confirming the amorphous nature of the thin films.

The measured values of Γ from the FWHM of the TO peak of a-Si:H allowed for the calculation of the RMS bond angle values of the same peak, the as-deposited samples correlated well with those for amorphous structures. After annealing an increase in the Γ values was observed and this was associated to an increase in disorder in the thin films.

Fourie Transform Infrared Spectroscopy and Elastic Recoil Detection Analysis was conducted on the as-deposited and annealed thin film samples to probe both the bonded and total hydrogen contained in the thin films, as well as the overall bonded structure of the thin films.

FTIR revealed that changes in the bonding structure occurs as the annealing temperature increased, causing a decrease in specific bonding configuration and an increase in others. At lower annealing temperatures rearrangement of the bonds are detected, after annealing at 600°C a huge loss in bonded hydrogen is observed in the MW 304 sample, with an increase in the bonded modes at lower wavenumbers.. Unfortunately the thin films belonging to the MW 303 annealing set were not stable at templeratures higher than 500°C and a similar trend could not be investigated.

ERDA was conducted to reaffirm the trends observed in the FTIR as well as to track the changes in the total hydrogen content of the thin film. At lower annealing temperatures no significant change in the hydrogen content is observed, with slight changes in the bulk of the thin film. It is only once the thin films were

UNIVERSITY of the
WESTERN CAPE

exposed to temperatures exceeding 500°C that a loss in the bulk of the thin films is observed. After annealing at 1000°C only surface hydrogen is observed.

AFM and HRSEM were used to characterise the surface features present on the as-deposited and the annealed thin films for MW 303 and MW 304. An overall decrease in roughness was observed with increasing annealing temperature, as the protrusions seen in the as-deposited thin films were observed to decrease in height and width for each increase in annealing temperature.

At high annealing temperatures (1000°C) two types of surfaces were detected by AFM, a blistered surface as well as a uniformly smooth surface, and this was corroborated with the use of HRSEM. The HRSEM detected little clusters of protrusions; this was not seen by the AFM due to the area selected on the surface of the thin film, whereas with the HRSEM, the chosen magnification and operating voltage allowed for a broader overview.

UNIVERSITY of the
WESTERN CAPE

The optical properties of a-SiN_x both as-deposited and annealed were investigated. The thin films described here were deposited under varying conditions such as low flow rates and the low temperature of the wire, in contrast to the usually used conditions in literature. The results however are no different to those observed in the thin films deposited under high gas flow rates conditions and using deposition techniques such as the industrially favoured PECVD, with many of the same trends being observed.

The OJL model used to describe the dielectric functions of semiconducting material was used to analyse the optical reflection spectra. A single layer OJL model on its own was not powerful enough to calculate the optical constants of the material, as the material is highly complex and riddled with inhomogeneities

due to the deposition effects. EMA theory was used to create more complex, and together an (EMA + OJL) optical model was used to calculate the optical parameters.

The single oscillator WD model was used to calculate the optical constants from the results obtained from the optical model. A comparison is drawn between the Tauc band gap and the "centre of gravity" average gap. The latter band gap is calculated to be higher compared to that of the Tauc band gap, but follows the same decreasing trend as annealing temperature increases.

The increase in disorder which was calculated in Raman Spectroscopy was correlated to the decrease in band gap as an increase in the number of trap states introduced into the forbidden region, and not the decrease of the conduction band. The refractive index was observed to increase as the annealing temperature increases, the refractive index values tended towards those of a-Si:H. As the annealing experiment progressed, and the annealing temperatures increased, hydrogen and nitrogen effused out of the thin films. The final product ultimately being like a pure semiconducting material such as a-Si:H, with the $\Delta\vartheta_b$ values calculated corroborating these results.

UNIVERSITY of the
WESTERN CAPE

References

[3.1] A. Adams, MSc Thesis, University of the Western Cape, Bellville, South Africa (2013).

[3.2] L. Giacomazzi, P. Umari, *Phys. Rev. B.*, **80** (2009) 144201.

[3.3] R. Nietubyć, E. Sobczak, O. Šipr, J. Vackář, A. Šimůnek, *Journal of Alloys And Compound*, **286** (1999) 148.

[3.4] F. Giorgis, C. F. Pirri, E. Tresso, *Thin Solid Films*, **307** (1997) 298.

[3.5] Y. Lai, S. W. Yung, J. Wang, *Thin Solid Films*, **519** (2011) 2235.

[3.6] W. C. Tan, S. Kobayashi, T. Aoki, R. E. Johnson, S. O. Kasap, *J Mater Sci: Mater Electron*, **20**, (2009) S15.

[3.7] V. Verlaan, A. D. Verkerk, W. M. Arnoldbik, C. H. M. van der Werf, R. Bakker, Z. S. Houweling, I. G. Romijn, D. M. Borsa, A. W. Weeber, S. L. Luxembourg, M. Zeeman, H. F. W. Kekkers, R. E. I. Schropp, *Thin Solid Films*, **517** (2009) 3499.

[3.8] V. Verlaan, C. H. M. van der Werf, W. M. Arnoldbik, H. D. Goldbach and R. E. I. Schropp, *Phys. Rev. B*, **73** (2006) 195333.

[3.9] W. Xu, B. Li, T. Fujimoto, I. Kojima, *Surface and Coatings Technology*,**135** (2001) 274.

[3.10] J. K. Holt, D. G. Goodwin, A. M. Gabor, F. Jiang, M. Stavola, H. A. Atwater, *Thin Solid Films*, **430** (2003) 37.

[3.11] A.K. Panchal, C.S. Solanki, *Thin Solid Films* **517** (2009) 3488.

[3.12] J. Xu, Y. Rui, D. Chen, J. Mei, L. Zhou, Z. Cen, W. Li, K. Chen, *Materials Letters*, **61** (2007) 5010.

[3.13] D. Beeman, R. Tsu, M. F. Thorpe, *Phys. Rev*, **B 32** (1985) 184.

UNIVERSITY of the
WESTERN CAPE

[3.14] A.J.M. Berntsen, '*Structural Disorder in Pure and Hydrogenated Amorphous Silicon*',PhD thesis, Utrecht University, Utrecht, The Netherlands, (1993).

[3.15] B. P. Swain, B. S. Swain, and N. M. Hwang, *Applied Surface Science*, **225** (2008) 2557.

[3.16] J.M. Owens, D. Han, B. Yan, J. Yang, K. Lord, S. Guha, *Mat. Res. Soc. Symp. Proc.* **762** (2003) A4.5.2.

[3.17] E.M. Esposito, L.V. Mercaldo, P.D. Veneri, L. Lancellotti, C. Privato, *Energy Procedia*, **2** (2010) 159.

[3.18] C.S. Cook, T. Daly, R. Liu, M. Canonico, M. Erikson, Q. Xie, R. Gregory, S. Zollner, *International Conf. on Compound Semiconductors* (2003).

[3.19] V. Verlaan, '*Silicon Nitride at High Growth Rates Using Hot Wire Chemical Vapor Deposition*', PhD Thesis, Utrecht University, Netherlands, (2008).

UNIVERSITY of the
WESTERN CAPE

[3.20] G. Scardera, T. Puzzer, I. Perez-Wurfl, G. Conibeer, *Journal of Crystal Growth*, **310** (2008) 3680.

[3.21] G. Beshkov, D. B. Dimitrov, N. Velchev, P. Petrov, B. Ivanov, L. Zambov, T. Dimitrova, *Vacuum* **58** (2000) 509.

[3.22] F. Liu, S. Ward, L. Gedvilas, B. Keyes, B. To, Q. Wang, *J. Appl. Phys.*, **96** (2005) 29730.

[3.23] F. L. Martínez, and I. Mártil, G. González-Díaz, B. Selle, I. Sieber, *J. Appl. Phys*. **86** (1999) 2055.

[3.24] Y. Mai, V. Verlaan. C.H.M. van der Werf, Z.S. Houweling, R. Bakker, J.K. Rath, R.E.I. Schropp, *Journal of Non-Crystalline Solids* **354**

(2008) 2372.

[3.25] M. Ionescu, B. Richards, L. McIntosh, R. Siegele, E. Stelcer, O. Hawas, D. Cohen, T. Chandra, *Material Science Forum Vols*. **539-543** (2007) 3551.

[3.26] M. Mayer, SIMNRA User's Guide.

[3.27] C. Savall, J.C Bruyère, *Thin Solid Films* **258** (1995) 1.

[3.28] C. Boehme, G. Lucovsky, *J. Appl. Phys*., **88** (2000) 6055.

[3.29] R. R. L. De Oliveira, D. A. C. Albuquerque, T.G.S. Cruz, F. M. Yamaji and F. L. Leite, '*Measurement of the Nanoscale Roughness by Atomic Force Microscopy:Basic Principles and Applications*', InTech (2012).

[3.30] I. Horcas, R. Fernández, J. M. Gómez-Rodríguez, J. Colchero, J. Gómez Herrero, A. M. Baro, Rev. Sci. Instrum., **78** (2007) 013705.

[3.31] W. Xu, B. Li, T. Fujimoto, I. Kojima, *Surface and Coatings Technology* **135** (2001) 274.

[3.32] C. J. Oliphant, C. J. Arendse, T. F. G. Muller, D. Knoesen, *Appl. Surf. Sci*. (2013), http://dx.doi.org/10.1016/j.apsusc.2013.08.075 (Article in press).

[3.33] C.H.M. van der Werf, H.D. Goldbach , J. Löffler , A. Scarfó, A.M.C. Kylner ,B. Stannowski , W.M. ArnoldBik , A. Weeber , H. Rieffe , W.J. Soppe , J. K. Rath , R.E.I. Schropp, *Thin Solid Films* **501**, (2006) 51.

[3.34] S. H. Wemple, M. DiDomenico, *Phys. Rev. **B*** **3** (1971) 1338.

[3.35] R. Swanepoel, J. Phps. *E: Sci. Instrum.*, 16 (1983) 1214.

[3.36] J. J. Mei, H. Chen, W. Z. Shen, H. F. W. Dekkers, *J. Appl. Phys.*, **100** (2006) 073516.

[3.37] S. K. O'Leary, S. R. Johnson, P. K. Lim, *J. Appl. Phys*., **82** (1997) 3334.

UNIVERSITY of the
WESTERN CAPE

[3.38] W.Theiss Hard- and Software, Accessed on April 2012, from: http://www.mtheiss.com.

[3.39] A. Gordijn, J. K. Rath, and R. E. I. Schropp, *Appl. Phys. Lett*. **85**, (2004) 5096.

[3.40] D.A.G. Bruggermann, *Ann. Physik (Leipzig)*, **24** (1935) 636.

[3.41] T. F. G. Muller, C. J. Arendse, S. Halindintwali, D. Knoesen, R.E.I. Schropp, *Thin Solid Films*, **519** (2011).

[3.42] A.-S. Keita, A. En Naciri, F. Delachat, M. Carrada, G. Ferblantier, A. Slouli, M. Stchakovsky, *Thin Solid Films*, **519** (2011) 2870.

[3.43] K. J. Laildler, J. H. Meiser, '*Physicsal Chemistry'*, 2nd Edition', Houghton Mifflin Company, Boston (1995).

[3.44] K.N. Anderson, W.E. Svendsen, T. Stimpel-Linfner, T Sulima, and H. Baumgärrtner, *Applied Surface Science* **243** (2005) 401.

[3.45] M. Fox, '*Optical Properties of Solids'*, Oxford University Press (2001).

[3.46] N. Piggins, S. C. Baylisst, E. A. Davis and T. Shen, *J. Phys.: Condens. Matter*, **1** (1989) 8111.

[3.47] J. Yoo, S.K. Dhungel, J. Yi, *Thin Solid Films*, **515** (2007) 7611.

[3.48] F. L. Martínez, and I. Mártil, G. González-Díaz, B. Selle, I. Sieber, *Journal of Non-Crystalline Solids*, **227** (1998) 523.

[3.49] B. Karunagaran, S.J. Chung, S. Velumani, E.-K. Suh, *Materials Chemistry and Physics* **106** (2007) 130.

UNIVERSITY of the
WESTERN CAPE

Summary

Chapter one highlights the need for sources of cheap alternative energy such as photovoltaic solar cells, which is a viable clean energy source to replace the depleting stocks of harmful fossil fuels. The conversion efficiency of a photovoltaic solar cell (bulk or thin film) can be increased by incorporating an anti-reflective coating, ensuring that the majority of the radiation is transferred to the active bulk layer deep within the solar cell. SiN_x is put forward as a practical choice as an anti-reflective coating, as the optical parameters may be tailored by varying the deposition conditions.

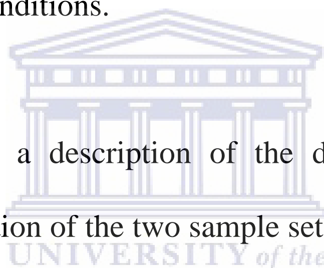

Chapter two undertakes a description of the deposition and post deposition conditions in the preparation of the two sample sets used in the current study, with details of the analytical techniques used in the characterisation of the thin films. The techniques include XRD and Raman spectroscopy for the determination of the structural changes which may have occurred during the heat treatment, FTIR and ERDA for the determination of the bonding structure and the total hydrogen content of the thin films respectively. AFM and HRSEM were used to study the evolution of the surface of the material, with increasing annealing temperature. The optical parameters such as refractive index and Tauc band gap were determined with the use of optical reflection measurements. EMA theory was required to successfully extract the optical parameters from the simulations.

In chapter three a comparison of the two types of thin films were conducted, describing how a difference in nitrogen content affects the overall structural and optical properties of the thin film during the annealing experiment. It was found that the thin films remained amorphous after annealing at 1000°C. FTIR analysis showed an increase in Si-N bonds, and a shift to higher wavenumbers in both sets of samples. The total hydrogen content was found to decrease with an increase in annealing temperatures. AFM as well as HRSEM analysis revealed protruding structures on the surface of the thin film, which affected the as-deposited roughness in both series. The protrusions formed as a consequence of the growth process, and the size of the structures were observed to decreased as the films were exposed to high temperatures, reducing the overall roughness of the thin film. The major difference between the two series described is the difference in nitrogen over silicon ratio contained in the in the silicon matrix. During annealing the thin film with the higher N/Si ratio withstood a higher annealing temperature compared to the thin film containing the lower N/Si ratio, with refractive index for the higher N/Si ration containing thin film calculated to be lower when compared to the lower containing N/Si counterpart. This was attributed to the deposition conditions, as NH_3 catalyses more readily on the hot wire compared to SiH_4. A reduction in thickness is observed after films were exposed to high temperatures, as the residual gas diffuses outwards.

An overall decrease in band gap ($E_{g\ (Tauc)}$ and E_0) was observed as the refractive index increased with annealing temperature. A decrease in thin film density was observed as the annealing experiment progressed, and the optical parameters tended towards those of a pure semiconducting material, with the loss of

UNIVERSITY of the
WESTERN CAPE

hydrogen, and the formation of absorbing Si-Si bonds. The changes in optical properties were linked to changes observed in structural techniques such as FTIR, Raman spectroscopy, and ERDA.